Single Walled Carbon Nanotubes Assembly: Nanohybrids toward Photodetection and Junction Engineering

Qingyu Ye

Under the supervision of
Dr Matteo Palma

School of Biological and Chemical Sciences
Queen Mary University of London

Submitted in partial fulfilment of the requirements of
the Degree of Doctor of Philosophy

September 2020

Statement of Originality

I, Qingyu Ye, confirm that the research included within this thesis is my own work or that where it has been carried out in collaboration with, or supported by others, that this is duly acknowledged below and my contribution indicated. Previously published material is also acknowledged below.

I attest that I have exercised reasonable care to ensure that the work is original, and does not to the best of my knowledge break any UK law, infringe any third party's copyright or other Intellectual Property Right, or contain any confidential material.

I accept that the College has the right to use plagiarism detection software to check the electronic version of the thesis.

I confirm that this thesis has not been previously submitted for the award of a degree by this or any other university.

Signature: Qingyu Ye

Date: 17/09/2020

Details of Collaborations and Publications

1. Qingyu Ye, Xinzhao Xu, Thomas Bamford, Benjamin R Horrocks, Andrew Houlton, Stoichko Dimitrov, Matteo Palma. Photoresponsive Multiplexed Nanoscale Devices: DNA-wrapped Carbon Nanotubes as Solution-processable Templates for the Assembly of Organic-Inorganic Nanohybrids. *Manuscript in preparation.*

2. Giuseppe Amoroso, Qingyu Ye, Keitel Cervantes-Salguero, Gustavo Fernandez, Alessandro Cecconello, Matteo Palma. DNA-Powered Stimuli-Responsive Single-Walled Carbon Nanotube Junctions. *Chem. Mater.* **31**, 1537–1542 (2019).

3. Pierrick Clement, Piera Trinchera, Keitel Cervantes-Salguero, Qingyu Ye, Christopher R. Jones, Matteo Palma. A one-step chemical strategy for the formation of carbon nanotube junctions in aqueous solution: Reaction of DNA-wrapped carbon nanotubes with diazonium salts. *Chempluschem* **84**, 1235–1238 (2019).

4. Giuseppe Amoroso, Andrei Sapelkin, Qingyu Ye, Vicente Araullo-Peters, Alessandro Cecconello, Gustavo Fernandeze, Matteo Palma. DNA-Driven Dynamic Assembly of MoS2 Nanosheets. *Faraday Discuss.* (2020). doi:10.1039/c9fd00118b

TABLE OF CONTENTS

Abstract

By synergistically combining the individual properties of more than one nanoscale component, novel features of hybrid structure assemblies represent a key motivation for making future functional nanomaterials. In this thesis, the successful construction of a multiplexed photo-responsive chip from DNA-wrapped single walled carbon nanotubes (DNA-CNTs) and DNA-CNT templated inorganic-organic hybrid structures is first demonstrated. The effective assembly of the hybrids was characterized by atomic force microscopy (AFM) and the corresponding device performance as well as the key mechanisms behind were investigated.

Then a facile approach for the fabrication of end-to-end SWCNT junctions exploiting oligonucleotides as molecular linkers is presented. The assembled junctions show clear stimuli-responsive features stemming from the designed sequences of oligonucleotides; this grants the SWCNTs the ability to self-assemble and disassemble under specific conditions in aqueous solutions. The junction formation was confirmed by Atomic Force Microscopy (AFM) and time-dependent fluorescence analysis. Moreover, an efficient strategy to sort DNA-wrapped SWCNTs (DNA-CNTs) by length via a gel electrophoresis technique was developed (confirmed by AFM). In addition to the application of oligonucleotides, the use of diazonium salts not only as a molecular linker but also the major reactive agent for CNT junction formation was also explored.

In conclusion, by integrating DNA-CNTs with other active components, we have achieved the assembly for organic-inorganic nanohybrids of multiplexed photo-sensing capabilities and the assembly of reconfigurable SWCNT junctions with stimuli-responsive features. Moreover, the facile and efficient strategies developed in our work can contribute to the controlled assembly of CNT based functional nanohybrids.

List of Figures

List of Abbreviations and Acronyms

A	Adenine
AC	Alternating current
AFM	Atomic force microscope (microscopy)
ATP	Aqueous two phase
C	Cytosine
CdS	Cadmium sulfide
CdSe	Cadmium selenide
CE	Capillary electrophoresis
CM	Clausius-Mossotti factor
CNT	Carbon nanotube
CoMoCAT	Cobalt–molybdenum catalyst
CVD	Chemical vapor deposition
DC	Direct current
DEP	Dielectrophoresis
DGU	Density gradient ultracentrifugation
DMF	Dimethylformamide
DNA	Deoxyribonucleic acid
DNA-CNT	DNA-wrapped carbon nanotube
DOS	Density of states
dsDNA	Double-stranded DNA
DX	Double-crossover
EDTA	Ethylenediaminetetraacetic acid
FRET	Förster resonance energy transfer (fluorescence resonance energy transfer)
G	Guanine

GE	Gel electrophoresis
HiPco	High-pressure carbon monoxide
HOMO	Highest occupied molecular orbital
IEX	Ion exchange chromatography
i-motif	Intercalated motif
LUMO	Lowest unoccupied molecular orbital
MEG	Multiple exciton generation
MOPS	3-(N-morpholino) propanesulfonic acid
MWCNT	Multi-walled carbon nanotube
Na_2S	Sodium sulfide
Nd:YAG	Neodymium-doped yttrium aluminium garnet
NIR	Near infrared
NP	Nanoparticle
OD	Optical density
OP	Oxygen plasma
PbS	Lead sulfide
PEG	Polyethylene glycol
PM	Photomultiplier tube
PZT	Piezoelectric
QD	Quantum dot
RNA	Ribonucleic acid
SC	Sodium cholate
SD	Standard deviation
SDS	Sodium dodecyl sulfate
SEC	Size exclusion chromatography
SPM	Scanning probe microscope (microscopy)
ssDNA	Single-stranded DNA

SWCNT	Single-walled carbon nanotube
T	Thymine
TAE	Tris-acetate-EDTA
TAS	Transient absorption spectroscopy
THF	Tetrahydrofuran
$U_{L\text{-}J}$	Lennard-Jones potential
UV	Ultraviolet
UV-vis-NIR	Ultraviolet-visible-near infrared

Acknowledgement

These fruits are our sustenance on the earth.[1]

Now that I'm here. I would like to take this chance to thank all that helped and motivated me along this journey. Without them I can never unfold the unimagined and come this far.

First of all, I would like to thank my supervisor Dr Matteo Palma, who introduced me to the nanoscience world and patiently gave me honest advices during the difficult times. He is the most supportive person no matter it's about experiments, ongoing projects or collaborations. It is a real honour to have him as the supervisor.

It is my fortune to meet all the lovely people in Queen Mary. Together with the fascinating DNA nanotechnology world, my friend Dr Alessandro Cecconello has greatly inspired me. I cannot thank more for the care he showed for me and the precious times we shared in the lab. Life might be a "mistake" and let's try to minimize it. Dr Stoichko Dimitrov, with his steady speaking pace and sudden smile, helped me to walk through the hard part of the experiments. I am truly grateful for his patience and kind help about the project. I really appreciate the inspirational discussions with Dr Keitel Cervantes Salguero during lunch times and respect his fight for the people he cares for. Dr Pierrick Clement, as a buddy not just in the lab: I miss the barbecues we made in

[1] Translated from page XI of *LES NOURRITURES TERRESTRES* from Andre Gide, Chinese edition. ISBN: 978-7-5327-6752-6.

summer and stews in winter. Dr Antonio Attanzio kindly demonstrated the essential lab skills to me at the very beginning of my PhD, which I will never forget. I appreciate Dr Jingyuan Zhu and Dr Da Huang for their warm-hearted welcome and for getting me familiar with the lab. I would also like to thank Giuseppe Amoroso for the invaluable accompany and the times at the start of our PhD. I am really gratitude for the welcoming host from Dr Andrew Houlton, Dr Benjamin R. Horrocks and Dr Thomas Bamford in Newcastle University. I would like to thank Xinzhao Xu, a hardworking and professional scientist, for his work and support during the PhD. Thank Dr Mark Freeley for showing me the way towards climbing and all the jokes from his brilliant mind (no matter I really understood them or not). I would also like to thank Caoimhe O'Neil, William Hawkes, William G. Neal, Sandra Perez Garrido, Ugne Balciunaite, Angus Hawkey for the times we've shared in Queen Mary.

I want to show my appreciation for the dear friends that I met in the journey. They kept inspiring me about the world and encouraging me to explore further. Thank all the lovely mates in Ifor Evans Place. Thank all the friends I met in Skeggs House. Special thanks to Oliwia Alksnin and Adonis Kamarligkos for the precious time we enjoyed in our little loving flat and all the breath-taking dishes we cooked together (and the failed ones too). Thank Yiming Dong for all the miles we walked, travels we made and talks we had. Thank Yahong Wu for all the accommodations he kindly provided (and all the amazing hotpots we enjoyed and suffered). Thank Kai Yang for the valuable discussions about film making and beyond. Thank Sirini for all the curries that sparked my cooking ideas.

Thank my parents for the warmest home in the world, which is the eternal drive and harbour.

Four years flew as the arrow, heading towards the start of another paragraph. Ups and downs running away remind me about the ups and downs waiting ahead. All efforts are Sisyphus efforts, and all efforts count.

Chapter 1

Introduction

Ever since their discovery in the 1990s,[1,2] carbon nanotubes (CNTs) have drawn attention from scientists around the world. As novel one-dimensional all-carbon materials with outstanding mechanical, chemical, electrical and optical properties,[3–8] CNTs are considered to be one of the most promising nanomaterials to drive the development of nanoscience and nanotechnology. After nearly 30 years of intensive study, researchers have made extraordinary progress in aspects including CNT synthesis, CNT theories (e.g. of 1D electrical transport in CNTs since they provide the perfect platform for related experimental tests) and applications of CNTs in fields like composite materials, mirco-/nanoelectronics and optoelectronics.[7,9–15] However, given the great progress achieved, challenges remain such as the efficient sorting of single-walled carbon nanotubes (SWCNTs) by length and chirality, facile assembly of CNT based nanostructures in aqueous solutions and CNT junction engineering with higher degree of site-specific control.

Deoxyribonucleic acid (DNA) is the biological molecule that stores and transmits significant genetic information in biological systems. Since its conceptual emergence

in the early 1980s,[16] the field of DNA nanotechnology has taken this molecule out of its biological context and used its information to assemble structural motifs and then to connect them together. With the increasing popularity DNA has gained from researchers around the world, well-designed DNA molecular systems have proved their potential to serve as a significant and versatile tool to promote the evolution of novel nanostructures.[17]

In this chapter, we will first introduce the basic concepts and properties, synthesis methods, post-synthetic sorting and chemical functionalizations of CNTs. In the second section, hybrid nanostructures based on CNTs including DNA-wrapped CNTs, CNT-semiconductor heterostructures and CNT junctions will be briefly introduced. In section three, a concise review on parts of DNA nanotechnology will be covered, with the focus on static and dynamic DNA nanostructures.

1.1 Carbon nanotubes (CNT)

1.1.1 Properties

Carbon nanotubes (CNTs) are one dimensional carbon materials which can be seen as a rolled up cylinder made up from a graphene sheet.[18] Graphene is a single layer of carbon atoms arranged in a two dimensional honeycomb lattice and the stacked graphene layers are known as graphite.[19,20] A tube made of a single graphitic layer cylinder is called a single walled nanotube (SWCNT) while a tube made with several concentrically arranged cylinders is a multiwalled nanotube (MWCNT). The length of CNTs can reach the micrometre scale with a diameter range from sub nanometre (as for

some SWCNTs) to 100 nm (typical for MWCNTs).[21] The presence of the C-C graphitic bond provides SWCNT with excellent chemical and mechanical properties, while the presence of extended, delocalized π-electron systems grants these carbon materials the capability to provide the ideal environment for charge transfer processes,[22] when combined, for example, with photoexcited electron donors.[23] Moreover, the electron accepting ability of semiconducting SWCNTs offers an opportunity to facilitate electron transport and increase the photo-conversion efficiency of nanostructure semiconductor based photovoltaic devices.

Because the microscopic structure of carbon nanotubes is closely related to graphene, their extraordinary properties have their origin in the particular electronic structure of graphene and CNTs are usually defined in terms of the graphene lattice vector (defined in ***Figure 1-1 a*** by the vectors $\vec{a}_1$ and $\vec{a}_2$). In carbon nanotubes, the graphene sheet is rolled up in such a way that a graphene lattice vector $\vec{c} = n_1\vec{a}_1 + n_2\vec{a}_2$ becomes the circumference of the tube. This vector $\vec{c}$, defined by two integers (n_1 and n_2), is called the chiral vector and it defines a particular SWCNT chirality. ***Figure 1-1 b, c*** and ***d*** illustrate SWCNTs with different chiralities. Featured properties of the nanotubes, like their electronic band structure, vary dramatically with the chiral vector even for SWCNTs with similar dimeter and direction of the chiral vector.[18]

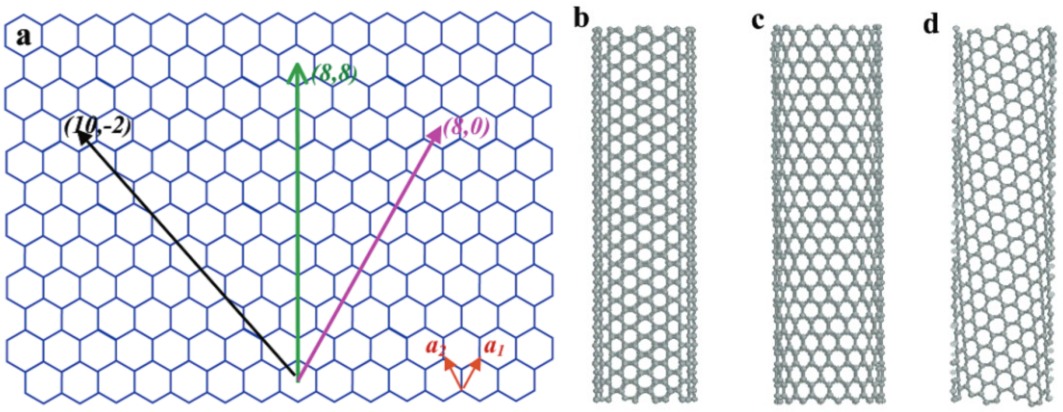

Figure 1-1. *The structures of graphene and single walled carbon nanotubes. (a) The carbon atoms in a single sheet of graphene are arranged in a honeycomb lattice. The basic vectors* $\vec{a}_1$ *and* $\vec{a}_2$ *are presented on the bottom-right corner. (b-d) SWCNTs with different chiral vectors.*

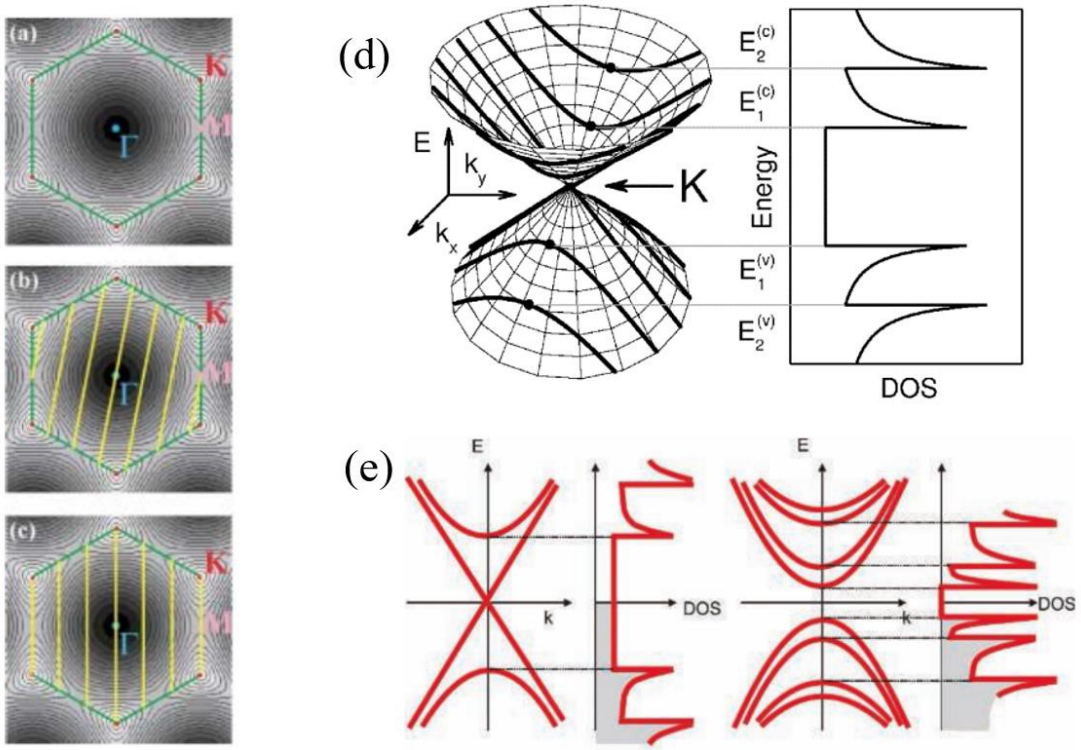

Figure 1-2. *Band structures in K space: (a) graphene; (b) semiconducting single-wall carbon nanotubes (c) metallic single-wall carbon nanotubes. The yellow lines indicate the allowed wave vectors after roll-up of the graphene sheet. (d) The 1D density of states (DOS) for the conduction and valence bands. (e) Schematic electronic energy-dispersion relations and densities of states of: a) metallic (left) and semiconducting (right) single-wall carbon nanotubes.*[6,24,25]

The electrical properties of CNTs can be studied starting from the honeycomb graphene structure (as shown in ***Figure 1-1 a***). Whereas graphene is a zero-gap semiconductor, in the case of the CNTs the electrons are confined along the circumference, and while the wave vector $\vec{k}$ along the tube axis $\vec{k}_{||}$ is continuous, as the tube is regarded as infinitely long, along the circumference periodic boundary conditions are imposed:

$$\vec{k}_{\perp} * \vec{c} = 2\pi j$$

where $\vec{c}$ is again the chiral vector and *j* is an integer. Consequently, any wave vector $\vec{k}_{\perp}$ is quantized and only certain set of the graphene *k* states are allowed. Therefore, each band of graphene is divided into a set of discrete energy sub-bands defined by *j* and the allowed energy states of a SWCNT are 1D sections of the graphene band structure (yellow lines in ***Figure 1-2 b*** and ***c***). The position of the allowed states is very important as they define the electronic properties of the CNTs: when the allowed states of a CNT pass through a Fermi point (K or K'), the tube is metallic. On the other hand, if no state passes through the Fermi point the tube is a semiconductor. Specifically, (*n*, *n*) nanotubes (armchair tubes) are always metallic; (*n*, *m*) nanotubes with $n - m = 3j$ $(j = 1, 2, 3 \ldots)$, are almost metallic: a tiny gap opens because of curvature effects; when $n - m \neq 3j$ $(j = 1,2,3 \ldots)$, CNTs are semiconductors. In the simple tight-binding model, the bandgap E_g of semiconducting CNTs is given by:

$$E_g = 4\hbar v_F / 3d_{CNT}$$

where d_{CNT} is the CNT diameter and v_F is the Fermi velocity.[26]

In ***Figure 1-2 d*** the corresponding density of the energy states (DOS) are shown (right hand side): the DOS for graphene around the K point is relatively linear, while at the saddle point M one spike on each band can be observed. On the other hand, in the case of SWCNTs, there are several minima of energy along the allowed sub-bands and in correspondence with these points there are more states with similar energy and the DOS grows massively generating several spikes called van Hove singularities. Effectively, the highest occupied molecular orbital (HOMO) and lowest unoccupied molecular orbital (LUMO) of semiconducting carbon nanotubes correspond to the first van Hove singularities in the valence and conduction bands, respectively, whereas the HOMO

and LUMO of metallic nanotubes meet at the Fermi level and consequently have a zero HOMO-LUMO gap.[24]

The characteristic absorption and photoluminescence spectra of carbon nanotubes are attributed to the van Hove singularities. Every SWCNT species with the specific chiral number (n, m) has its unique absorption and photoluminescence spectra (***Figure 1-3***). As illustrated in ***Figure 1-3 a*** light is absorbed between the van Hove singularities of the valence and conduction band giving rise to E_{ii} absorption transitions ($v_i \rightarrow c_i$) while in the case of photoluminescence, after the light induced excitation, electrons first relax to the lowest conduction van Hove singularity and finally relax to the highest valence van Hove singularity emitting light (E_{11} transition). In the case of metallic tubes there is no energy band gap so while absorbance peaks are present no photoluminescence can be observed.

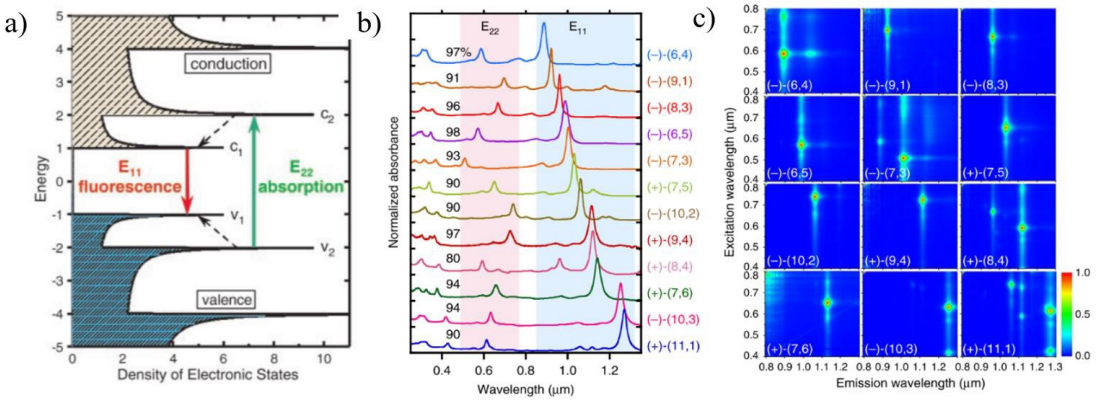

Figure 1-3. *(a) Schematic showing the density of electronic states for a single nanotube structure. Solid arrows depict the optical excitation and emission transitions of interest; dashed arrows denote non-radiative relaxation of the electron (in the conduction band) and hole (in the valence band) before emission. (b) Optical absorption spectra and (c) photoluminescence contour maps of the 12 sorted (n, m) semiconducting SWCNTs.*[24]

1.1.2 CNT synthesis

CNTs are produced by three major methods: laser ablation, arc discharge and chemical vapor deposition (CVD) (***Figure 1-4***). Laser ablation, is the fabrication of CNTs where a high power laser (e.g. Nd:Yag laser) is used to vaporize a carbon target at high temperature under a continuous flux of an inert gas (e.g. argon) and carbon nanotubes grow on the colder surface of the reactor as the vaporized carbon condenses (***Figure 1-4 a***).[27] Both SWCNT and MWCNT can be synthetized with this technique and the quantity and quality of the tubes depends on the amount and type of catalyst, laser power as well as temperature, pressure and inert gas. CNTs can also be prepared through arc-discharge which involves applying a voltage between two graphitic electrodes in the presence of a metallic catalyst allowing the growth of the tubes (***Figure 1-4 b***).[11] Chemical vapor deposition is another method involving the growth of CNTs from a metal catalyst through the deposition of a carbon gaseous source (***Figure 1-4 c***).[28,29] While these are all developed methods for the production of SWCNTs, it has still proven to be challenging to control the chirality of the nanotubes.[30]

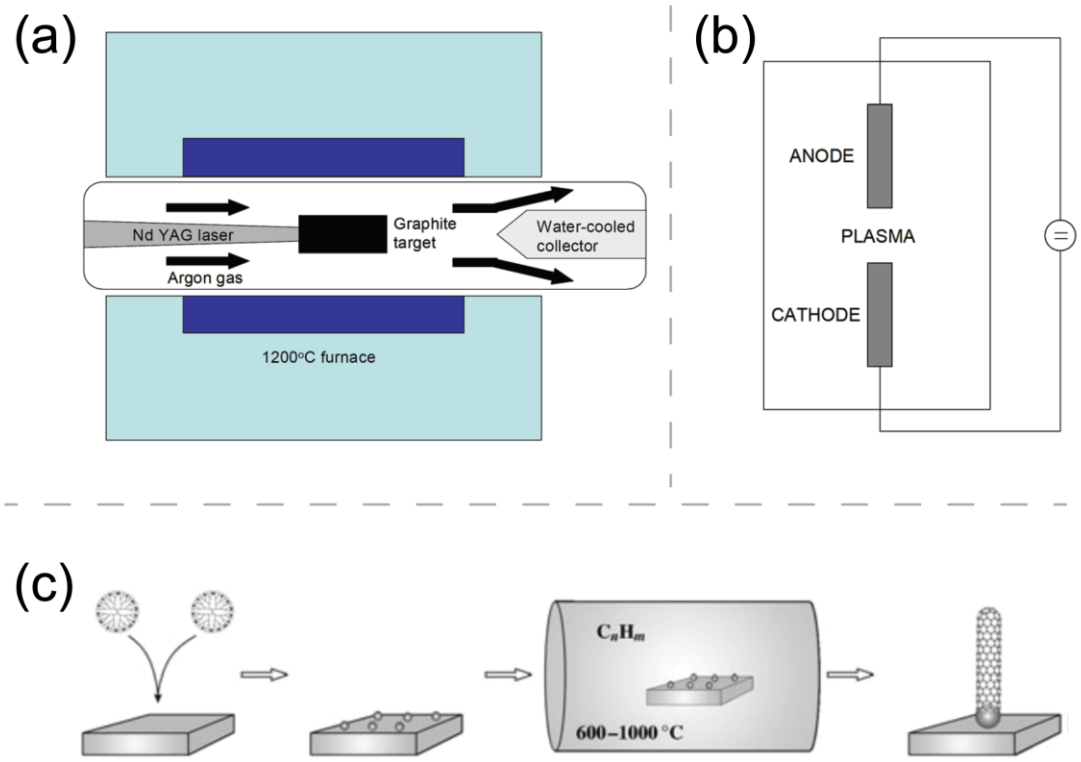

Figure 1-4. *The schematic illustrations of the three major ways to synthesize CNTs. (a) laser ablation; (b) arc discharge; (c) chemical vapor deposition (CVD).*[31]

1.1.3 Post-synthetic sorting of CNTs

The dominant physical dimension of a SWCNT is its length. Certain physical processes, such as carrier recombination, could be length-dependent; device applications, such as CNT-based scanning probes, require CNT length control for easy and reproducible fabrication; solution-phase assemblies of CNTs on solid substrates (e.g. end-to-end CNT junction assembly) will also benefit from CNTs with well-defined length (the uniform building block). On the other hand, the chirality of SWCNTs significantly influences the electronic band structure (especially for semiconducting SWCNTs, as mentioned in section 1.1.1). Consequently, from fundamental studies on single chirality

SWCNT to SWCNT-based semiconducting device fabrications, the realization of a chirality-pure CNT batch is being pursued by researchers around the world.

Though tremendous progress has been made in CNT synthesis, directly making CNTs with a particular size or structure remains a major challenge: the current as-produced samples still contain CNTs of varied lengths and chiralities.[32] As a result, scientists have been trying to find out efficient post-synthetic methods to address the CNT sorting problem. Based on the CNT parameter that is subject to sorting, these methods can be classified into two main branches: length sorting and chirality sorting.

Many studies have been done on length sorting.[32,33] Doorn et al. first demonstrated the possibility of separating as-produced CNTs by length via capillary electrophoresis (CE).[32] The underlying mechanism of such separations is that the mobility of the solution phase (the dispersed CNTs in corresponding solutions) is charge and size dependent under the applied electric field. Based on a similar theory, an approach of size-exclusion chromatography (SEC) has shown the potential for CNT length sorting:[34–36] notably, Zheng et al. developed a SEC method with high resolution sorting capability.[37] However, in many of the reported works, quantification of length variation in obtained fractions was absent. Some works did demonstrate control over the average length of separated tubes; the length variation within a given fraction, however, was typically very broad and could be as high as 80%. In addition, some of the processes reported cannot be scaled up for processing large quantities of materials. It is, thus, highly desirable to develop a scalable process that can yield CNT fractions of well-defined length.

In terms of the chirality sorting, several directions were explored. Pioneering work has been demonstrated by Zheng et al. where ion exchange chromatography (IEX) was exploited to separate DNA-wrapped CNTs (DNA-CNTs) which will be introduced in more detail in section 1.2.1;[38] following that achievement, more single-chirality semiconducting CNT species were obtained with an optimized procedure.[39] In 2005 and 2006, the Mark Hersam group found that density gradient ultracentrifugation (DGU), a well-established biochemical separation method, can be adopted for the separation of CNT chiralities.[40] Applying the aqueous two-phase (ATP) extraction method to chirality sorting was first reported by Zheng et al. in 2013.[41] The ATP extraction method, first explored by Albertson,[42] uses polymer–polymer phase separation to create two immiscible aqueous phases of slightly different physical properties. The ATP extraction method is scalable and relies entirely on homogeneous molecular interactions to achieve separation. It is applicable to both surfactant-coated and DNA-CNTs. Importantly, the emergence of the ATP method continues the trend of moving away from instrumentation-based, external field driven processes to spontaneous, molecular force driven CNT separation processes.

1.1.4 Chemical functionalization of CNTs

It has been demonstrated that CNTs can interact with different classes of compounds.[14,29,43–51] The formation of supramolecular complexes allows a better processing of CNTs toward the fabrication of innovative nanodevices. In addition, CNTs can undergo chemical reactions that make them more soluble for their integration into inorganic, organic, and biological systems.

In order to facilitate their further applications, by covalently attaching chemical groups through reactions onto the pi-conjugated skeleton of CNTs, scientists have developed various approaches to functionalize the materials. These approaches are, including but not limited to: CNT sidewall halogenation,[52–54] cycloaddition,[55–57] radical addition[58–61] and amidation reaction.[62,63]

Importantly, to face the challenge of the direct and efficient functionalization of CNTs, researchers have developed a method to functionalize the sidewall and tips of CNTs by azide photochemistry, where the irradiation of the photoactive azidothymidine in the presence of nanotubes was found to cause the formation of very reactive nitrene groups in the proximity of the carbon lattice.[55,56] In a cycloaddition reaction, these nitrene groups couple to the nanotubes and form aziridine adducts (***Figure 1-5***).

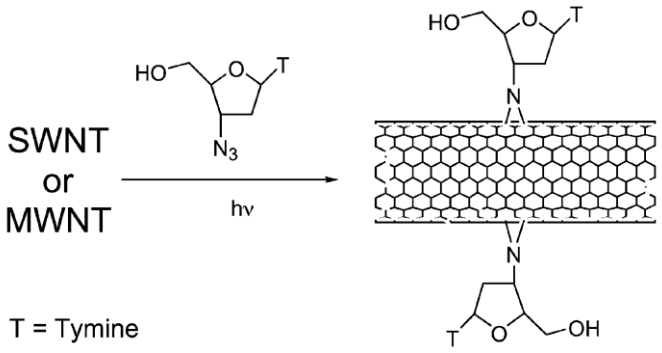

Figure 1-5. *Cycloaddition: photoinduced generation of reactive nitrenes in the presence of nanotubes (medium-pressure xenon lamp with maximum output of 112 mW/cm2 at 254 nm applied).*[64]

Another method introducing radicals onto the CNT surface with diazonium salts was explored by several groups.[58–61] Derivatization of small diameter CNTs (HiPco) was achieved by the electrochemical reduction of substituted aryl diazonium salts in organic

media, where the reactive species was supposed to be an aryl radical. The formation of aryl radicals was triggered by electron transfer between the CNTs and the aryl diazonium salts, in a self-catalyzed reaction. Based on this concept, water-soluble diazonium salts were utilized to react selectively with metallic CNTs.[61,65,66] In particular, electrochemical modification of individual CNTs was demonstrated by the attachment of substituted phenyl groups.[58–60] The reductive coupling of aryl diazonium salts resulted in a C-C bond formation at the graphitic surface of CNTs (***Figure 1-6***).

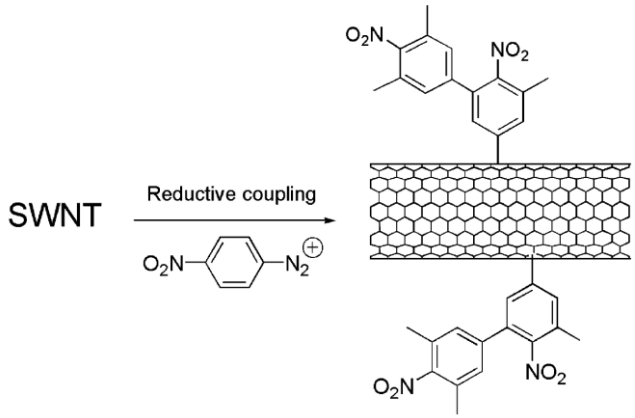

Figure 1-6. *Radical addition: electrochemical functionalization resulting in C-C bond formation.*[64]

1.2 CNT based hybrid structures

1.2.1 DNA-wrapped carbon nanotubes (DNA-CNTs)

Though CNTs can be directly decorated with intended functionalities via covalent approaches,[8] some internal properties (e.g. electronic properties) of CNTs could be altered or undermined greatly, especially for SWCNTs. Additionally, the lack of solubility and the difficult manipulation in any solvents remain a challenge for the further use of CNTs. In fact, as-produced CNTs are insoluble in all organic solvents

and aqueous solutions. They can be dispersed in some solvents by sonication, but precipitation immediately occurs when this process is interrupted.

Therefore, some non-covalent binding approaches were explored to increase the solubility of CNTs without compromising their electronic properties. Different molecules like polymers, biomolecules, surfactants and polyaromatic compounds have been employed as surfactants.[64,67–69] Intriguingly, deoxyribonucleic acid (DNA), as a naturally occurring polymer that plays a central role in biology, can also play an important role in non-biological contexts due to its unique properties. In particular, the formation of a complex from CNTs and DNA has drawn great attention since these hybrids will then take the advantages of both the outstanding properties of CNTs and the selective recombination ability of DNA strands (e.g. base-paring capability). In 2003, Zheng[38,70] et al. successfully bound single-strand DNA (ssDNA) to nanotubes through π-π stacking, in the form of helical wrapping on the surface (shown in ***Figure 1-7***). The strong noncovalent interaction between CNTs and DNA makes SWCNTs soluble and effectively dispersed in aqueous solutions. Moreover, compared to other polymer wrapping methods, DNA coupling offers a high CNT concentration as much as 4 mg/ml. Additionally, the phosphate groups on the DNA in the hybrids provide a negative charge density, which was found to be dependent on the DNA sequence and the CNT chirality.[71,72] Importantly, by introducing interactions with the DNA strands wrapping around CNTs, modifications could be made while still preserving the valued CNT properties.

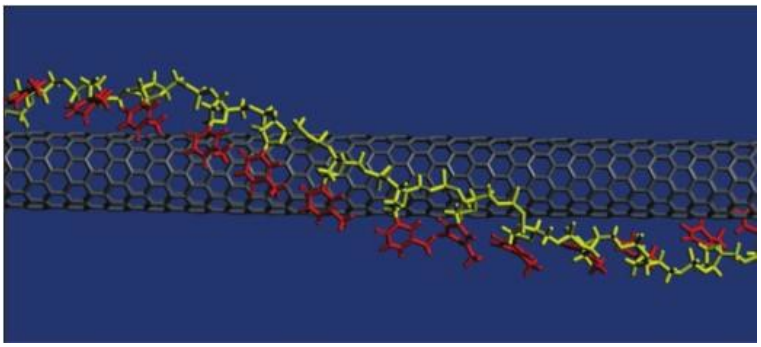

Figure 1-7. *DNA wrapped SWCNT.*[38]

In addition to the outstanding aqueous solubility they have, these DNA-wrapped CNT hybrids also found applications based on other features. In particular, the DNA-CNT hybrid introduces a promising way to sort SWCNTs by their chiralities. Given that the fine structures (how the DNA wraps the CNT surface) of DNA-CNT hybrids are related to the interplay between DNA strands (length and sequence) and CNT chirality, researchers have found ways to specifically pick out a single chirality of nanotubes. Tu et al. have successfully purified 12 single-chirality CNT species from a synthetic mixture via an ion exchange chromatography (IEX) method (***Figure 1-8 a***).[39] On the other hand, an aqueous two phase (ATP) extraction method was introduced by Khripin et al. to separate single chiralities from a synthetic mixture (***Figure 1-8 b, c, d***).[41] These two methods mark the main directions of the chirality sorting for post-synthetic SWCNTs.

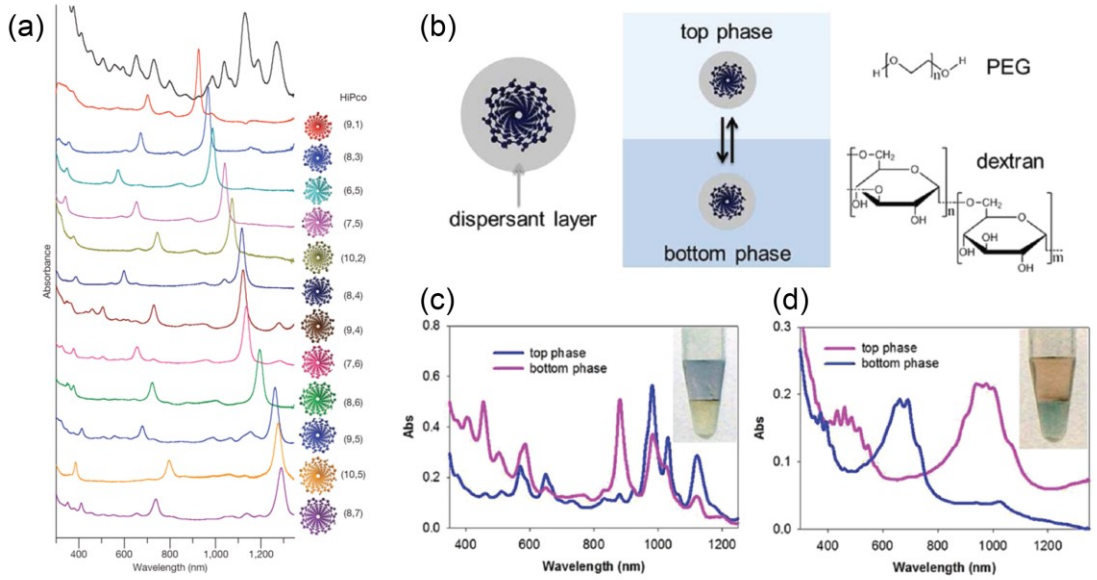

Figure 1-8. *(a) Ultraviolet–visible–near-infrared absorption spectra of 12 purified semiconducting SWCNTs (ranked according to the measured E_{11} absorption wavelength) and the starting HiPco mixture.*[39] *(b) Schematics of the PEG/dextran two-phase system used in ATP method. Top phase is PEG-rich, and bottom phase is dextran-rich. (c) Partition of small diameter CoMoCAT tubes. (d) Partition of large diameter arc-discharge tubes.*[41]

Moreover, site-specific modifications of DNA-CNT hybrids are possible as a result of the different surface conditions between the CNT sidewall and terminal ends that are introduced by the helical wrapping of DNA. For instance, Attanzio et al. attached semiconductor quantum dots (QDs) exclusively to the terminal ends of DNA wrapped CNTs (***Figure 1-9***).[73] This highlights the realization of finer control over the assembly of CNT based nanostructures (e.g. end-to-end SWCNT junctions).

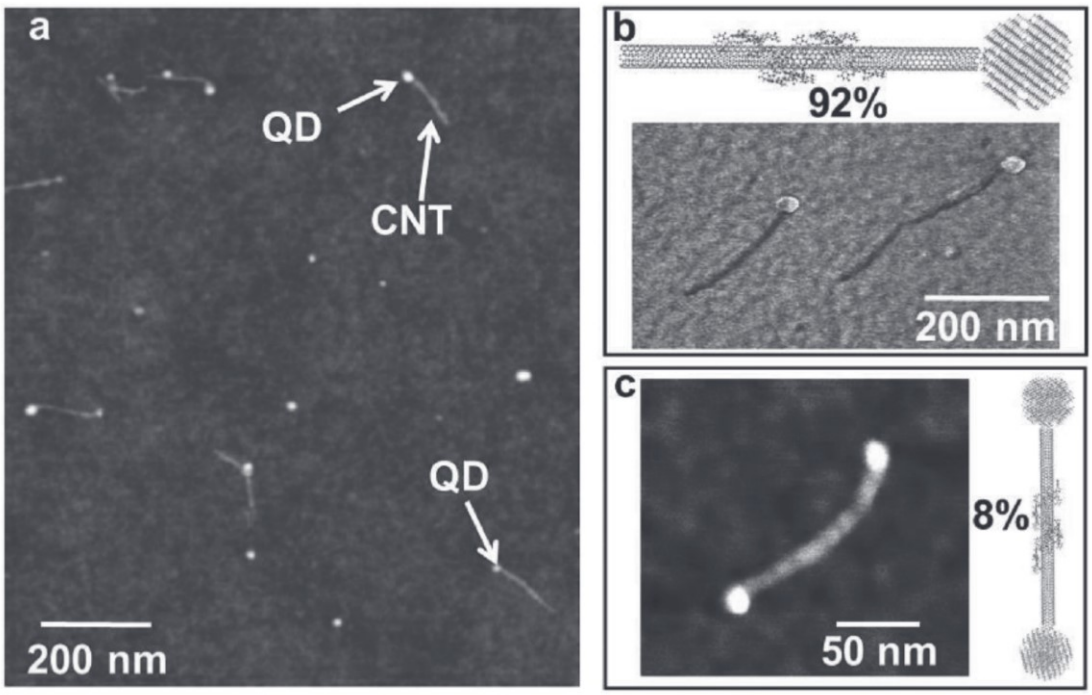

Figure 1-9. *QDs site-specifically attached to the terminal ends of DNA wrapped CNTs. (a) Representative AFM image of SWCNT-QD heterostructures. (b) Schematic and AFM deformation image (defined as the penetration of the tip into the surface at the peak force) of monofunctionalized SWCNT-QD structures: the different mechanical response of the two components of the hybrid is evident. (c) Schematic and AFM topographical image of bis-functionalized SWCNT-QD structures.*[73]

1.2.2 CNT-semiconductor hybrids

By synergistically combining the individual properties of more than one nanoscale component, research efforts on heterostructures assembly and their features represent a key motivation for making future functional nanomaterials.[73–79] Both carbon nanomaterials and semiconductor nanocrystals have been widely studied and a number of devices have been developed. A further step towards better and more efficient devices would be to combine these two materials into functional heterostructures either

to merge and improve the properties of the single components or to take advantage of the possible phenomena that can be generated at the interface.

As depicted in ***Figure 1-10***, different from nanocomposites, where several components in different phases are mixed together in a single matrix material resulting in a combination of the properties of the single component materials (the materials are usually synthetized separately and then combined so that one phase is dispersed into a second one),[75,80] nanohybrids are assembled with a finer control so that a second component is in direct contact with the main support material. In these nanohybrids, the interface between the component materials plays a more significant role. As a result, hybrid materials merge the properties of the components in a way that creates new properties distinct from those of either building blocks.[75]

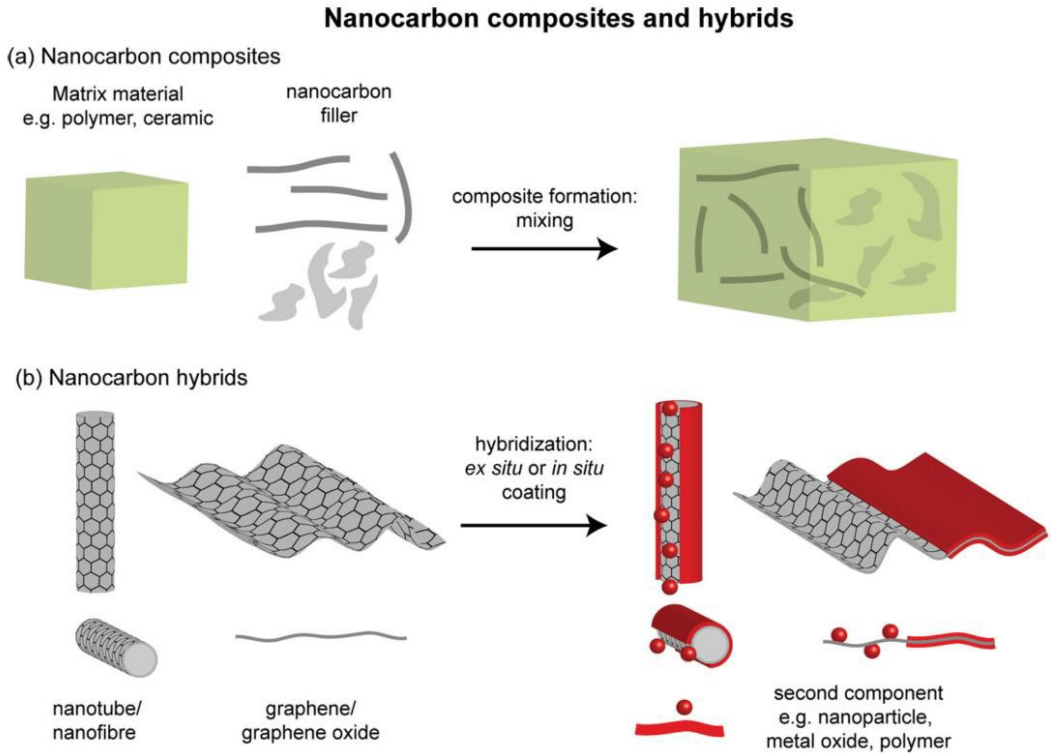

Figure 1-10. *Schematics of nanocarbon composites and hybrids showing differences between (a) nanocarbon composites and (b) nanocarbon hybrids.*[75]

CNT based hybrids are of particular interest due to their advantageous features such as high surface area and outstanding electrical and electronic properties.[81,82] Consequently, CNTs can serve as promising building blocks in nanoarchitectures, making them exceptional nanostructure supports for certain applications.[74,83–87] Meanwhile, inorganic semiconducting quantum dots (QDs) are very appealing components to be assembled with CNTs since they exhibit broad absorption bands and high band gap tunability depending on their size and composition.[88–91]

As a typical example, researchers have been trying to fabricate devices based on CNT-QDs hybrids for next generation optoelectronic applications. In this regard, CdS and CdSe have been widely employed to fabricate systems exhibiting photoresponses to the green/blue light in the visible spectrum.[88,92–94] Istvan et al synthesized CdS-SWCNT hyrbids in THF and methanol, and investigated the electron transfer from CdS to SWCNT by transient absorption spectroscopy (TAS).[92] A similar electron transfer process was proposed for CdSe-CNT heterostructures in a study carried out by Liangbing Hu et al., where hybrids were assembled on a surface from DMF solutions employing CdSe QDs pre-functionalized with a pyrene derivative.[93] Moreover, researchers revealed that amine molecules were able to mediate the doping of SWCNTs, giving them the capability to tune the photoresponse of fabricated CdS-CNT hybrid devices.[94] Similarly, PbS based systems extend the photoresponse into the red and near infrared (NIR) regime.[89,95–99] Defa Wang et al fabricated photovoltaic devices based on PbS-CNT hybrids made from oleyamine capped PbS QDs and pre-functionalized MWCNTs.[96] Fast photoresponse was further obtained in PbS-CNT based devices

fabricated with pulsed laser ablation techniques.[97] Additionally, multiple exciton generation (MEG) was observed in PbS-CNT hybrids highlighting their potential for high performance optoelectronic applications.[98]

1.2.3 CNT junctions

As the promising building block of nanomaterials, CNTs not only form heterostructures with other components but also assemble into intriguing configurations with themselves in the presence of specific molecular linkers. The CNT junctions, though considered as one of the simplest configurations, are significant because of their various potential applications. For instance, the construction of junctions between SWCNTs[100–104] has been investigated for the fabrication of nano-electronic devices.[105–107] Additionally, the use of SWCNTs as nanoelectrodes was proved essential in single molecule investigations such as molecular electron transportation studies.[73,79,101,108–111]

In this context, the controlled assembly of linear (end-to-end) junctions through in-solution approaches[100,101,112–114] is particularly desirable for the low-cost (solution processable) fabrication[115–117] of carbon nanotube-based devices.[109,111] Different methods have been explored for junction formation.[100,103,104,118] For instance, Clement et al. demonstrated an efficient one-step chemical strategy allowing the formation of linear DNA-CNT junctions with diazonium salts in aqueous solutions.[119] On the other hand, although different technologically-relevant nanomaterials have been designed to respond to changes in the surrounding medium,[120,121] the assembly of reversibly reconfigurable end-to-end SWCNT junctions in-solution has yet to be demonstrated; this would allow the facile fabrication of carbon nanotube-based stimuli-responsive

molecular systems and devices. To address this challenge, we have developed a strategy combining photo-activated cycloaddition reaction with dynamic DNA nanostructures to realize stimuli-responsive CNT junctions.[122]

1.3 DNA nanotechnology

1.3.1 Background

DNA is the molecule that stores and transmits genetic information in biological systems and the field of DNA nanotechnology takes this molecule out of its biological context and uses its information to assemble structural motifs and then to connect them together. This field has had a remarkable impact on nanoscience and nanotechnology, and has been revolutionary in improving our ability to control molecular self-assembly.

DNA is the genetic information carrier for all known living organisms and some viruses. It is a biopolymer of nucleotides, with each nucleotide containing one of four nucleobases: cytosine (C), guanine (G), adenine (A), or thymine (T); a deoxyribose; and a phosphate group. The interaction between two DNA biopolymers or strands is determined by the coding of bases, known as Watson–Crick base pairing,[123] where A pairs with T and C pairs with G through hydrogen bonding. Massive amounts of information, genetic or nongenetic,[124] can be stored in a piece of DNA with defined sequences.

Intriguingly, from a material science perspective, the unique characteristics of DNA make it a promising material candidate for a wide range of applications. Since interactions between DNA molecules are specifically governed by Watson–Crick base

pairing, DNA has the most predictable and programmable interactions of any natural or synthetic molecule. It possesses remarkable binding specificity and thermodynamic stability and owns a library of nearly infinite choices of sequences to build versatile nanostructures. It is also structurally well-defined on the nanometre scale and has a persistence length of about 50 nm under conventional conditions. These incomparable features have led to the foundation of DNA nanotechnology. DNA nanotechnology is the field in which DNA (or RNA) molecules are utilized as building blocks for self-assembly into artificial nanostructures. Its conceptual emergence can be traced to 1982, when Seeman[16] proposed utilizing DNA structures to aid the crystallization of proteins. Three decades of development have led to the use of DNA as a designer molecule with an enormous capacity to construct both static and dynamic nanostructures with unprecedented precision and complexity. These DNA nanostructures are a set of materials with unique properties (e.g., well-defined size, geometry, interactions) that can be utilized on their own or be combined with other materials for many biomedical applications. For example, pristine DNA nanostructures have been used to interact with biological systems to enable biosensing,[125] bioimaging,[126] or drug delivery.[127]

1.3.2 DNA nanostructures

1.3.2.1 Static DNA nanostructures

Based on the fully complementary double helix, static DNA nanostructures such as DNA tiles and DNA origami have been designed and built by researchers in the field. DNA tiles are a set of artificial structures composed of several DNA single strands with unique sequences, whose hierarchical assembly leads to the formation of large DNA structures. Seeman et al.[128] reported the first DNA tile, named the immobile four-way

junction, that was built from four single DNA strands (***Figure 1-11 a***). This DNA tile closely resembles the natural Holliday junction, in which strand migration is prevented by minimizing the sequence symmetry in the junction. Three-, five-, six-, eight-, and 12-way junctions have been constructed via the same strategy.[129–131] Nevertheless, such DNA tiles failed to assemble into higher-order structures due to significant structural flexibility both on and off the tile plane. Rigid DNA double-crossover (DX) structures were then proposed and fabricated.[132] In these structures, two four-way junctions are confined within two parallel DNA double helices by two crossovers (***Figure 1-11 b***). In 1998, a two-dimensional (2D) DNA crystal structure was fabricated through sticky-end mediated assembly of a two-arm DX tile.[133] This was the first example of a higher-order crystal-like structure assembled from DNA, representing a milestone in the field of structural DNA nanotechnology.

Origami refers to the art of folding and sculpting flat paper into objects with arbitrary shapes. The idea of making DNA origami, reported by Rothemund[134] in 2006, creates similar art at the nanoscale. In the molecular self-folding process, a long ssDNA (scaffold DNA), typically the M13 bacteriophage genome DNA (∼7,000 nt), is folded into designed objects with well-defined geometry by hundreds of synthetic, short (20–60 nt) ssDNAs (known as staple DNAs).

Two distinct DNA origami design strategies have been developed so far: lattice-based origami and wire-frame origami (***Figure 1-11 c***). These methods differ in the arrangement of helices within the DNA origami objects. Earlier DNA origami studies built upon the lattice-like packing of DNA helices, in which the helices were closely

packed into square [134,135] honeycomb,[136] hexagonal or hybrid lattices.[137] Flat 2D objects, such as the famous smiley face (***Figure 1-11 d-i***), were the first to be constructed.[134] Further folding of flat 2D origami sheets led to the formation of hollow 3D containers, such as a DNA box (***Figure 1-11 d-ii***)[138] and a tetrahedron.[139] In contrast to lattice-based DNA origami, wire-frame DNA origami produces porous structures by minimizing the packing of DNA helices. Bathe and colleagues[140] developed an algorithm named DAEDALUS that enabled the automated design of a large library of polyhedral structures (***Figure 1-11 d-iii***). Hogberg and colleagues[141] reported an alternative wire-frame strategy that renders designed objects into meshes. 3D objects, such as the Stanford bunny (***Figure 1-11 d-iv***), have been fabricated through this method. Wire-frame DNA origami excels at constructing arbitrary-shaped, soft, and porous structures.

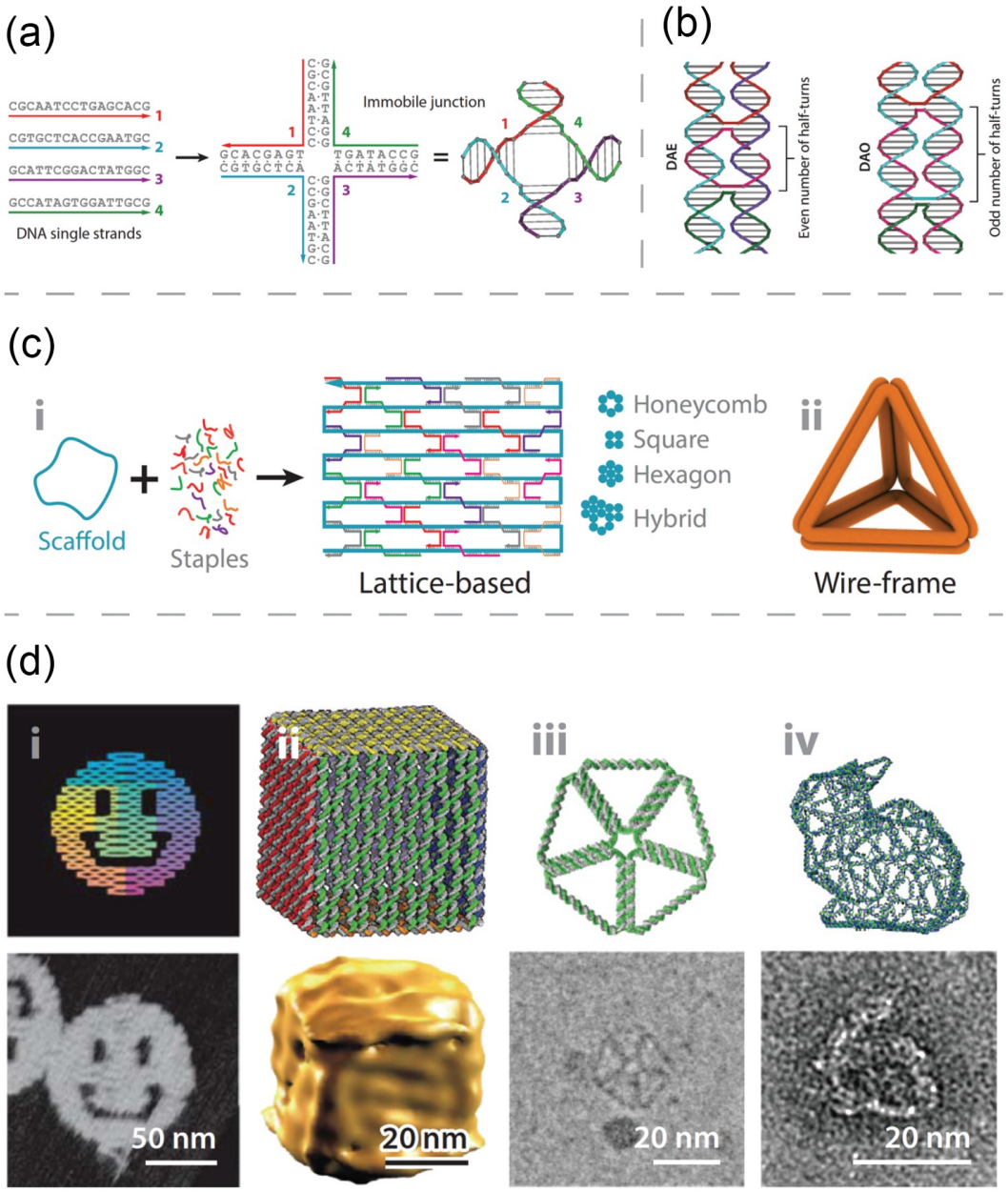

Figure 1-11. *Static nanostructures assembled from DNA tiles and DNA origami. (a) Artificial immobile junction assembled from four DNA strands. (b) Rigid double-crossover structures. (c) Two basic DNA origami design strategies: lattice-based versus wire-frame origami. (d-i & d-ii) Representative two-dimensional (2D) and three-dimensional (3D) objects assembled from lattice-based DNA origami. (d-iii & d-iv) Representative 2D and 3D objects assembled from wire-frame DNA origami.*

1.3.2.2 Dynamic DNA nanostructures

The possibility to reversibly control the structures of nucleic acids, the stability of duplex nucleic acids and the ability to design precise complex geometry at the molecular scale renders structural DNA nanotechnology capable of constructing nanomaterials, devices, and machinery that can sense, respond to, and navigate the local environment; transfer motion, forces, and energy; and process and communicate information. Constructing dynamic DNA-based devices with these functions generally requires integrating various underlying components with a range of mechanical and chemical properties, including flexibility and biochemical addressability.[142,143]

In addition to the well-established duplex structures of oligonucleotides originating from complementary base-pairing, with designed internal properties, other DNA structures could be induced by specific external triggers. For instance, cytosine-rich strands self-assemble under acidic conditions into intercalated structures (known as "i-motif"),[144] that dissociate at neutral pH values, while G-quadruplex[145] structures (helical guanine tetrads formed from guanine-rich nucleic acid sequences) are stabilized by K^+. Similarly, triplex formation bridged by C+•G-C or T•A-T complexes, undergo pH-induced formation or dissociation.[146,147] ***Figure 1-12*** illustrates the concept of a DNA switch while exemplifying the pH-induced reversible functions of the DNA switch. In this example, a cytosine-rich sequence is subjected to an acidic pH value (pH=5) that triggers the formation of the i-motif quadruplex structure stabilized by the homo-cytosine base-pair depicted in the inset. Neutralization of the pH (pH=7) destabilizes the i-motif structure and restores the random coil state of the nucleic acid.[144]

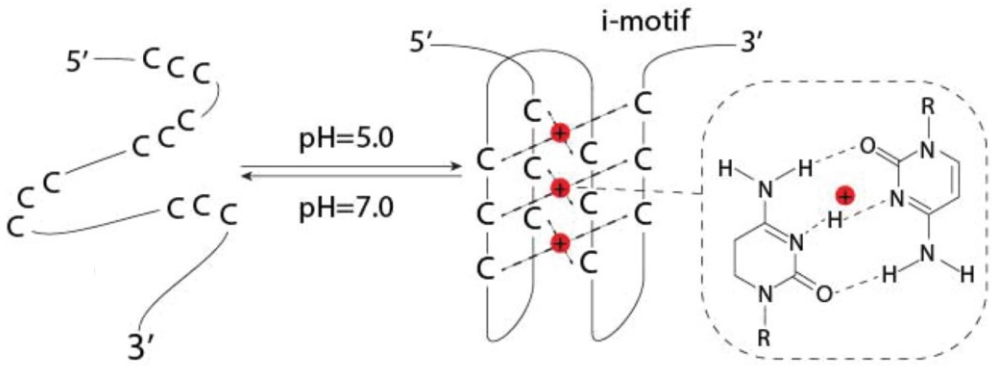

Figure 1-12. *The i-motif DNA structure and the pH induced reconfiguration process: cytosine-rich strands self-assemble under acidic conditions (pH 5 in the scheme) into intercalated structures (known as "i-motif") which will then dissociate at neutral pH values (pH 7 in the scheme).*

Another important stimulus that can trigger the dynamic process and reconfiguration of DNA structures is nucleic acid itself.[148,149] In 2000, the concept of isothermal DNA strand displacement was first introduced, which became essential to the construction of many DNA machines.[150] In this concept, a DNA "tweezer" (***Figure 1-13 a***) is closed by the addition of DNA "fuel" strands and re-opened with a different DNA strand, with the mechanical motion measured by fluorescence energy transfer between two dyes. The notion is that an unpaired 'toehold' extension to a motif component on the machine can bind to the complete complement of the strand. Upon binding, when the toehold is sufficiently long (usually about eight nucleotides), the complement will branch and migrate to the other end of the strand, thereby removing the strand from the motif because more nucleotide pairs are formed. A DNA actuator that was introduced into a 2D tile lattice enabled switching of the entire lattice between a stretched and a compact conformation.[151] In a different concept — "hybridization chain reaction" — hairpin DNA monomers assemble only when a trigger DNA strand is added. More specifically,

the trigger strand opens the first hairpin, which can then open the second hairpin, which in turn opens the first, and so on (***Figure 1-13 b***). As a result , the DNA assembly can be triggered and amplified autonomously.[152,153]

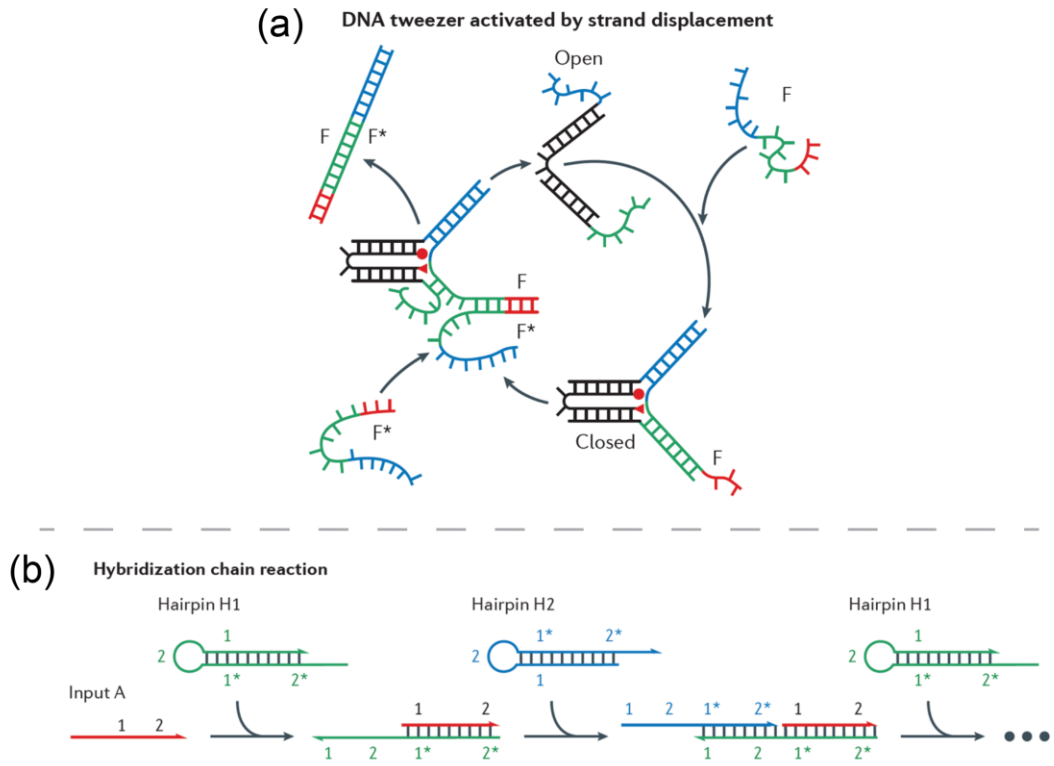

Figure 1-13. *Dynamic DNA systems based on strand-displacement principle. (a) A DNA tweezer. In the open form (top), the two fluorophores are separated. Strand F brings the blue and green strands together and closes the tweezer, increasing fluorescence resonance energy transfer (FRET). Strand F* removes F by strand displacement, restoring the open form of the tweezer. Asterisks denote complementary DNA sequences.*[150] *(b) Hybridization chain reaction. Hairpin DNA monomers H1 and H2 stay closed until input strand A is introduced. This strand opens H1, revealing a region that opens H2, which in turns opens H1, and so on, until a polymer is formed.*[152]

1.4 Summary

The synergistic effect from the combination of CNTs and DNA is a theme in nanoscience and nanotechnology. With their exceptional features, CNTs have been considered as one of the most promising nanomaterials for various future applications. On the other hand, the integration of DNA nanotechnology with CNTs has granted CNTs more flexibility and possibilities to build functional nanostructures.

In the following parts of this thesis, after briefly introducing the experimental methods that were used during related research works (Chapter 2), we will mainly focus on the assembly of functional CNT hybrid and CNT junction engineering. In particular, in Chapter 3 the use of DNA-CNT templates for the assembly of hybrid nanostructures with inorganic semiconducting materials in aqueous solutions and their application in optoelectronic devices is discussed. In Chapter 4, a facile approach for the fabrication of end-to-end SWCNT junctions exploiting DNA strands as the stimuli-responsive molecular linkers is presented. In addition to the application of oligonucleotides, in Chapter 5 an efficient way to sort DNA-CNTs by length via a gel electrophoresis technique (confirmed by AFM) is developed, which further facilitated the analysis of CNT junction formation with diazonium salt in our laboratory. Finally, in Chapter 6 the thesis will be summarized and concluded with the addressing of future challenges in the field.

1.5 References

1. S. Iijima. Hellical microtubules of graphitic carbon. *Nature* **354**, 56–58 (1991).

2. Iijima, S. & Ichihashi, T. Single-shell carbon nanotubes of 1-nm diameter. *Nature* **363**, 603–605 (1993).

3. Saito, R. & Dresselhaus, M. S. *Optical Properties of Carbon Nanotubes*. *Carbon Nanotubes and Graphene: Edition 2* (2014). doi:10.1016/B978-0-08-098232-8.00005-X

4. Popov, V. N. Carbon nanotubes: Properties and application. *Materials Science and Engineering R: Reports* **43**, 61–102 (2004).

5. Bachilo, S. M. *et al. Structure-assigned optical spectra of single-walled carbon nanotubes*. *Science* **298**, (Wiley, 2002).

6. Nanot, S., Hároz, E. H., Kim, J. H., Hauge, R. H. & Kono, J. Optoelectronic properties of single-wall carbon nanotubes. *Advanced Materials* **24**, 4977–4994 (2012).

7. Dai, H. Carbon nanotubes: Synthesis, integration, and properties. *Acc. Chem. Res.* **35**, 1035–1044 (2002).

8. Tasis, D., Tagmatarchis, N., Bianco, A. & Prato, M. Chemistry of carbon nanotubes. *Chemical Reviews* **106**, 1105–1136 (2006).

9. R. Moussaddar, A. Charlier, E. McRae, R. Heyd, M. F. C. Band theory and electronic structures of carbon nanotubes. *Synth. Met.* **89**, 81–86 (1997).

10. Tans, S. J. *et al.* Individual single-wall carbon nanotubes as quantum wires. *Nature* **386**, 474–477 (1997).

11. Journet, C. *et al.* Large-scale production of single-walled carbon nanotubes by the electric-arc technique. *Nature* **388**, 756–758 (1997).

12. Wildöer, J. W. G., Venema, L. C., Rinzler, A. G., Smalley, R. E. & Dekker, C. Electronic structure of atomically resolved carbon nanotubes. *Nature* **391**, 59–62 (1998).

13. Odom, T. W., Huang, J.-L., Kim, P. & Lieber, C. M. Structure and Electronic Properties

of Carbon Nanotubes. *J. Phys. Chem. B* **104**, 2794–2809 (2000).

14. Sun, Y. P., Fu, K., Lin, Y. & Huang, W. Functionalized carbon nanotubes: Properties and applications. *Acc. Chem. Res.* **35**, 1096–1104 (2002).

15. Popov, V. N. Carbon nanotubes: Properties and application. *Mater. Sci. Eng. R Reports* **43**, 61–102 (2004).

16. Seeman, N. C. Nucleic acid junctions and lattices. *J. Theor. Biol.* **99**, 237–247 (1982).

17. Pinheiro, A. V., Han, D., Shih, W. M. & Yan, H. Challenges and opportunities for structural DNA nanotechnology. *Nature Nanotechnology* **6**, 763–772 (2011).

18. Jorio, A. et al. Carbon nanotubes: Advanced topics in the synthesis, structure, properties and applications. *Mater. Today* **11**, 57 (2008).

19. Geim, A. K. & Novoselov, K. S. The rise of graphene. *Nat. Mater.* **6**, 183–191 (2007).

20. Castro Neto, A. H., Guinea, F., Peres, N. M. R., Novoselov, K. S. & Geim, A. K. The electronic properties of graphene. *Rev. Mod. Phys.* **81**, 109–162 (2009).

21. Terrones, M. Carbon Nanotubes and Related Structures: New materials for the Twenty-first Century. *Carbon N. Y.* **38**, 787–788 (2000).

22. Roth, S. & Carroll, D. *One-dimensional metals: Conjugated polymers, organic crystals, carbon nanotubes and graphene*. *One-Dimensional Metals: Conjugated Polymers, Organic Crystals, Carbon Nanotubes and Graphene* (2015). doi:10.1002/9783527690176

23. Guldi, D. M. *et al.* CNT-CdTe versatile donor-acceptor nanohybrids. *J. Am. Chem. Soc.* **128**, 2315–2323 (2006).

24. Joselevich, E. Electronic structure and chemical reactivity of carbon nanotubes: A Chemist's view. *ChemPhysChem* **5**, 619–624 (2004).

25. Samsonidze, G. G. *et al.* The concept of cutting lines in carbon nanotube science.

Journal of Nanoscience and Nanotechnology **3**, 431–458 (2003).

26. Mintmire, J. W., Dunlap, B. I. & White, C. T. Are fullerene tubules metallic? *Phys. Rev. Lett.* **68**, 631–634 (1992).

27. Zhang, Y., Gu, H. & Iijima, S. Single-wall carbon nanotubes synthesized by laser ablation in a nitrogen atmosphere. *Appl. Phys. Lett.* **73**, 3827–3829 (1998).

28. Kumar, M. & Ando, Y. Chemical vapor deposition of carbon nanotubes: A review on growth mechanism and mass production. *Journal of Nanoscience and Nanotechnology* **10**, 3739–3758 (2010).

29. Balasubramanian, K. & Burghard, M. Chemically functionalized carbon nanotubes. *Small* **1**, 180–192 (2005).

30. Sanchez-Valencia, J. R. *et al.* Controlled synthesis of single-chirality carbon nanotubes. *Nature* **512**, 61–64 (2014).

31. Baddour, C. E. & Briens, C. Carbon Nanotube Synthesis: A Review : International Journal of Chemical Reactor Engineering. *Int. J. Chem. React. Eng.* **3**, (2005).

32. Doorn, S. K. *et al.* High resolution capillary electrophoresis of carbon nanotubes. *J. Am. Chem. Soc.* **124**, 3169–3174 (2002).

33. Doorn, S. K. *et al.* Capillary electrophoresis separations of bundled and individual carbon nanotubes. *J. Phys. Chem. B* **107**, 6063–6069 (2003).

34. Heller, D. A. *et al.* Concomitant length and diameter separation of single-walled carbon nanotubes. *J. Am. Chem. Soc.* **126**, 14567–14573 (2004).

35. Niyogi, S. *et al.* Chromatographic purification of soluble single-walled carbon nanotubes (s-SWNTs) [1]. *Journal of the American Chemical Society* **123**, 733–734 (2001).

36. Farkas, E., Elizabeth Anderson, M., Chen, Z. & Rinzler, A. G. Length sorting cut single

wall carbon nanotubes by high performance liquid chromatography. *Chem. Phys. Lett.* **363**, 111–116 (2002).

37. Huang, X., Mclean, R. S. & Zheng, M. High-resolution length sorting and purification of DNA-wrapped carbon nanotubes by size-exclusion chromatography. *Anal. Chem.* **77**, 6225–6228 (2005).

38. Zheng, M. *et al.* DNA-assisted dispersion and separation of carbon nanotubes. *Nat. Mater.* **2**, 338–342 (2003).

39. Tu, X., Manohar, S., Jagota, A. & Zheng, M. DNA sequence motifs for structure-specific recognition and separation of carbon nanotubes. *Nature* **460**, 250–253 (2009).

40. Arnold, M. S., Stupp, S. I. & Hersam, M. C. Enrichment of single-walled carbon nanotubes by diameter in density gradients. *Nano Lett.* **5**, 713–718 (2005).

41. Khripin, C. Y., Fagan, J. A. & Zheng, M. Spontaneous partition of carbon nanotubes in polymer-modified aqueous phases. *J. Am. Chem. Soc.* **135**, 6822–6825 (2013).

42. Albertsson, P. Partition of cell particles and macromolecules in polymer two-phase systems. *Adv. Protein Chem.* **24**, 309–341 (1970).

43. Tasis, D., Tagmatarchis, N., Georgakilas, V. & Prato, M. Soluble carbon nanotubes. *Chemistry - A European Journal* **9**, 4000–4008 (2003).

44. Thostenson, E. T., Ren, Z. & Chou, T. W. Advances in the science and technology of carbon nanotubes and their composites: A review. *Compos. Sci. Technol.* **61**, 1899–1912 (2001).

45. Dai, L. & Mau, A. W. H. Controlled synthesis and modification of carbon nanotubes and C60: Carbon nanostructures for advanced polymeric composite materials. *Adv. Mater.* **13**, 899–913 (2001).

46. Hirsch, A. Functionalization of single-walled carbon nanotubes. *Angewandte Chemie -*

International Edition **41**, 1853–1859 (2002).

47. Fischer, J. E. Chemical doping of single-wall carbon nanotubes. *Acc. Chem. Res.* **35**, 1079–1086 (2002).

48. Niyogi, S. *et al.* Chemistry of single-walled carbon nanotubes. *Acc. Chem. Res.* **35**, 1105–1113 (2002).

49. Banerjee, S., Kahn, M. G. C. & Wong, S. S. Rational chemical strategies for carbon nanotube functionalization. *Chemistry - A European Journal* **9**, 1898–1908 (2003).

50. De La Torre, G., Blau, W. & Torres, T. A survey on the functionalization of single-walled nanotubes. The chemical attachment of phthalocyanine moieties. *Nanotechnology* **14**, 765–771 (2003).

51. Davis, J. J., Coleman, K. S., Azamian, B. R., Bagshaw, C. B. & Green, M. L. H. Chemical and biochemical sensing with modified single walled carbon nanotubes. *Chemistry - A European Journal* **9**, 3732–3739 (2003).

52. An, K. H. *et al.* Structural transformation of fluorinated carbon nanotubes induced by in situ electron-beam irradiation. *J. Am. Chem. Soc.* **125**, 3057–3061 (2003).

53. Jaffe, R. L. Quantum Chemistry Study of Fullerene and Carbon Nanotube Fluorination. *J. Phys. Chem. B* **107**, 10378–10388 (2003).

54. Mickelson, E. T. *et al.* Fluorination of single-wall carbon nanotubes. *Chem. Phys. Lett.* **296**, 188–194 (1998).

55. Lee, K. M., Li, L. & Dai, L. Asymmetric end-functionalization of multi-walled carbon nanotubes. *J. Am. Chem. Soc.* **127**, 4122–4123 (2005).

56. Moghaddam, M. J. *et al.* Highly Efficient Binding of DNA on the Sidewalls and Tips of Carbon Nanotubes Using Photochemistry. *Nano Lett.* **4**, 89–93 (2004).

57. Chen, Y. *et al.* Chemical attachment of organic functional groups to single-walled

carbon nanotube material. *J. Mater. Res.* **13**, 2423–2431 (1998).

58. Balasubramanian, K., Sordan, R., Burghard, M. & Kern, K. A selective electrochemical approach to carbon nanotube field-effect transistors. *Nano Lett.* **4**, 827–830 (2004).

59. Balasubramanian, K. *et al.* Electrical transport and confocal Raman studies of electrochemically modified individual carbon nanotubes. *Adv. Mater.* **15**, 1515–1518 (2003).

60. Kooi, S. E., Schlecht, U., Burghard, M. & Kern, K. Electrochemical modification of single carbon nanotubes. *Angew. Chemie - Int. Ed.* **41**, 1353–1355 (2002).

61. Strano, M. S. *et al.* Electronic structure control of single-waited carbon nanotube functionalization. *Science (80-.).* **301**, 1519–1522 (2003).

62. Hamon, M. A., Hui, H., Bhowmik, P., Itkis, H. M. E. & Haddon, R. C. Ester-functionalized soluble single-walled carbon nanotubes. *Appl. Phys. A Mater. Sci. Process.* **74**, 333–338 (2002).

63. Chen, J. *et al.* Dissolution of full-length single-walled carbon nanotubes. *J. Phys. Chem. B* **105**, 2525–2528 (2001).

64. Tasis, D., Tagmatarchis, N., Bianco, A. & Prato, M. Chemistry of carbon nanotubes. *Chem. Rev.* **106**, 1105–1136 (2006).

65. Dyke, C. A. & Tour, J. M. Unbundled and highly functionalized carbon nanotubes from aqueous reactions. *Nano Lett.* **3**, 1215–1218 (2003).

66. Strano, M. S. Probing Chiral Selective Reactions Using a Revised Kataura Plot for the Interpretation of Single-Walled Carbon Nanotube Spectroscopy. *J. Am. Chem. Soc.* **125**, 16148–16153 (2003).

67. Ernst, F. *et al.* Noncovalent Stable Functionalization Makes Carbon Nanotubes Hydrophilic and Biocompatible. *J. Phys. Chem. C* **121**, 18887–18891 (2017).

68. Fernandes, R. M. F., Dai, J., Regev, O., Marques, E. F. & Furó, I. Block Copolymers as Dispersants for Single-Walled Carbon Nanotubes: Modes of Surface Attachment and Role of Block Polydispersity. *Langmuir* **34**, 13672–13679 (2018).

69. Fernandes, R. M. F., Buzaglo, M., Regev, O., Marques, E. F. & Furó, I. Surface Coverage and Competitive Adsorption on Carbon Nanotubes. *J. Phys. Chem. C* **119**, 22190–22197 (2015).

70. Zheng, M. *et al.* Structure-based carbon nanotube sorting by sequence-dependent DNA assembly. *Science* **302**, 1545–8 (2003).

71. Roxbury, D., Jagota, A. & Mittal, J. Structural characteristics of oligomeric DNA strands adsorbed onto single-walled carbon nanotubes. *J. Phys. Chem. B* **117**, 132–140 (2013).

72. Roxbury, D., Jagota, A. & Mittal, J. Sequence-specific self-stitching motif of short single-stranded DNA on a single-walled carbon nanotube. *J. Am. Chem. Soc.* **133**, 13545–13550 (2011).

73. Attanzio, A. *et al.* Carbon Nanotube-Quantum Dot Nanohybrids: Coupling with Single-Particle Control in Aqueous Solution. *Small* **13**, (2017).

74. Eder, D. Carbon nanotube-inorganic hybrids. *Chem. Rev.* **110**, 1348–1385 (2010).

75. Shearer, C. J., Cherevan, A. & Eder, D. Application and future challenges of functional nanocarbon hybrids. *Adv. Mater.* **26**, 2295–2318 (2014).

76. Padgaonkar, S., Olding, J. N., Lauhon, L. J., Hersam, M. C. & Weiss, E. A. Emergent Optoelectronic Properties of Mixed-Dimensional Heterojunctions. *Acc. Chem. Res.* **53**, 763–772 (2020).

77. Zhang, X., Hou, L. & Samorì, P. Coupling carbon nanomaterials with photochromic molecules for the generation of optically responsive materials. *Nature Communications* **7**, (2016).

78. Peng, X., Chen, J., Misewich, J. A. & Wong, S. S. Carbon nanotube–nanocrystal heterostructures. *Chem. Soc. Rev.* **38**, 1076 (2009).

79. Freeley, M. *et al.* Tuning the Coupling in Single-Molecule Heterostructures: DNA-Programmed and Reconfigurable Carbon Nanotube-Based Nanohybrids. *Adv. Sci.* **5**, (2018).

80. Eder, D. Carbon nanotube-inorganic hybrids. *Chem. Rev.* **110**, 1348–1385 (2010).

81. Hammel, E. *et al.* Carbon nanofibers for composite applications. in *Carbon* **42**, 1153–1158 (2004).

82. Zaporotskova, I. V., Boroznina, N. P., Parkhomenko, Y. N. & Kozhitov, L. V. Carbon nanotubes: Sensor properties. A review. *Mod. Electron. Mater.* **2**, 95–105 (2016).

83. Kamat, P. V. *et al.* Self-assembled linear bundles of single wall carbon nanotubes and their alignment and deposition as a film in a dc field. *J. Am. Chem. Soc.* **126**, 10757–10762 (2004).

84. Girishkumar, G., Vinodgopal, K. & Kamat, P. V. Carbon nanostructures in portable fuel cells: Single-walled carbon nanotube electrodes for methanol oxidation and oxygen reduction. *J. Phys. Chem. B* **108**, 19960–19966 (2004).

85. Wang, C. *et al.* Proton Exchange Membrane Fuel Cells with Carbon Nanotube Based Electrodes. *Nano Lett.* **4**, 345–348 (2004).

86. Arnold, M. S. *et al.* Recent developments in the photophysics of single-walled carbon nanotubes for their use as active and passive material elements in thin film photovoltaics. *Physical Chemistry Chemical Physics* **15**, 14896–14918 (2013).

87. Gaviria Rojas, W. A. & Hersam, M. C. Chirality-Enriched Carbon Nanotubes for Next-Generation Computing. *Adv. Mater.* 1905654 (2020). doi:10.1002/adma.201905654

88. Lesiak, A. *et al.* Optical sensors based on II-VI quantum dots. *Nanomaterials* **9**, 192

(2019).

89. Moreels, I. *et al.* Size-dependent optical properties of colloidal PbS quantum dots. *ACS Nano* **3**, 3023–3030 (2009).

90. Clifford, J. P. *et al.* Fast, sensitive and spectrally tuneable colloidal-quantum-dot photodetectors. *Nat. Nanotechnol.* **4**, 40–44 (2009).

91. Schulz-Drost, C. *et al.* Innovative inorganic-organic nanohybrid materials: Coupling quantum dots to carbon nanotubes. *Angew. Chemie - Int. Ed.* **49**, 6425–6429 (2010).

92. Robel, I., Bunker, B. A. & Kamat, P. V. Single-walled carbon nanotube-CdS nanocomposites as light-harvesting assemblies: Photoinduced charge-transfer interactions. *Adv. Mater.* **17**, 2458–2463 (2005).

93. Hu, L. *et al.* Light-induced charge transfer in pyrene/CdSe-SWNT hybrids. *Adv. Mater.* **20**, 939–946 (2008).

94. Li, X., Jia, Y. & Cao, A. Tailored single-walled carbon nanotube-CdS nanoparticle hybrids for tunable optoelectronic devices. *ACS Nano* **4**, 506–512 (2010).

95. Saran, R. & Curry, R. J. Lead sulphide nanocrystal photodetector technologies. *Nature Photonics* **10**, 81–92 (2016).

96. Wang, D. *et al.* Controlled fabrication of pbs quantum-dot/carbon-nanotube nanoarchitecture and its significant contribution to near-infrared photon-to-current conversion. *Adv. Funct. Mater.* **21**, 4010–4018 (2011).

97. Ka, I., Le Borgne, V., Ma, D. & El Khakani, M. A. Pulsed laser ablation based direct synthesis of single-wall carbon nanotube/PbS quantum dot nanohybrids exhibiting strong, spectrally wide and fast photoresponse. *Adv. Mater.* **24**, 6289–6294 (2012).

98. Ka, I. *et al.* Multiple exciton generation induced enhancement of the photoresponse of pulsed-laser-ablation synthesized single-wall-carbon-nanotube/PbS-quantum-dots

nanohybrids. *Sci. Rep.* **6**, (2016).

99. Feng, W. *et al.* A layer-nanostructured assembly of PbS quantum dot/multiwalled carbon nanotube for a high-performance photoswitch. *Sci. Rep.* **4**, (2014).

100. Palma, M. *et al.* Controlled formation of carbon nanotube junctions via linker-induced assembly in aqueous solution. *J. Am. Chem. Soc.* **135**, 8440–8443 (2013).

101. Zhu, J. *et al.* Solution-Processable Carbon Nanoelectrodes for Single-Molecule Investigations. *J. Am. Chem. Soc.* **138**, 2905–2908 (2016).

102. McMorrow, J., Freeley, M. & Palma, M. DNA-Wrapped Single-Walled Carbon Nanotube Assemblies. *Ind. Eng. Chem. Res.* **56**, 5302–5308 (2017).

103. Zhen, Y., Postma, H. W. C., Balents, L. & Dekker, C. Carbon nanotube intramolecular junctions. *Nature* **402**, 273–276 (1999).

104. Fuhrer, M. S. *et al.* Crossed nanotube junctions. *Science (80-.).* **288**, 494–497 (2000).

105. Park, H. *et al.* High-density integration of carbon nanotubes via chemical self-assembly. *Nat. Nanotechnol.* **7**, 787–791 (2012).

106. Cao, Q. & Rogers, J. A. Ultrathin films of single-walled carbon nanotubes for electronics and sensors: A review of fundamental and applied aspects. *Advanced Materials* **21**, 29–53 (2009).

107. Park, S., Vosguerichian, M. & Bao, Z. A review of fabrication and applications of carbon nanotube film-based flexible electronics. *Nanoscale* **5**, 1727–1752 (2013).

108. Freeley, M. *et al.* Site-Specific One-to-One Click Coupling of Single Proteins to Individual Carbon Nanotubes: A Single-Molecule Approach. *J. Am. Chem. Soc.* **139**, 17834–17840 (2017).

109. Feldman, A. K., Steigerwald, M. L., Guo, X. & Nuckolls, C. Molecular electronic devices based on single-walled carbon nanotube electrodes. *Acc. Chem. Res.* **41**, 1731–

1741 (2008).

110. Guo, X. Single-molecule electrical biosensors based on single-walled carbon nanotubes. *Adv. Mater.* **25**, 3397–3408 (2013).

111. Xiang, D., Wang, X., Jia, C., Lee, T. & Guo, X. Molecular-Scale Electronics: From Concept to Function. *Chem. Rev.* **116**, 4318–4440 (2016).

112. Weizmann, Y., Chenoweth, D. M. & Swager, T. M. Addressable terminally linked DNA-CNT nanowires. *J. Am. Chem. Soc.* **132**, 14009–14011 (2010).

113. Oruc, B., Celik, S., Hayat Soytas, S. & Unal, H. DNA Directed Self-Assembly of Single Walled Carbon Nanotubes into Three-Way Junction Nanostructures. *ACS Omega* **3**, 4157–4162 (2018).

114. J. Wind, S. *et al.* Integrating DNA with Functional Nanomaterials. *J. Self-Assembly Mol. Electron.* **1**, 177–194 (2013).

115. Xu, X. *et al.* Reconfigurable Carbon Nanotube Multiplexed Sensing Devices. *Nano Lett.* **18**, 4130–4135 (2018).

116. Geier, M. L. *et al.* Solution-processed carbon nanotube thin-film complementary static random access memory. *Nat. Nanotechnol.* **10**, 944–948 (2015).

117. Brady, G. J. *et al.* Quasi-ballistic carbon nanotube array transistors with current density exceeding Si and GaAs. *Sci. Adv.* **2**, (2016).

118. Jin, C., Suenaga, K. & Iijima, S. Plumbing carbon nanotubes. *Nat. Nanotechnol.* **3**, 17–21 (2008).

119. Clément, P. *et al.* A one-step chemical strategy for the formation of carbon nanotube junctions in aqueous solution: Reaction of DNA-wrapped carbon nanotubes with diazonium salts. *Chempluschem* **84**, 1235–1238 (2019).

120. A.P.Alivisatos. Semiconductor Clusters, Nanocrystals, and Quantum Dots. *Science*

(80-.). **271**, (1996).

121. Baker, S. N. & Baker, G. A. Luminescent carbon nanodots: Emergent nanolights. *Angewandte Chemie - International Edition* **49**, 6726–6744 (2010).

122. Amoroso, G. *et al.* DNA-Powered Stimuli-Responsive Single-Walled Carbon Nanotube Junctions. *Chem. Mater.* **31**, 1537–1542 (2019).

123. Watson, J. D. & Crick, F. H. C. Molecular structure of nucleic acids: A structure for deoxyribose nucleic acid. *Nature* **171**, 737–738 (1953).

124. Shipman, S. L., Nivala, J., Macklis, J. D. & Church, G. M. CRISPR-Cas encoding of a digital movie into the genomes of a population of living bacteria. *Nature* **547**, 345–349 (2017).

125. Modi, S. *et al.* A DNA nanomachine that maps spatial and temporal pH changes inside living cells. *Nat. Nanotechnol.* **4**, 325–330 (2009).

126. Jungmann, R. *et al.* Multiplexed 3D cellular super-resolution imaging with DNA-PAINT and Exchange-PAINT. *Nat. Methods* **11**, 313–318 (2014).

127. Douglas, S. M., Bachelet, I. & Church, G. M. A logic-gated nanorobot for targeted transport of molecular payloads. *Science (80-.).* **335**, 831–834 (2012).

128. Kallenbach, N. R., Ma, R. I. & Seeman, N. C. An immobile nucleic acid junction constructed from oligonucleotides. *Nature* **305**, 829–831 (1983).

129. Ma, R. I., Kallenbach, N. R., Sheardy, R. D., Petrillo, M. L. & Seeman, N. C. Three-arm nucleic acid junctions are flexible. *Nucleic Acids Res.* **14**, 9745–9753 (1986).

130. Wang, Y., Mueller, J. E., Kemper, B. & Seeman, N. C. Assembly and Characterization of Five-Arm and Six-Arm DNA Branched Junctions. *Biochemistry* **30**, 5667–5674 (1991).

131. Wang, X. & Seeman, N. C. Assembly and characterization of 8-arm and 12-arm DNA

branched junctions. *J. Am. Chem. Soc.* **129**, 8169–8176 (2007).

132. Tsu-Ju, F. & Seeman, N. C. DNA Double-Crossover Molecules. *Biochemistry* **32**, 3211–3220 (1993).

133. Winfree, E., Liu, F., Wenzler, L. A. & Seeman, N. C. Design and self-assembly of two-dimensional DNA crystals. *Nature* **394**, 539–544 (1998).

134. Rothemund, P. W. K. Folding DNA to create nanoscale shapes and patterns. *Nature* **440**, 297–302 (2006).

135. Ke, Y. *et al.* Multilayer DNA origami packed on a square lattice. *J. Am. Chem. Soc.* **131**, 15903–15908 (2009).

136. Douglas, S. M. *et al.* Self-assembly of DNA into nanoscale three-dimensional shapes. *Nature* **459**, 414–418 (2009).

137. Ke, Y., Voigt, N. V., Gothelf, K. V. & Shih, W. M. Multilayer DNA origami packed on hexagonal and hybrid lattices. *J. Am. Chem. Soc.* **134**, 1770–1774 (2012).

138. Andersen, E. S. *et al.* Self-assembly of a nanoscale DNA box with a controllable lid. *Nature* **459**, 73–76 (2009).

139. Ke, Y. *et al.* Scaffolded DNA origami of a DNA tetrahedron molecular container. *Nano Lett.* **9**, 2445–2447 (2009).

140. Veneziano, R. *et al.* Designer nanoscale DNA assemblies programmed from the top down. *Science (80-.).* **352**, (2016).

141. Benson, E. *et al.* DNA rendering of polyhedral meshes at the nanoscale. *Nature* **523**, 441–444 (2015).

142. Wang, F., Lu, C. H. & Willner, I. From cascaded catalytic nucleic acids to enzyme-DNA nanostructures: Controlling reactivity, sensing, logic operations, and assembly of complex structures. *Chemical Reviews* **114**, 2881–2941 (2014).

143. Yan, H., Zhang, X., Shen, Z. & Seeman, N. C. A robust DNA mechanical device controlled by hybridization topology. *Nature* **415**, 62–65 (2002).

144. Gehring, K., Leroy, J. L. & Guéron, M. A tetrameric DNA structure with protonated cytosine-cytosine base pairs. *Nature* **363**, 561–565 (1993).

145. Sen, D. & Gilbert, W. Formation of parallel four-stranded complexes by guanine-rich motifs in DNA and its implications for meiosis. *Nature* **334**, 364–366 (1988).

146. Duca, M., Vekhoff, P., Oussedik, K., Halby, L. & Arimondo, P. B. The triple helix: 50 years later, the outcome. *Nucleic Acids Res.* **36**, 5123–5138 (2008).

147. Chan, P. P. & Glazer, P. M. Triplex DNA: Fundamentals, advances, and potential applications for gene therapy. *Journal of Molecular Medicine* **75**, 267–282 (1997).

148. Zhang, D. Y. & Winfree, E. Control of DNA strand displacement kinetics using toehold exchange. *J. Am. Chem. Soc.* **131**, 17303–17314 (2009).

149. Qian, L. & Winfree, E. Scaling up digital circuit computation with DNA strand displacement cascades. *Science (80-.).* **332**, 1196–1201 (2011).

150. Yurke, B., Turberfield, A. J., Mills, A. P., Simmel, F. C. & Neumann, J. L. A DNA-fuelled molecular machine made of DNA. *Nature* **406**, 605–608 (2000).

151. Feng, L., Park, S. H., Reif, J. H. & Yan, H. A two-state DNA lattice switched by DNA nanoactuator. *Angew. Chemie - Int. Ed.* **42**, 4342–4346 (2003).

152. Dirks, R. M. & Pierce, N. A. Triggered amplification by hybridization chain reaction. *Proc. Natl. Acad. Sci. U. S. A.* **101**, 15275–15278 (2004).

153. Yin, P., Choi, H. M. T., Calvert, C. R. & Pierce, N. A. Programming biomolecular self-assembly pathways. *Nature* **451**, 318–322 (2008).

Chapter 2

Experimental Techniques

In this chapter, the main experimental techniques exploited throughout the studies in the thesis will be introduced. As the valuable tool to directly confirm the assembly of CNT based nanohybrids, atomic force microscopy is first introduced. To gain further information of the nanocomponents and assembled materials (composition, band gap, excited state kinetics etc.), spectroscopy methods including steady-state absorption spectroscopy, transient absorption spectroscopy and steady-state fluorescence spectroscopy are discussed. At last, a brief introduction about the electrophoretic techniques that are used for the length sorting of DNA-CNTs and the manipulation of assembled hybrids between nano-electrodes will be presented.

2.1 Atomic force microscopy (AFM)

Atomic force microscopy (AFM), also called scanning force microscopy (SFM) is a type of scanning probe microscopy (SPM). Invented by Binning in 1986,[1] AFM allows the mapping of the topography/morphology of surfaces and interfaces with a vertical resolution approaching 0.1 nanometre and lateral resolution of no more than few tens of nanometres. The AFM system has evolved into a useful tool for direct measurements

of intermolecular forces with its featured atomic-resolution characterization that can be employed in a broad spectrum of applications such as electronics, semi-conductors, materials and manufacturing, polymers, biology and biomaterials.[2–4]

In AFM experiments, a sharp tip (with a radius usually smaller than 12 nm) is applied to probe the sample surface.[5] By measuring forces (typically of the van der Waals type) between the tip and surface at very short distances (0.2-10 nm probe-sample), AFM provides a 3D profile of the surface at the nanoscale. As depicted in ***Figure 2-1***, a typical AFM system consists of a micro-machined cantilever probe and a sharp tip mounted to a piezoelectric (PZT) actuator and a position sensitive photo detector for receiving a laser beam reflected off the end-point of the beam to provide cantilever deflection feedback. The basic principle of AFM operation is to scan the tip over the sample surface with feedback mechanisms that enable the PZT scanners to maintain the tip at a constant force, or constant height above the sample surface. As the tip scans the surface of the sample, moving up and down with the contour of the surface, the laser beam which reflects from the back side of the cantilever is detected by the photodetector. The position of the beam signal in the sensor measures the deflection of the cantilever and in turn the force. A feedback loop is introduced to maintain the tip at a constant height above the surface (depending on the working mode). In the constant force mode, the PZT transducer monitors real time height deviation. In the constant height mode, the deflection force on the sample is recorded.

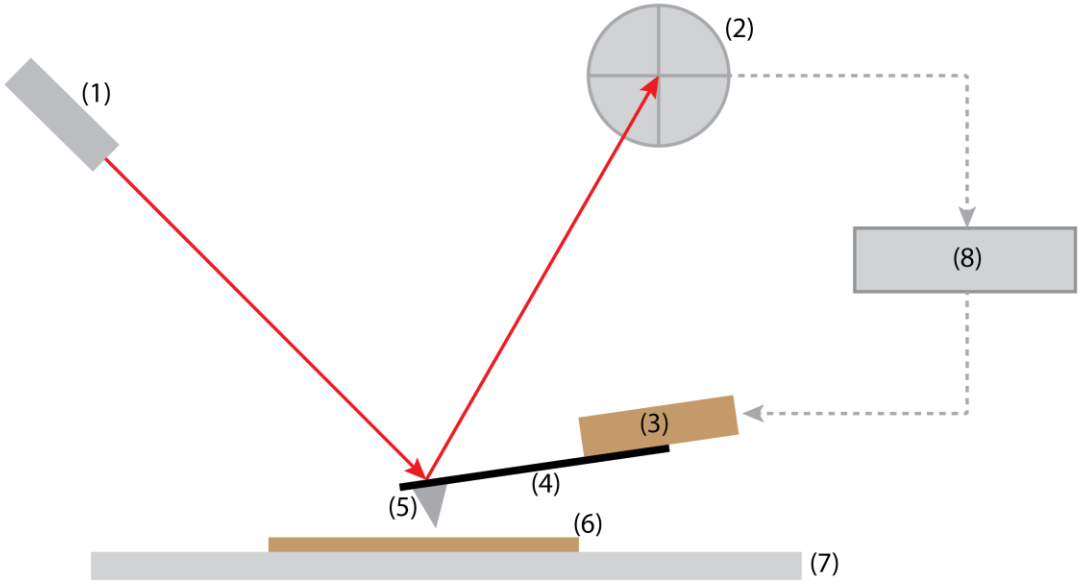

Figure 2-1. *The typical AFM configuration. The small spring-like cantilever (4) is carried by the support where a piezoelectric element (3) oscillates the cantilever (4) at its eigen frequency. The sharp tip (5) is fixed to the free end of the cantilever (4), acting as the probe. The detector (2) records the deflection and motion of the cantilever (4) through reflected laser beam from a laser source (1). The sample (6) is mounted on the sample stage (7). The feedback gained from detector (2) is processed by the controlling system (8) which then decides the motion of the piezoelectric actuator (3) according to the working mode of the AFM. Numbers in parentheses correspond to numbered elements of AFM in the scheme.*

According to the configuration described above, the interaction between tip and sample, which can be an atomic scale phenomenon, is transduced into changes of the motion of cantilever which, is a macro scale phenomenon. Therefore, the value of deflection is used to quantify the interaction between the tip and sample.

As for the description of the tip-sample interactions, the Lennard-Jones potential U_{L-J}.[6] is usually introduced:

$$U_{L-J}(r) = U_0\left[-2\left(\frac{r_0}{r}\right)^6 + \left(\frac{r_0}{r}\right)^{12}\right]$$

Here r is the tip-surface distance, r_0 the tip-surface distance at which the potential reaches its minimum, and U_0 is the minimal value of the potential. By taking the derivative of the potential over distance, the force between tip and surface can be obtained from the above equation. ***Figure 2-2*** graphically displays the relationship between tip-surface force and distance. In general, there are two regimes where different forces will dominate. At a very small distance (a few angstrom), a strong repulsive force appears between the tip and the sample atoms (which scales as r^{-12} in the above equation). The force originates from the exchange interactions due to the overlap of the electronic orbitals at atomic distances.

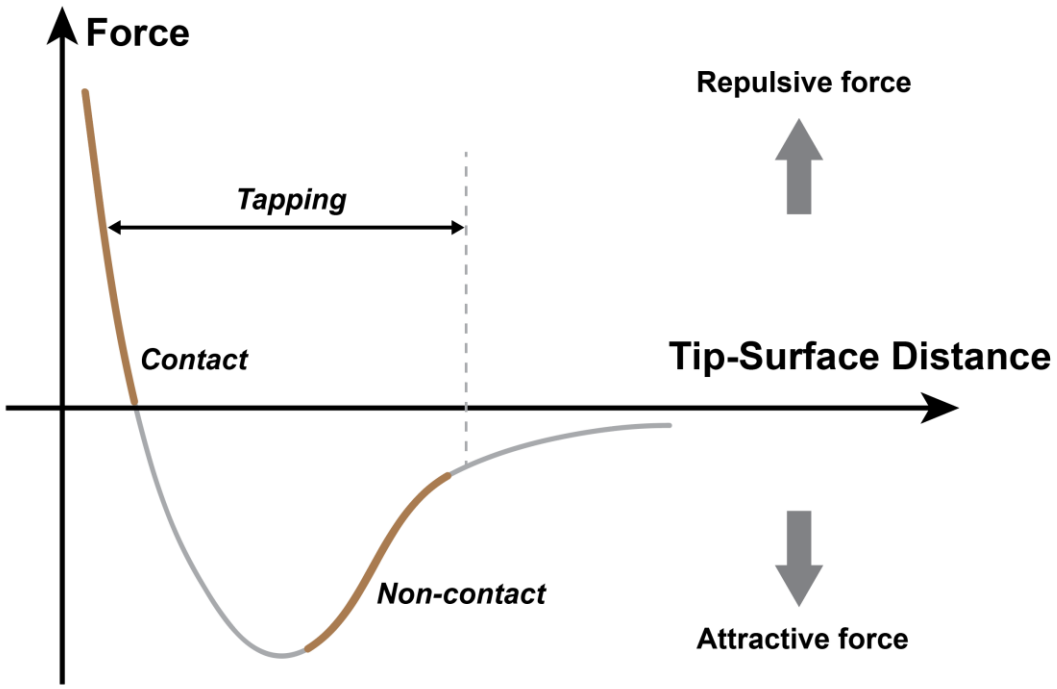

Figure 2-2. *Tip-surface force as the function of tip-surface distance (figure was optimized for better illustration from reference 2).*

When the repulsive force is dominant, the tip is said to be in "contact" with the sample. As the tip moves away from the surface, a polarisation interaction between atoms results in attraction between the tip and the sample surface (van der Waals).

Based on the type(s) of interactions involved, there are three main working modes for AFM: contact mode (distance < 0.5 nm), non-contact mode (0.5~2 nm) and tapping mode (1~10 nm). In contact mode, the tip is kept constant on the surface in the repulsive zone. Contours are measured using the feedback loop signal which is tuned to keep the cantilever at a constant position/force. For non-contact mode, the tip oscillates at the resonant frequency of the cantilever (about 100-400 kHz) and the oscillation amplitude (< 10 nm) is kept constant. As the tip approaches the surface, the van der Walls force acts to decrease resonant frequency which is then measured by the system. The

frequency deviation is then used to make an image of the sample. Non-contact mode exploits the r^{-6} dependence of tip-surface force interaction in the U_{L-J} expression.

Tapping mode is a combination of both contact and non-contact modes. Similar to non-contact mode, the cantilever is driven to oscillate up and down near its resonance frequency. The oscillation is achieved by a small piezoelectric element attached to the AFM tip holder. The amplitude of the oscillation varies between a few nm to 200 nm. The frequency and amplitude of the driving signal are kept constant so that the amplitude of oscillation should be the same if there is no interaction between the tip and surface. When the tip approaches the surface, it will "lightly" tap the surface which causes a decrease in oscillation amplitude. The amplitude is used for the feedback, and the vertical adjustments of the piezo scanner are recorded as the height information.

Benefitting from the oscillating contact, tapping mode can achieve an improved lateral resolution（~5nm）compared to non-contact mode, but without damaging a "soft" organic/biological surface as contact mode would. As is illustrated in ***Figure 2-3***, contact mode might damage the surface structure while non-contact mode has a lower resolution. Tapping mode benefits from the elimination of friction forces and preventing the tip from being "trapped" by surface structures.

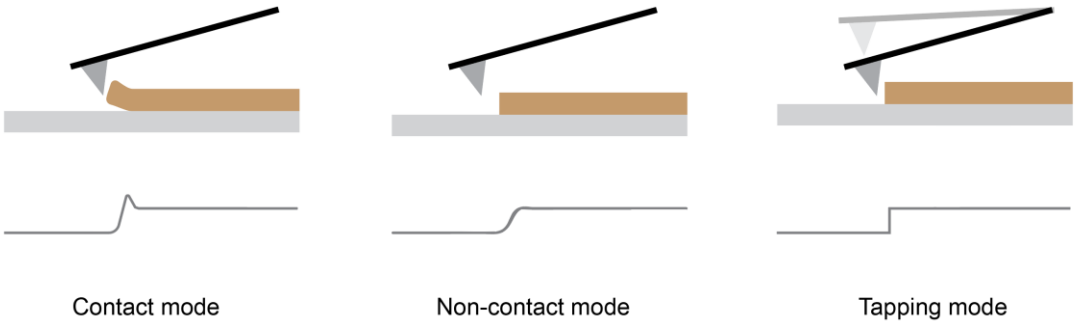

Figure 2-3. *Comparison of AFM working modes (figure was optimized for better illustration from reference 2).*

Beyond surface topography, other characteristics such as electrical and mechanical properties can be acquired simultaneously at the nanoscale. For instance, electrical characteristics such as conductivity can be measured by using a conductive tip. On the other hand, AFM can record the elasticity and the viscosities of samples ranging from inorganic materials to living cells and membranes. Moreover, due to the versatility of such methodology, AFM provides possibilities of nano-manipulation by forcing intended contact. By forcing the tip 'hard' contact with the surface, nanolithography can be achieved. As a result, AFM becomes unique in the sense that it allows the user to modify and manipulate objects while measuring the interaction forces at the nanoscale.

2.2 Spectroscopic methods

2.2.1 Absorption spectroscopy

2.2.1.1 Steady-state absorption spectroscopy

As a physical phenomenon, the absorption of electromagnetic radiation happens when the matter (the absorber) takes up the photon energy from the incident light, which will result in the gradually reduced light intensity as it propagates through the medium. Essentially, photons that match the available energy gaps presented in the matter will be absorbed and the corresponding molecules of the absorber will be excited, while the rest of the photons are transmitted through the absorber. Consequently, important information on the band structures of tested materials can be revealed by their specific absorption spectra, and the technique serves as an efficient tool for determining components and structures of materials.

From an experimental point of view, one needs to pass the light through the sample and to measure the light intensity before (I_{in}) and after (I_{out}) the sample to determine the absorption (as indicated in ***Figure 2-4***). Then, the relevant values of the sample could be calculated as:

$$T = \frac{I_{out}}{I_{in}}$$

$$A = -\log T = \varepsilon c l$$

where T is defined as the transmittance, A the absorbance or optical density (OD). If the density of light absorbing molecules is expressed in molar concentration c, the absorbing characteristic as molar extinction coefficient ε and the optical path as l (as labelled in ***Figure 2-4***), then the absorbance A can be expressed by their product.

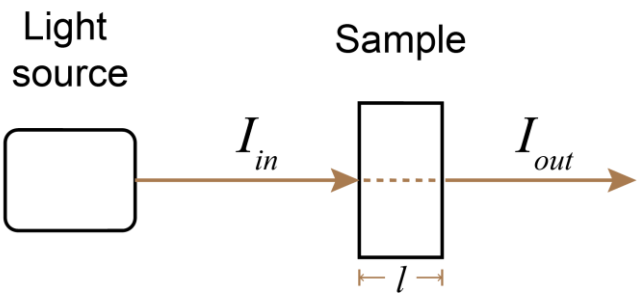

Figure 2-4. *The light absorption process of a sample. The intensities of the incident light* I_{in} *and the light passed the sample* I_{out} *together describe the absorption of this sample.*

Technically speaking, to obtain the absorption spectrum, the measurements must be repeated in the expected wavelength range by tuning the light source from one wavelength to another with small steps (which decides the wavelength resolution). As a result, this underlines three major requirements for the absorption spectroscopy instrument. Firstly, one needs a source providing monochromatic light which can be tuned easily in a wide range. Secondly, a detector is required to measure the intensities, I_{in} and I_{out}. Finally, some optical components are needed to connect different parts together (including the sample).[7] A schematic optical scheme of such device is presented in ***Figure 2-5***.

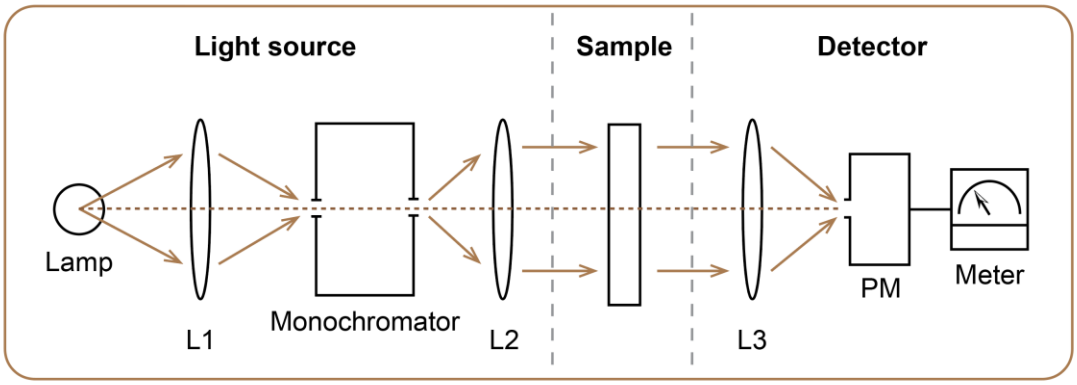

Figure 2-5. *The schematic illustration of the absorption spectroscopy device. Such device is composed of three basic sections: firstly, a source of monochromatic light which can be tuned easily in a wide range; secondly, a detector is required to measure the intensities,* I_{in} *and* I_{out}*; thirdly, some optical components connecting different parts together (as indicated in the figure as L1, L2 and L3).*

As can be seen there is only one photodetector in the scheme. To measure the light intensity before and after the sample the measurements must be done twice: first time without the sample to obtain I_{in} and the second time with the sample to obtain I_{out}. Note that for our first measurement, "without the sample" essentially means the use of a reference sample which considers absorptions of the cuvette, the solvent and attenuation factors such as reflection. In this case, with the two acquired measurements, the absorption of the sample of interest (tested molecules/particles etc.) will be obtained.

The light detection part in the scheme consists of a photomultiplier tube (PM) detector and a meter. The actually detected signal is the PM output voltage U, which is proportional to the light intensity on the PM entrance, $U = s * I$, where s is the voltage

sensitivity of the detector. Therefore, the transmittance T can be obtained from the PM output voltages of the two measurements U_1 and U_2:

$$T = \frac{U_2}{U_1} = \frac{I_{out}}{I_{in}}$$

In a typical experiment, the whole spectrum is first measured without the sample, giving the spectrum $U_1(\lambda)$. Then the spectrum is measured with the sample to yield the spectrum $U_2(\lambda)$. Finally, the transmittance or absorbance is calculated from these two spectra and will be presented to the instrument user directly. The first measured spectrum $U_1(\lambda)$, is commonly known as the baseline and the measurements of the baseline can be acquired once for a series of samples.

2.2.1.2 Transient absorption spectroscopy (TAS)

In order to study the detailed kinetics and mechanisms of physical events occurring on the time scales from nanosecond to femtosecond range, transient absorption spectroscopy (TAS) was developed with the help of ultrafast laser technologies.[8] Depending on the time resolution of the TAS setup, one can investigate non-radiative relaxation of higher electronic states (femtoseconds), vibrational relaxations (picoseconds) and radiative relaxation of excited singlet state (typically on nanoseconds time scale). As a result, TAS has the capability to trace the intermediate states in a photo-chemical reaction; energy or charge transfer process; conformational changes, thermal relaxation, fluorescence processes etc..[8–13] Importantly, compared with time-resolved fluorescence spectroscopy, TAS allows one to investigate the evolution of non-emissive states of the studied system.

In a typical TAS measurement, a fraction of the sample molecules is promoted to an electronically excited state by means of an excitation pulse (the pump). A weak probe pulse (i.e., a pulse that has such a low intensity so that multiphoton/multistep processes are avoided during probing) will be sent through the sample with a time delay τ with respect to the pump pulse. After passing the sample, the probe beam reaches the spectrometer composed of a monochromator and a photon detector where the transient absorption spectra will be recorded as a function of time (***Figure 2-6 a***).

A schematic description of the sample's electronic states during the TAS measurement can be found in ***Figure 2-6 b***. Different events occur among the ground state (G) and excited states (A, B), with the application of a single-wavelength pump laser or the white light probe as a function of time (t). In the absence of photoexcitation, most species are in the ground state (G). When $t < 0$, before the pump laser excitation arrives, the incident probe beam is on the sample and the detector records the intensity of the ground state (G) absorption resulting in the spectrum Abs ($t < 0$). At $t = 0$, the pump pulse reaches the sample and creates a high, non-equilibrium population in the excited state A. After the pump excitation, as $t > 0$, another spectrum Abs ($t > 0$) is obtained. In this spectrum, a decrease in the ground state absorption ($G \rightarrow A$) occurs because more ground state molecules were "pumped up" (promoted) to excited states, which is known as the ground state bleach (depletion). Additionally, a new component due to the excited state absorption ($A \rightarrow B$) is also observed in the spectrum.

Subsequently, by subtracting the absorption spectrum of the sample in the ground state (before pump, t < 0) from the absorption spectrum of the excited sample (after pump, t > 0), a difference absorption spectrum is then generated as (ΔAbs or ΔA):

$$\Delta Abs(t) = Abs(t > 0) - Abs(t < 0)$$

A series of these transient absorption spectra could be acquired by changing the time delay τ between the pump and the probe and recording the corresponding ΔA spectrum at each time delay. Consequently, a ΔA profile as a function of τ and wavelength λ, i.e., a $\Delta A\ (\lambda, \tau)$, reflecting the dynamic processes occurring in the system under study, is obtained.

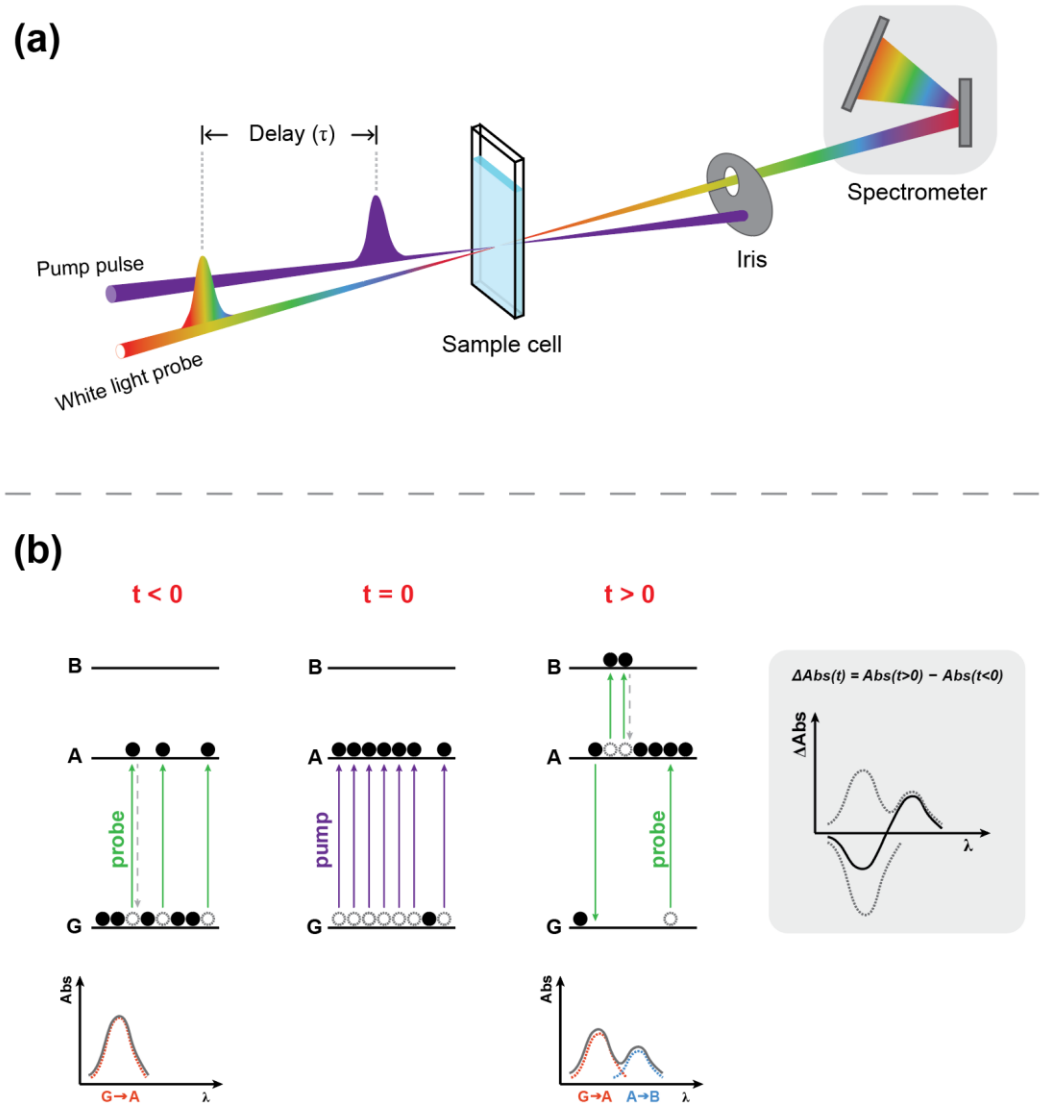

Figure 2-6. *(a) The schematic depiction of the transient absorption spectroscopy setup and (b) a schematic example of how the difference absorption spectrum (ΔA) is generated [figure (b) was optimized based on schematics from Edinburgh Instruments Ltd. for better illustration].*

In general, a ΔA spectrum contains contributions from various processes:[14]

(1) The first contribution is known as the ground state bleach. As a fraction of the molecules has been promoted to the excited state through the action of the pump pulse,

the number of molecules in the ground state is decreased (depleted) (as shown in ***Figure 2-6 b***). Therefore, the ground-state absorption in the excited sample is less than that in the non-excited sample. Consequently, a negative signal in the ΔA spectrum is observed in the region of ground state absorption, as schematically indicated in ***Figure 2-7*** (red dashed line).

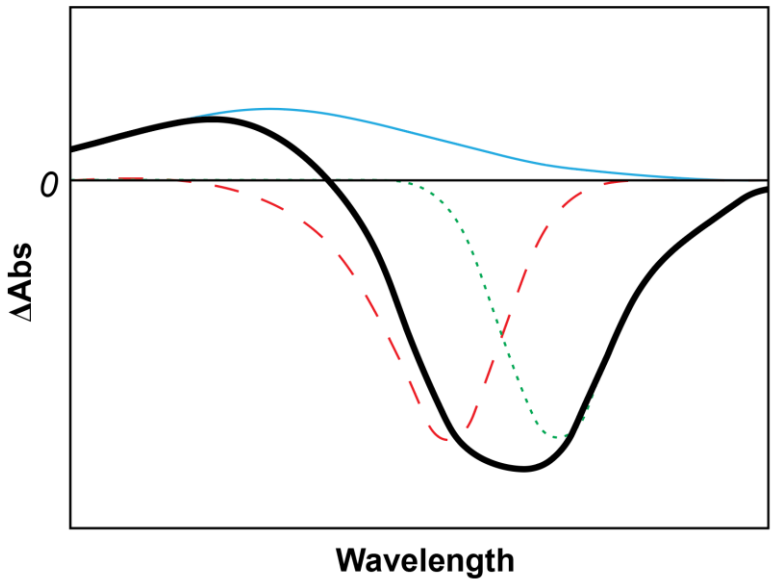

Figure 2-7. *Main contributions to a ΔA spectrum: ground state bleach (red dashed line), stimulated emission (green dotted line), excited-state absorption (blue solid line) and sum of these contributions (thick black solid line) (figure was optimized for better illustration from reference 14).*

(2) The second contribution could be the stimulated emission. For a two-level system, the Einstein coefficients for absorption from the ground to the excited state (A_{12}) and stimulated emission from the excited to the ground state (A_{21}) are identical. Thus, upon population of the excited state, stimulated emission to the ground state will occur when the probe pulse passes through the excited sample. Stimulated emission happens only when transitions are optically allowed and has a spectrum that follows the fluorescence

spectral features of the excited chromophore, i.e., it is usually Stokes shifted with respect to the ground-state bleach. Stimulated emission results in an increase of light intensity on the detector, corresponding to a negative ΔA signal, as schematically indicated in ***Figure 2-7*** (green dotted line).

(3) The third contribution could be the excited-state absorption. Upon excitation with the pump pulse, optically allowed transitions from the excited (populated) states of a chromophore to higher excited states may exist in certain wavelength regions, and absorption of the probe pulse at these wavelengths will occur. Consequently, a positive signal in the ΔA spectrum might be observed in the region of excited-state absorption (***Figure 2-7***, blue solid line). Note that the intensity of the probe pulse is considerably weak throughout the measurement that the excited-state population is not affected substantially by the excited-state absorption process.

(4) Another possible contribution to the ΔA spectrum might come from product absorption. After excitation of the investigated system, reactions may happen which result in a transient or a long-lived molecular state, e.g. triplet states, charge-separated states, and isomerized states. As a result, the absorption of such a (transient) product will appear as a positive signal in the ΔA spectrum. A ground-state bleach will be observed at the wavelengths where the chromophore on which the product state resides has a ground-state absorption.

2.2.2 Fluorescence spectroscopy

After being electronically excited, substances might release the energy via the emission of light that is a process known as luminescence. A fast luminescence process that occurs typically within the nanosecond time scale is fluorescence, which is due to the rapid emission of photons from excited singlet states. As a result, in addition to exploiting controlled fluorescence as the non-destructive way to track/analyse (bio)molecules,[15] the fluorescence spectra of materials can also provide information such as electronic band gap size (HOMO-LUMO gap) of samples.[16] Moreover, together with the growing utilization of Förster resonance energy transfer (FRET, also known as fluorescence resonance energy transfer) to detect biomolecule (e.g. proteins, DNA) interaction/configuration and monitor nanoparticle related assembly/disassembly, molecular fluorescence has become a popular tool in biology and nanoscience.[17–19]

The experimental arrangement of fluorescence measurement equipment is schematically illustrated in ***Figure 2-8***. The fluorometer (steady-state fluorescence measurement system) is composed, in the order of processes, by a source of excitation that can be a lamp with the monochromator (e.g. Xenon flash lamp) or laser(s) (e.g. Nd:YAG laser), a sample stage and an adjustable single wavelength detector (similar to the detector in absorption measurement, consisting of a monochromator, and photomultiplier and a meter). Other components may be needed to connect the parts together and optimize the measurement quality (e.g. filters are applied in the light source and detector section as labelled by F1 and F2 in ***Figure 2-8***). After the incident light has been generated with the desired wavelength, the radiation is collected and focused on the sample. Subsequently, the material is excited by the striking of incident light, and the fluorescence signal is collected by another lens in the direction which is

perpendicular to that of the incident light (to minimize the stray light interference), towards the monochromator input. The final output will be the read from the meter of the detector.

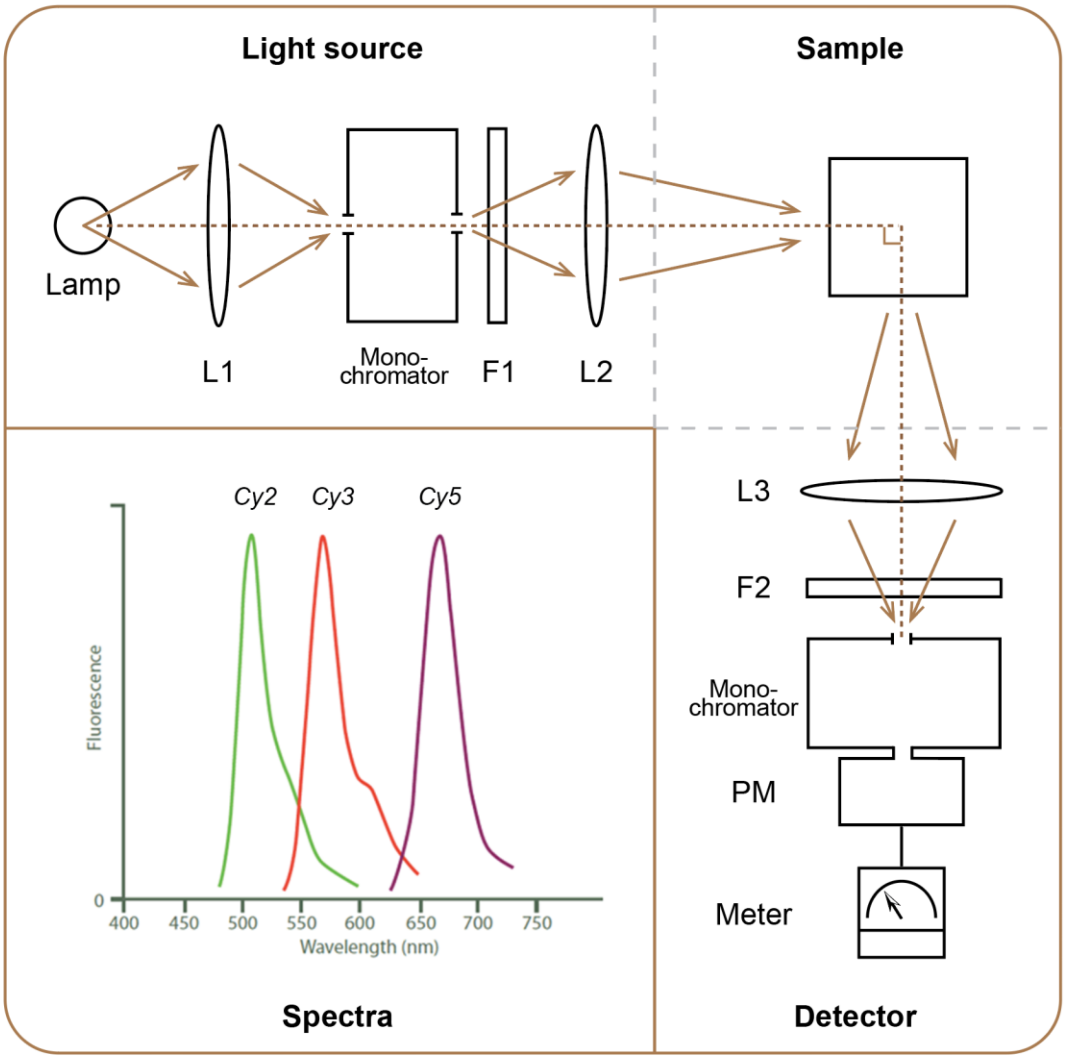

Figure 2-8. *(Top and right) schematic illustration of a steady-state fluorescence measurement setup, and (bottom left) the emission spectra of three commonly used cyanine chromophores (Cy2, Cy3, Cy5) (emission spectra credit: Stratech, Inc).*

Fluorescence spectral data are generally presented as emission spectra, where the fluorescence emission intensity is plotted versus wavelength. Emission spectra vary

widely and are dependent upon the chemical structure of the fluorophore and the solvent in which it is dissolved. As an example, ***Figure 2-8*** shows the emission spectra of Cy2 (cyanine), Cy3 (indocarbocyanine) and Cy5 (indodicarbocyanine), with corresponding fluorescence peaks at 510 nm, 570 nm and 670 nm, respectively.

2.3 Electrophoresis

2.3.1 Gel electrophoresis (GE)

Since its discovery in 1807 by Peter Ivanovich Strakhov and Ferdinand Frederic Reuss, electrophoresis has evolved into an extensively used laboratory technique to separate charged macromolecules by their size or binding affinity.[20] The underlined principle of electrophoresis is that charged molecules move at different rates under the same uniform applied electric field based on their sizes. Molecules (e.g. DNA, proteins etc.) are frequently associated with positive or negative charges when dispersed in aqueous solutions. With the presence of an electric field, these charged molecules will move towards the electrode of opposite charge because of the electrostatic interaction. The whole process happens in a porous matrix made of agarose or polyacrylamide gel. A typical gel electrophoresis setup is illustrated in ***Figure 2-9***. The agarose gel block sits within a tank of buffer that provides the stable electrolyte environment for the running of the gel. The samples are then placed in wells at one end of the gel block and an electrical current will pass across the gel upon the application of the electric field. If the sample molecules are negatively charged in buffer solution (e.g. DNA), they will move toward the positive electrode.

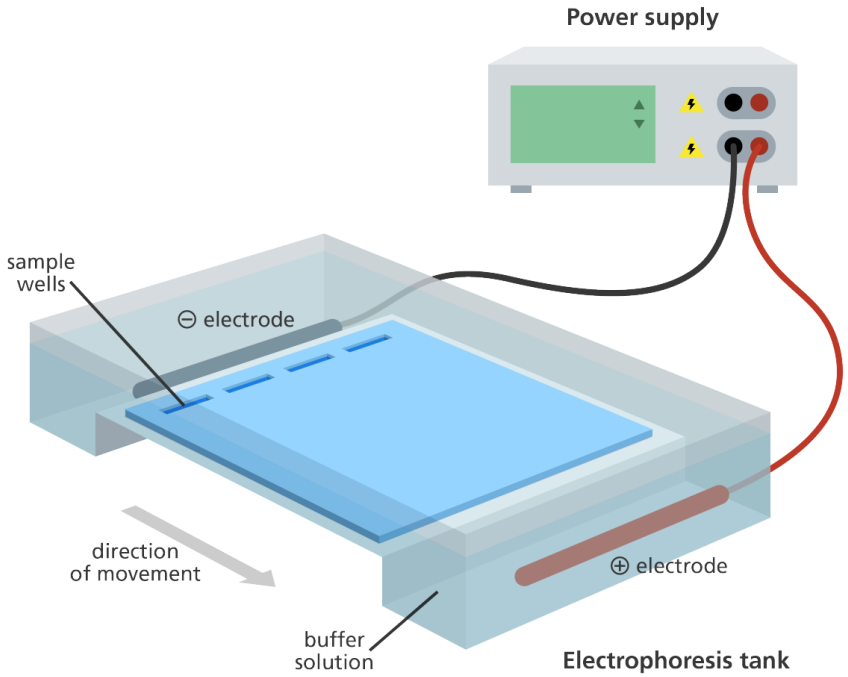

Figure 2-9. *Schematic illustration of a typical agarose gel setup (image credit: Genome Research Limited).*

Several factors are concerned with the relative mobility of the individual molecules. The most important include the net charge, charge/mass ratio, shape, and size of the molecules; the temperature, porosity and viscosity of the matrix through which the molecule migrates.

If a mixture of electrically charged molecules is placed in an electric field of field strength E, they will freely move towards the electrode of opposite charge. However, different molecules will move at quite different and individual rates depending on the physical characteristics of the molecule and on experimental system used. The velocity of movement, v, of a charged molecule in an electric field E depends on variables described by:

$$v = \frac{Eq}{f}$$

where f is the frictional coefficient and q is the net charge of the molecule.[21] The frictional coefficient describes the frictional resistance to molecule mobility and consequently a number of factors such as mass of the molecule, its degree of compactness, buffer viscosity and the porosity of the matrix in which the experiment is performed will all contribute to the final separation quality. The net charge is determined by the number of positive and negative charges in the molecule. For instance, DNA has a particularly uniform charge distribution since a phosphate group confers a single negative charge per nucleotide, resulting in a highly predictable net charge value according to its sequence length. The above equation means that, with similar size, molecules will move faster as their net charge q increases, the electric field E strengthens and as f decreases. Molecules of similar net charge separate due to differences in frictional coefficient while molecules of similar mass/shape may differ widely from each other in net charge. Consequently, it is possible to achieve high resolution separation by gel electrophoresis.

2.3.2 Dielectrophoresis (DEP)

Different from conventional electrophoresis where a uniform electric field is applied for charged molecules, dielectrophoresis (DEP) causes the motion of neutral particles by the application of a non-uniform electric field. On the basis of the study by Herbert Pohl in the 1950s,[22,23] DEP has emerged as an important technique for the manipulation of micro- and nano-sized particles in recent years.[24–26]

Dielectrophoresis occurs when a polarizable particle is suspended in a non-uniform electric field. The particles will be polarized in the presence of electric field and the poles will experience forces in opposite directions. The total force applied on the particles should be zero in a uniform electric field. However, when the field is non-uniform, the dipole will experience a total force, causing the movement of the particles (***Figure 2-10***). The relative polarizability of the particle and medium decides the orientation of the dipole. As a result, the direction of the force is dependent on field gradient rather than field direction, and DEP will occur in AC as well as DC electric fields; polarization (and hence the direction of the force) will depend on the relative polarizabilities of particle and medium.

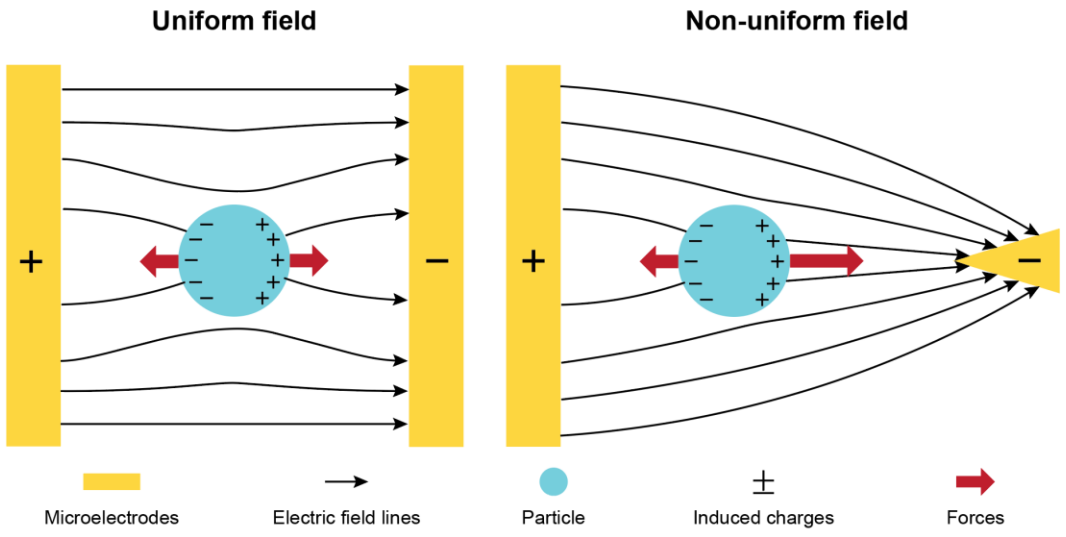

Figure 2-10. *The polarized particle in a uniform electric field (left) and a non-uniform electric field (right) (figure was optimized for better illustration from reference 26).*

The expression for the time-average DEP force (acting on a spherical particle) is given by:

$$F_{DEP} = 2\pi R^3 \varepsilon_m Re[CM(\omega)]\nabla E^2$$

with

$$CM(\omega) = \left(\frac{\varepsilon_p^* - \varepsilon_m^*}{\varepsilon_p^* + 2\varepsilon_m^*}\right)$$

where R is the particle radius, ε_m is the permittivity of the suspending medium, ∇ represents the gradient operator, E is the electric field amplitude (rms), $Re[CM(\omega)]$ is the real part of the Clausius-Mossotti factor (CM) that is related to the effective polarizability of the particle. Note that ε_m^* and ε_p^* are the complex permittivity of the medium and particle respectively, which could be expressed as:

$$\varepsilon^* = \varepsilon - \frac{j\sigma}{\omega}$$

with σ as the conductivity, ε the permittivity and ω the angular frequency of the applied electric field.

The frequency-dependence of $Re[CM(\omega)]$ indicates that the force acting on the particle varies with the frequency. The magnitude of $Re[CM(\omega)]$ also varies depending on whether the particle is more or less polarizable than the medium. If $Re[CM(\omega)]$ is positive, then particles move to regions of highest field strength (positive DEP); the converse is negative DEP where particles are repelled from these regions. Hence, not only the manipulation (movement) of particles is possible but also the separation of mixed samples with varied permittivity can be achieved. By careful construction of the electrode geometry which creates the electric field, it is possible to create electric field morphologies so that potential energy minima are bounded by regions of increasing electric field strengths. In such electrodes, particles experiencing positive DEP are attracted to the regions of highest electric field (typically the electrode edges, particularly where adjacent electrodes are close), whilst particles experiencing negative DEP are trapped in isolated field minima. As the relative polarizabilities of the particle

and medium are frequency-dependent, varying the energizing signal and measuring the way in which the force changes can be used to determine the electrical properties of particles as well.

Notably, in addition to applying DEP for the manipulation of nanoparticles such as gold nanoparticles,[27] the manipulation and separation of CNTs were also realized by customizing the related DEP parameters (e.g. electrode shape and configuration, electric field frequency and strength, suspending medium etc.).[28–30] For instance, in 2003 researchers have developed a method to separate metallic SWCNTs from semiconducting ones using AC DEP,[28] based on the different relative dielectric constants of the two species with respect to that of the solvent (***Figure 2-11***).

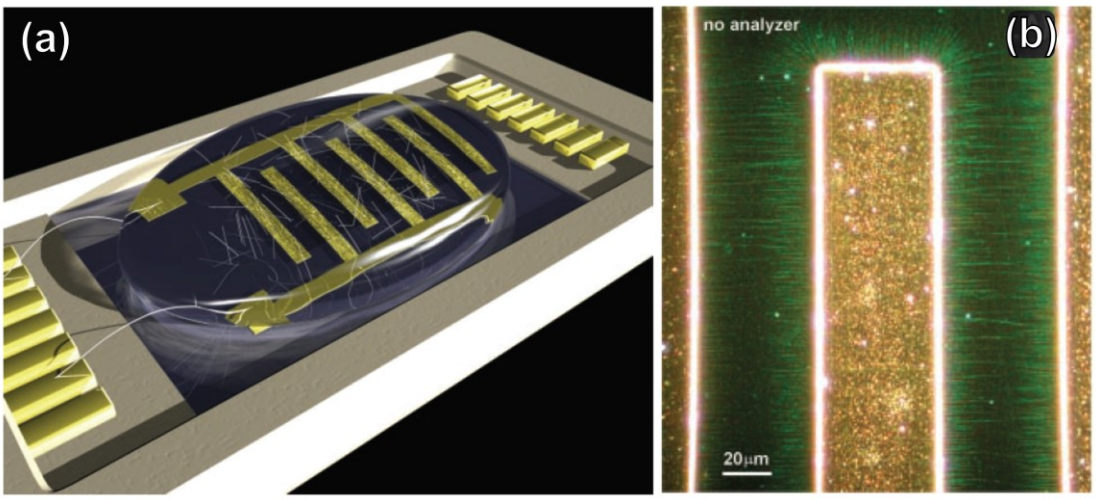

Figure 2-11. *The application of DEP for the manipulation and separation of CNTs. (a) Illustration of the experimental DEP setup for the manipulation of CNTs. (b) The Rayleigh scattered light from the DEP deposited CNTs suggests the fine alignment obtained.*[28]

2.4 References

1. Binnig, G., Quate, C. F. & Gerber, C. Atomic force microscope. *Phys. Rev. Lett.* **56**, 930–933 (1986).

2. Jalili, N. & Laxminarayana, K. A review of atomic force microscopy imaging systems: Application to molecular metrology and biological sciences. *Mechatronics* **14**, 907–945 (2004).

3. Vinckier, A. & Semenza, G. Measuring elasticity of biological materials by atomic force microscopy. in *FEBS Letters* **430**, 12–16 (1998).

4. Dufrêne, Y. F. *et al.* Imaging modes of atomic force microscopy for application in molecular and cell biology. *Nature Nanotechnology* **12**, 295–307 (2017).

5. Markiewicz, P. & Goh, M. C. Atomic Force Microscopy Probe Tip Visualization and Improvement of Images Using a Simple Deconvolution Procedure. *Langmuir* **10**, 5–7 (1994).

6. Mironov, V. L. *Fundamentals of Scanning Probe Microscopy*. *the Russian Academy of Sciences Institute of Physics of Microstructures* (2004).

7. Tkachenko, N. V. Optical spectroscopy: methods and instrumentations. *Opt. Spectrosc. Methods Instrumentations* 15–38 (2006).

8. Kimura, Y., Alfano, J. C., Walhout, P. K. & Barbara, P. F. Ultrafast transient absorption spectroscopy of the solvated electron in water. *J. Phys. Chem.* **98**, 3450–3458 (1994).

9. Tamaki, Y. *et al.* Dynamics of efficient electron-hole separation in TiO2 nanoparticles revealed by femtosecond transient absorption spectroscopy under the weak-excitation condition. *Phys. Chem. Chem. Phys.* **9**, 1453–1460 (2007).

10. Kovalenko, S. A., Schanz, R., Hennig, H. & Ernsting, N. P. Cooling dynamics of an optically excited molecular probe in solution from femtosecond broadband transient

absorption spectroscopy. *J. Chem. Phys.* **115**, 3256–3273 (2001).

11. McArthur, E. A., Morris-Cohen, A. J., Knowles, K. E. & Weiss, E. A. Charge carrier resolved relaxation of the first excitonic state in CdSe quantum dots probed with near-infrared transient absorption spectroscopy. *J. Phys. Chem. B* **114**, 14514–14520 (2010).

12. Nogueira, A. F. *et al.* Charge recombination in conjugated polymer/fullerene blended films studied by transient absorption spectroscopy. *J. Phys. Chem. B* **107**, 1567–1573 (2003).

13. Logunov, S. L., Ahmadi, T. S., El-Sayed, M. A., Khoury, J. T. & Whetten, R. L. Electron dynamics of passivated gold nanocrystals probed by subpicosecond transient absorption spectroscopy. *J. Phys. Chem. B* **101**, 3713–3719 (1997).

14. Berera, R., van Grondelle, R. & Kennis, J. T. M. Ultrafast transient absorption spectroscopy: Principles and application to photosynthetic systems. *Photosynthesis Research* **101**, 105–118 (2009).

15. Progatzky, F., Dallman, M. J. & Celso, C. Lo. From seeing to believing: Labelling strategies for in vivo cell-tracking experiments. *Interface Focus* **3**, (2013).

16. O'Connell, M. J. *et al.* Band gap fluorescence from individual single-walled carbon nanotubes. *Science (80-.).* **297**, 593–596 (2002).

17. Qi, X.-J., Lu, C.-H., Cecconello, A., Yang, H.-H. & Willner, I. A two-ring interlocked DNA catenane rotor undergoing switchable transitions across three states. *Chem. Commun. (Camb).* **50**, 4717–20 (2014).

18. Lu, C. H., Cecconello, A., Elbaz, J., Credi, A. & Willner, I. A three-station DNA catenane rotary motor with controlled directionality. *Nano Lett.* **13**, 2303–2308 (2013).

19. Amoroso, G. *et al.* DNA-Powered Stimuli-Responsive Single-Walled Carbon Nanotube Junctions. *Chem. Mater.* **31**, 1537–1542 (2019).

20. Stellwagen, N. C. Electrophoresis of DNA in agarose gels, polyacrylamide gels and in free solution. *Electrophoresis* **30**, (2009).

21. Adamson, N. J. & Reynolds, E. C. Rules relating electrophoretic mobility, charge and molecular size of peptides and proteins. *J. Chromatogr. B Biomed. Appl.* **699**, 133–147 (1997).

22. Pohl, H. A. The motion and precipitation of suspensoids in divergent electric fields. *J. Appl. Phys.* **22**, 869–871 (1951).

23. Pohl, H. A. Some effects of nonuniform fields on dielectrics. *J. Appl. Phys.* **29**, 1182–1188 (1958).

24. Morgan, H. & Green, N. G. *AC electrokinetics: colloids and nanoparticles*. *Microtechnologies and Microsystems Series* **2**, (2002).

25. Tathireddy, P., Choi, Y. H. & Skliar, M. Particle AC electrokinetics in planar interdigitated microelectrode geometry. *J. Electrostat.* **66**, 609–619 (2008).

26. Khoshmanesh, K., Nahavandi, S., Baratchi, S., Mitchell, A. & Kalantar-zadeh, K. Dielectrophoretic platforms for bio-microfluidic systems. *Biosensors and Bioelectronics* **26**, 1800–1814 (2011).

27. Kumar, S., Yoon, S. H. & Kim, G. H. Bridging the nanogap electrodes with gold nanoparticles using dielectrophoresis technique. *Curr. Appl. Phys.* **9**, 101–103 (2009).

28. Krupke, R., Hennrich, F., Löhneysen, H. v. & Kappes, M. M. Separation of metallic from semiconducting single-walled carbon nanotubes. *Science (80-.).* **301**, 344–347 (2003).

29. Krupke, R., Hennrich, F., Kappes, M. M. & Löhneysen, H. V. Surface conductance induced dielectrophoresis of semiconducting single-walled carbon nanotubes. *Nano Lett.* **4**, 1395–1399 (2004).

30. Krupke, R., Linden, S., Rapp, M. & Hennrich, F. Thin films of metallic carbon nanotubes prepared by dielectrophoresis. *Adv. Mater.* **18**, 1468–1470 (2006).

Chapter 3

Constructing Multiplexed Photo-Responsive Nano-Devices: The Dual Role of DNA-Wrapped SWCNT

3.1 Introduction

By synergistically combining the individual properties of more than one nanoscale component, novel features of hybrid structure assemblies represent a key motivation for making future functional nanomaterials.[1–7] Among the potential applications of these hybrid structures, photodetection is a typical example where the nanodevice converts incident photons into an electrical signal. Devices based on these novel hybrids will pave the way towards next-generation photodetectors with not only improved performance but also merits including nanoscale dimensions and potential flexibility.[8–18]

For a photodetection device based on hybrid structures, efficient electron-hole pair separation and charge carrier transport are essential.[19] Among the hybrid structures for

optoelectronic applications, CNT based hybrids are of particular interest because the presence of CNTs greatly improves the charge mobility and facilitates the charge transfer at the heterointerface with other active components in the hybrids, so that the device efficiency can be promoted: these advantageous features are granted by the high surface area, outstanding electrical and electronic properties of CNTs.[20,21] Consequently, CNTs can serve as promising building blocks for the construction of nanoarchitectures of next generation optoelectronic devices for such applications.[1,22–26] Meanwhile, inorganic semiconducting quantum dots (QDs) are very appealing components to be assembled with CNTs since they hold a broad absorption band and high tunability of band gap according to their sizes and compositions.[17,27–29]

As a result, researchers have been trying to fabricate devices based on hybrids from CNTs and QDs for next generation optoelectronic applications. In this regard, CdS and CdSe have been widely employed to fabricate systems exhibiting photoresponses to green/blue light in the visible spectrum.[27,30–32] Istvan et al. synthesized CdS-SWCNT hyrbids in THF and methanol, and investigated the electron transfer from CdS to SWCNT by transient absorption spectroscopy (TAS).[30] A similar electron transfer process was proposed for CdSe-CNT heterostructures in a study carried out by Liangbing Hu et al., where hybrids were assembled on surface from DMF solutions employing CdSe QDs pre-functionalized with a pyrene derivative.[31] Moreover, researchers revealed that amine molecules were able to mediate the doping of SWCNTs, giving them the capability to tune the photoresponse of fabricated CdS-CNT hybrid devices.[32] Similarly, PbS was employed, allowing for the extension of the photoresponse into the red and near infrared (NIR) regime.[28,33–37] Defa Wang et al. fabricated photovoltaic devices based on PbS-CNT hybrids made from oleyamine

capped PbS QDs and pre-functionalized MWCNTs.[34] Fast photoresponse was further obtained in PbS-CNT based devices fabricated with pulsed laser ablation techniques.[35] Additionally, multiple exciton generation (MEG) was observed in PbS-CNT hybrids highlighting their potential for high performance optoelectronic applications.[36]

Given the demonstrated photoresponses of these hybrids, challenges remain as the hybrid synthesis and device fabrication approaches still unavoidably involve at least some of the following aspects: i) the use of organic solvents during in the hybrid assembly process due to the extreme hydrophobicity of CNTs; ii) the chemical functionalization of CNT surfaces, potentially compromising the nanotubes' electronic properties; iii) the use ligands around the QDs to prevent their aggregation, to the detriment of an efficient charge transfer between the QDs and the CNTs; iv) the fabricated devices are typically made of unaligned/disordered composite (e.g. spin coated films), which hinders their further controlled miniaturization down to the nanoscale; v) only one type of hybrid is implemented in the device so that the potential of multiplexed wavelength responses in a single nanodevice is not exploited.

On the other hand, assembly approaches by exploiting some specific template for the construction of nanohybrids have gained more attention in recent years, as they often represent facile and effective bottom-up strategy operating in solutions. For instance, DNA was demonstrated to be the template for the growth of metal nanoparticles (NPs) or efficient assembly of heterostructures with inorganic nanoparticles and hybrid nanowires with semiconducting materials.[38–42] Moreover, some pre-functionalized CNTs were also proved to template hybrid structures with NPs.[31,43] Importantly, DNA-

wrapped CNTs (DNA-CNTs), with the ideal combination of desired CNT features (preserved electronic properties, one-dimensionality) and great water dispersity,[44] could be the promising templating candidate to construct CNT based semiconducting nanohybrid structures in aqueous solutions and this possibility has yet to be explored.

Herein, by employing DNA-CNTs as the well-dispersed one-dimensional templates,[44] we present a facile strategy to assemble in aqueous solution different QD-CNT heterostructures, organize them (DNA-CNTs and the templated QD-CNT hybrids) in nanoscale devices, and exploit their photoinduced electrical response at different wavelengths for the construction of multiplexed chips. We developed the same one-pot assembly method to grow CdS or PbS QDs along the sidewall of the nanotube templates, directly in aqueous solution. The morphology of DNA-CNT template and the assembly of CdS-DNA-CNT/PbS-DNA-CNT hybrid nanostructures was confirmed by atomic force microscopy (AFM), while their organization between pre-patterned nanoelectrodes was achieved via dielectrophoresis (DEP). This approach allowed us to fabricate multiplexed nanoscale devices, that we tested for their photoresponse to blue (405 nm), green (532 nm) and red (650 nm) light on probe station.

Intriguingly, the photoinduced electrical response features indicated different processes within the devices, depending on: i) whether the template surface is decorated by inorganics and ii) the exact inorganic material employed, i.e. CdS or PbS. By comparing the devices' photo-responsive performances in ambient conditions (in air) and in vacuum, a photo-induced molecular desorption process was suggested for the DNA-CNT and CdS-DNA-CNT devices. Meanwhile, further investigations on the excited-

state behaviour of the hybrids via TAS indicated the charge transfer between excited SWCNT and PbS QDs within the PbS-DNA-CNT heterostructures. Significantly, the two mechanisms in our devices revealed two roles of DNA-CNTs which both conceive valuable potential for future applications: as the photo-responsive device itself and as the effective template to construct CNT based photo-responsive hybrids. The strategy we developed is of general applicability for the controlled fabrication of CNT-based multiplexed photo-responsive optoelectronic hybrid systems and devices.

3.2 Hybrid assembly

We first wrapped and dispersed (7,6) chirality enriched semiconducting SWCNTs with single-strand DNA (ssDNA) through sonication in aqueous solution (see scheme in ***Figure 3-1a***).[44] In brief, (7,6) enriched SWCNTs were wrapped by single-strand (ss) DNA [$(GT)_{20}$] in 0.1M NaCl solution under 60 min sonication to form the DNA-CNTs. The undispersed CNTs and residues (amorphous carbon etc.) were removed by keeping only the supernatant after 90 min centrifugation at 16000 g. The supernatant solution was then dialysed against MiliQ® H_2O overnight. The DNA-CNT aqueous solution can then be stored under 4°C as stock solution for further device implementation.

To assemble PbS-DNA-CNT hybrids, the prepared aqueous solutions containing DNA-CNT templates were subject to a facile one-pot two-step procedure: i) addition of Pb^{2+} into the DNA-CNT solution and overnight incubation; ii) addition of S^{2-} to the solution and overnight incubation (as shown in ***Figure 3-1a***). In detail, the stock DNA-CNT solutions were diluted 10x with MiliQ® H_2O. To every 10 μL of diluted DNA-CNT

solution, 25 μL of H_2O and 10 μL of 5 mM Pb^{2+} [dissolved from $Pb(NO_3)_2$] were added and the solution was incubated at 4°C overnight; to the incubated solution was then added 10 μL of 5 mM S^{2-} (dissolved from Na_2S) and subject to overnight incubation. The incubated solution was dialysed against MiliQ® H_2O for 3 h. The incubated solutions were dialyzed against MiliQ® H_2O for 3 h and the PbS-DNA-CNT hybrids were then ready for device implementation and further investigations.

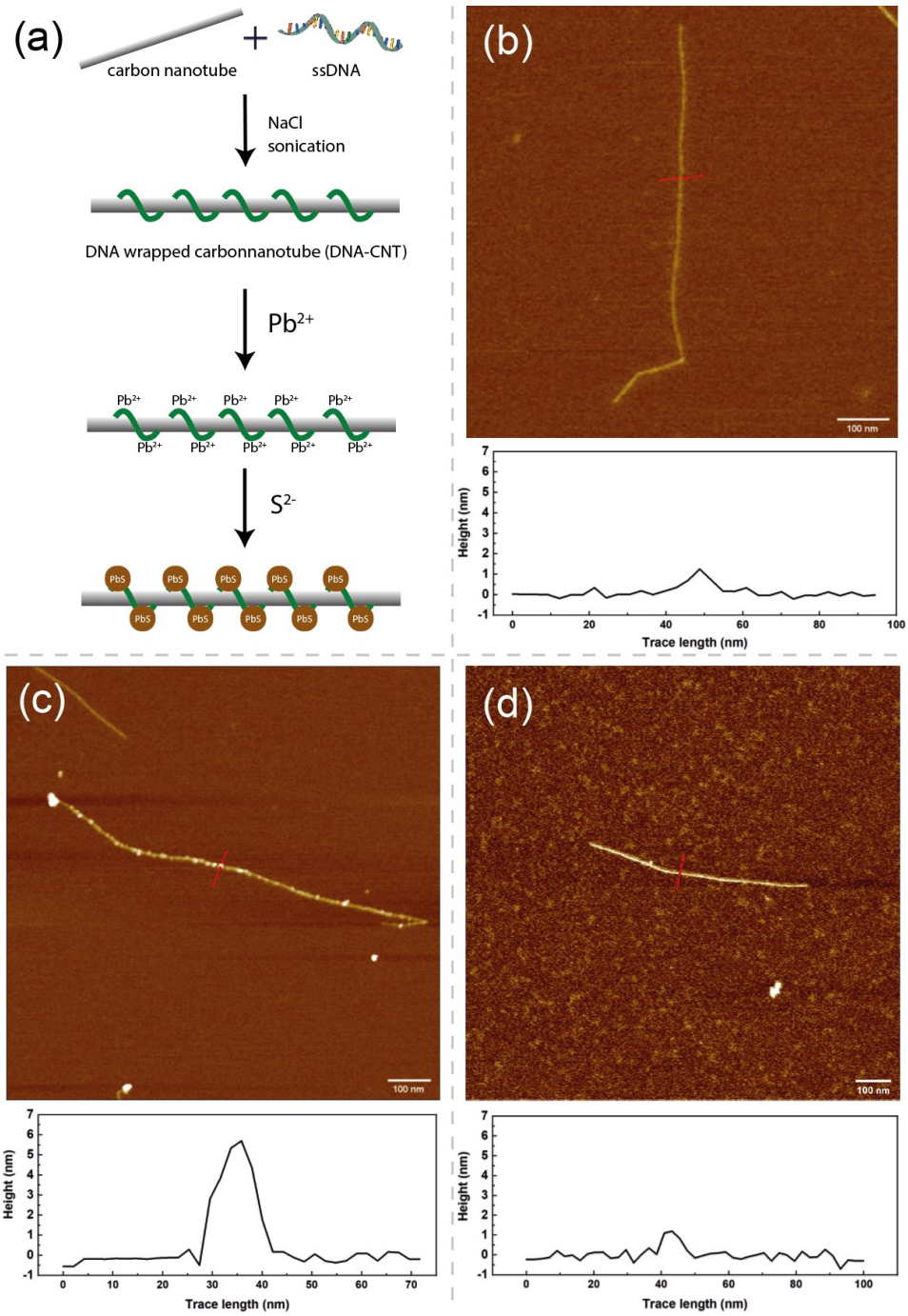

Figure 3-1. *Assembly scheme and AFM characterization. (a) schematic illustration of DNA-CNT preparation and PbS-DNA-CNT hybrid assembly from DNA-CNT templates in aqueous solution; (b-d) AFM characterizations of the (b) DNA-CNT, (c) PbS-DNA-CNT hybrid and (d) DNA-CNT mixed directly with preformed PbS QDs. The height profiles follow the corresponding red dashed lines in every AFM picture above it, indicating the typical sizes of the samples.*

Prepared solutions were cast on muscovite mica to investigate their morphological properties at the nanoscale via atomic force microscopy (AFM); this was done on both the original DNA-CNTs and the templated assembly of PbS-DNA-CNT hybrids: see ***Figure 3-1 b*** and ***Figure 3-1 c*** for representative AFM images. The DNA-CNT has a typical diameter of c.a. 1.4 nm (***Figure 3-1b***), while in the assembled PbS-DNA-CNT hybrid QDs can be observed along the sidewall of the DNA-CNT templates exhibiting a typical size of (4 ± 1) nm (***Figure 3-1c***). Moreover, the AFM height profiles following the lengths of DNA-CNT and PbS-DNA-CNT also indicated the attachment of PbS along the DNA-CNT templates (***Figure 3-2*** and ***Figure 3-3***).

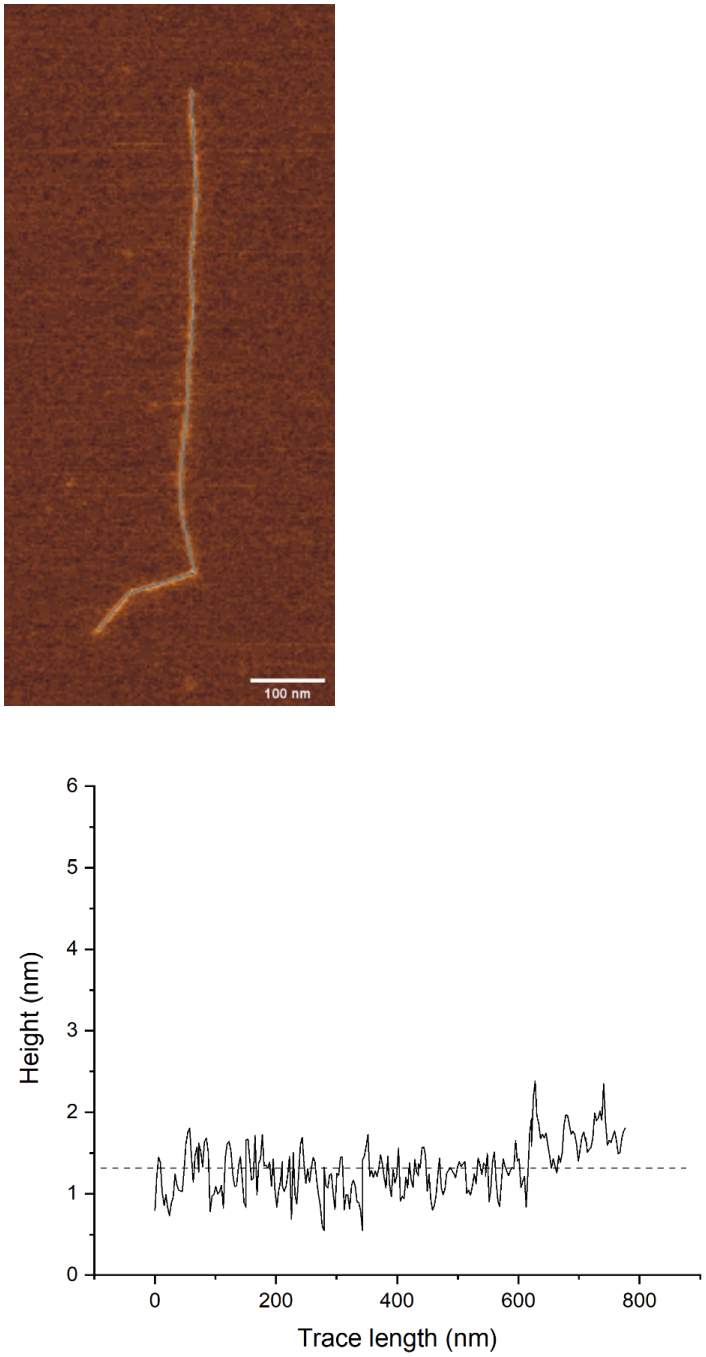

Figure 3-2. *Height profile along the length of DNA-CNT. Top: AFM image of DNA-CNT; bottom: height profile along the length of the shown DNA-CNT (the dashed line indicates the average height of 1.4 nm).*

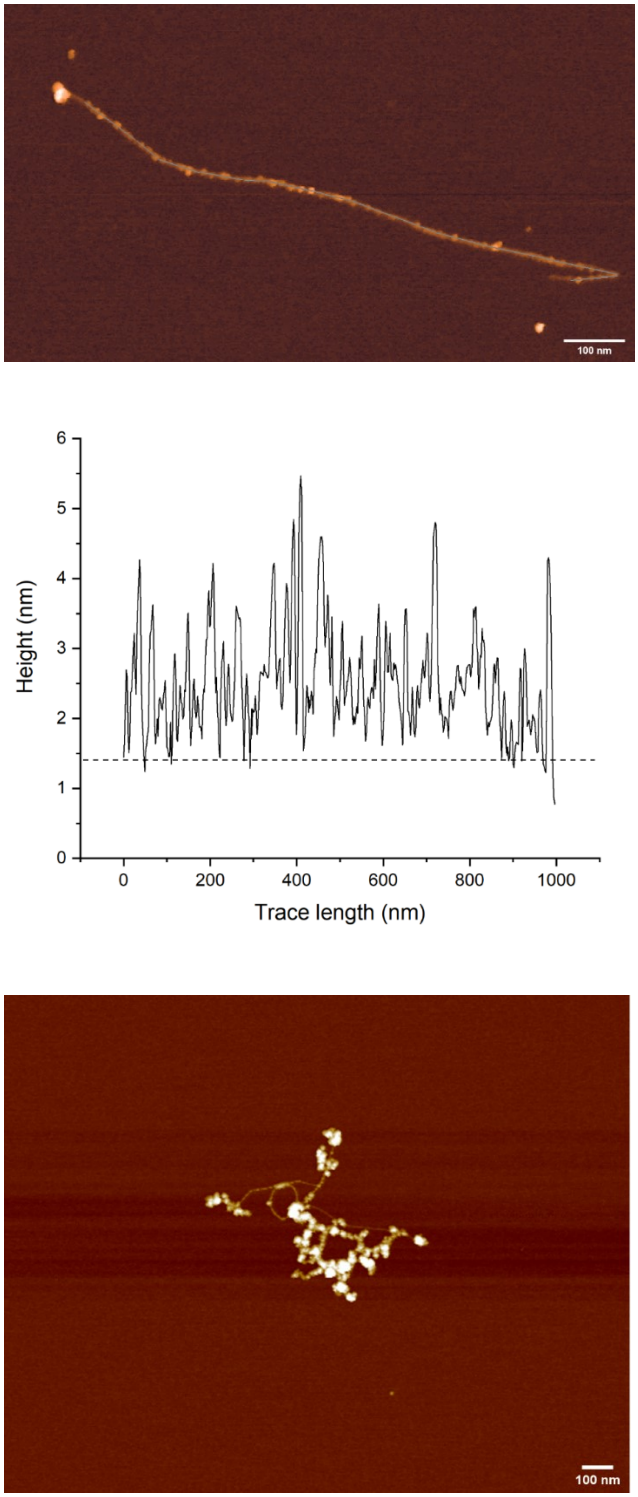

Figure 3-3. *Height profile along the length of PbS-DNA-CNT. Top: AFM image of PbS-DNA-CNT hybrid; middle: height profile along the length of the shown PbS-DNA-CNT (the dashed line indicates the DNA-CNT average height of 1.4 nm); bottom: additional AFM image showing the successful assembly of PbS QDs along DNA-CNTs.*

The AFM data strongly suggests that the direct assembly of PbS QDs along the DNA-CNT templates was successfully achieved in aqueous solution; it is reasonable to assume this to be the result of efficient seeding of Pb^{2+} along the templates via Coulomb interaction between the metal cations and the negatively charged DNA phosphate backbone in H_2O, similar to what was observed on λ-DNA.[39] This templating effect was further confirmed with the AFM images of DNA-CNT templates mixing directly with preformed PbS QDs (i.e. Pb^{2+} and S^{2-} were sequentially added into pure H_2O instead of the solution containing DNA-CNTs, and afterwards pristine DNA-CNTs were then added into the solution of preformed PbS QDs). In this case, before having the chance to interact with negatively charged DNA-CNTs, the metal cations in solution were depleted by reacting with S^{2-} to form PbS. Consequently, as shown in ***Figure 3-1d***, the DNA-CNT from this sample exhibited a diameter of typical pristine DNA-CNT template (c.a. 1.2 nm) and the sidewall were not decorated by QDs (see ***Figure 3-4*** for profile along the length of the sample).

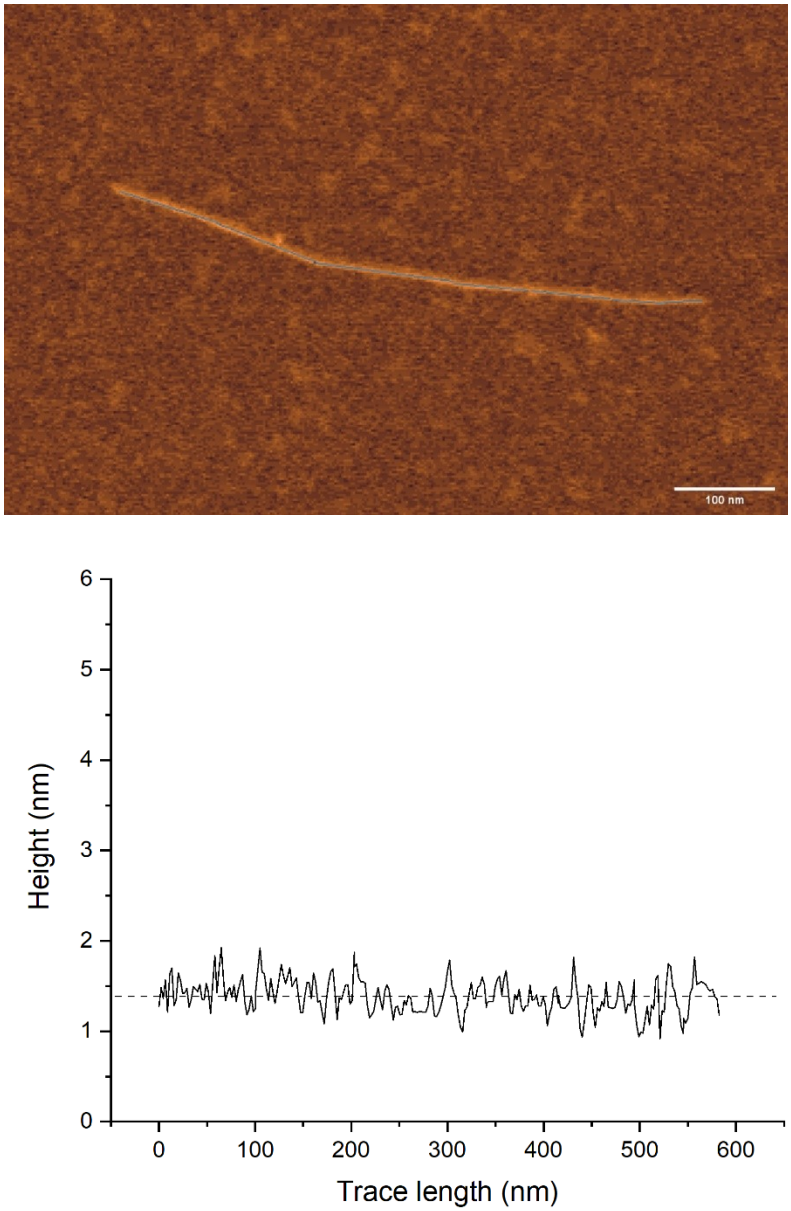

Figure 3-4. *Height profile along the length of DNA-CNT mixed directly with preformed PbS QDs. Top: AFM image of DNA-CNT; bottom: height profile along the length of the shown DNA-CNT (the dashed line indicates the average height of 1.4 nm).*

3.3 Device implementation and performance features

3.3.1 Device implementation

In order to organize the DNA-CNTs and Pb-DNA-CNT heterostructures in device configurations, we cast the solutions on pre-patterned nanoelectrodes and immobilized the hybrids between these electrodes with a dielectrophoretic technique similar to what we have previously demonstrated with aptamer-CNT hybrids and metal-filled CNT hybrids.[45,46] In the AFM images representing the typical device configurations (***Figure 3-5***), small bundles of the aligned DNA-CNTs and PbS-DNA-CNT hybrids can be observed which are estimated to be consist of no more than 353 DNA-CNTs and 322 PbS-DNA-CNT hybrids.

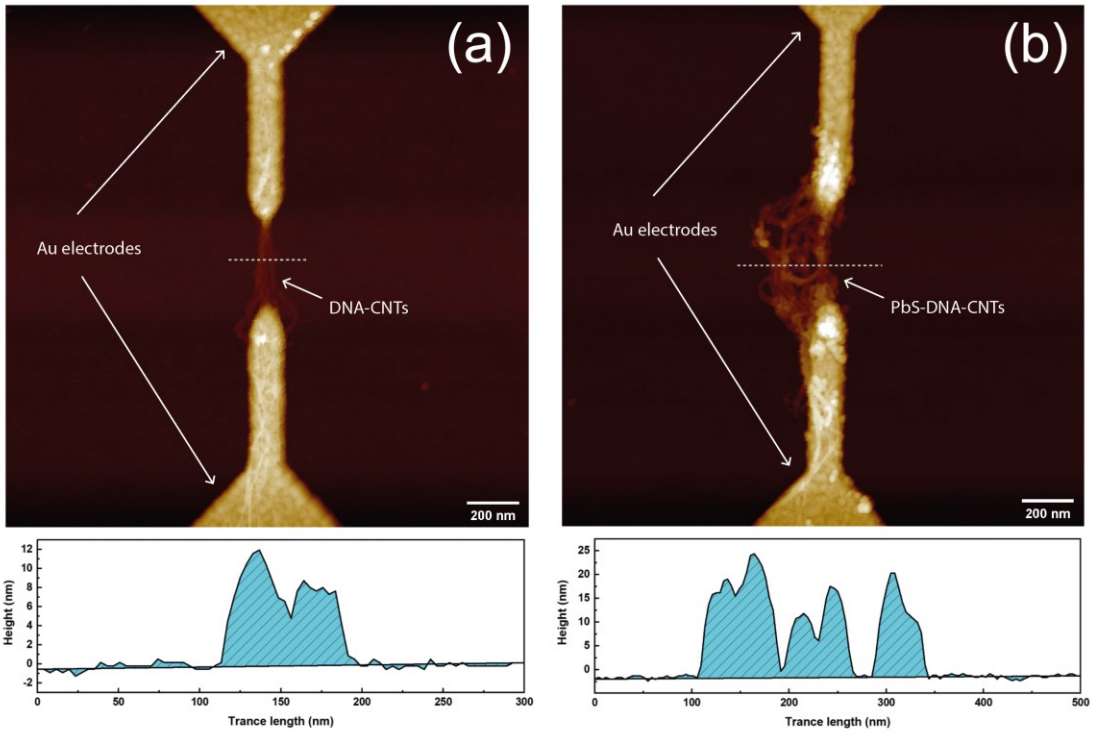

Figure 3-5. *On the same chip, DNA-CNTs and assembled PbS-DNA-CNT hybrids were sequentially aligned between pre-patterned nanoelectrodes (400 nm gap) via dielectrophoresis (DEP) in less than 30s. The AFM images with height profiles along the corresponding dashed lines of typical (a) DNA-CNT device and (b) PbS-DNA-CNT device are shown here. The chip was connected to an electrical measurement setup and the real-time device performance could then be monitored with laser source turned on and off.*

The estimation of the DNA-CNT or PbS-DNA-CNT hybrids quantities between nanoelectrodes is based on the AFM profile data of the devices (***Figure 3-5***). The representative height profiles of the DNA-CNT/PbS-DNA-CNT bundles between the electrodes are shown below the AFM images. The area integration of the bundle profile was calculated to be 544 nm^2 for DNA-CNT device and 2292 nm^2 for PbS-DNA-CNT device (indicated as shadowed areas under the height profiles in ***Figure 3-5 a, b***).

Considering the rigidity of DNA-CNTs and PbS-DNA-CNTs with the average diameters of 1.4 nm and 3 nm respectively (radius of 0.7 nm and 1.5 nm, respectively), it is reasonable to assume every DNA-CNT or PbS-DNA-CNT hybrid has an effective cross section area of at least $A_{DNA\text{-}CNT} = \pi*(0.7)^2 \approx 1.54$ nm^2 or $A_{PbS\text{-}DNA\text{-}CNT} = \pi*(1.5)^2 \approx 7.1$ nm^2 ($\pi = 3.14$). The number of DNA-CNTs or PbS-DNA-CNTs in the bundle can then be simply estimated as $N_{DNA\text{-}CNT} = 544/1.54 \approx 353$ or $N_{PbS\text{-}DNA\text{-}CNT} = 2292/7.1 \approx 322$. Note that this number should be the upper limit of the quantities in the bundles since the profiles are assumed to be 100% occupied by DNA-CNTs or the hybrids.

To investigate the photoresponsive properties of the prepared devices, we performed real-time measurement of the current through the source (s) and drain (d) electrodes (I_{sd}) with a constant voltage (V_{sd}, 1 V). Lasers of different wavelengths were cast on the devices to monitor the photoresponses of them.

In detail, electrical measurements were performed using a probe station (PS-100, Lakeshore) equipped with a semiconducting parameter analyser (Keithley, 4200SCS) at room temperature. The analyser recorded the current through the devices (I_{sd}) where a constant voltage (1 V) was applied to the source and drain electrodes. After the current was stable, lasers of different wavelength (650nm, 532nm and 405nm) were cast onto the devices. After a duration of c.a. 20 s, the lasers were turned off. We repeated this process to test the reproducibility of the devices.

3.3.2 Photoresponsive performances

In ambient conditions, after illuminating the DNA-CNT device with 405 nm laser, an I_{sd} decrease as great as 60% was immediately observed; the current recovered gradually after switching off the laser (***Figure 3-6 a)***, which took c.a.200 s to reach 80% of the initial current level (the relative real-time current is reported as $\boldsymbol{I/I_0}$ for better illustration of current change, $\boldsymbol{I}$ represents the absolute real-time current value and $\boldsymbol{I_0}$ equals to the mean current value before the first laser illumination upon the device). For the implemented DNA-CNT device, the results demonstrated an improved photo-responsive performance compared to what was previously observed by Li et al. in spin-coated films of CdS-CNTs where CdS QDs were believed to interact with CNTs and a current change of 20% with a corresponding recovery time of about 200 s was obtained.[32]

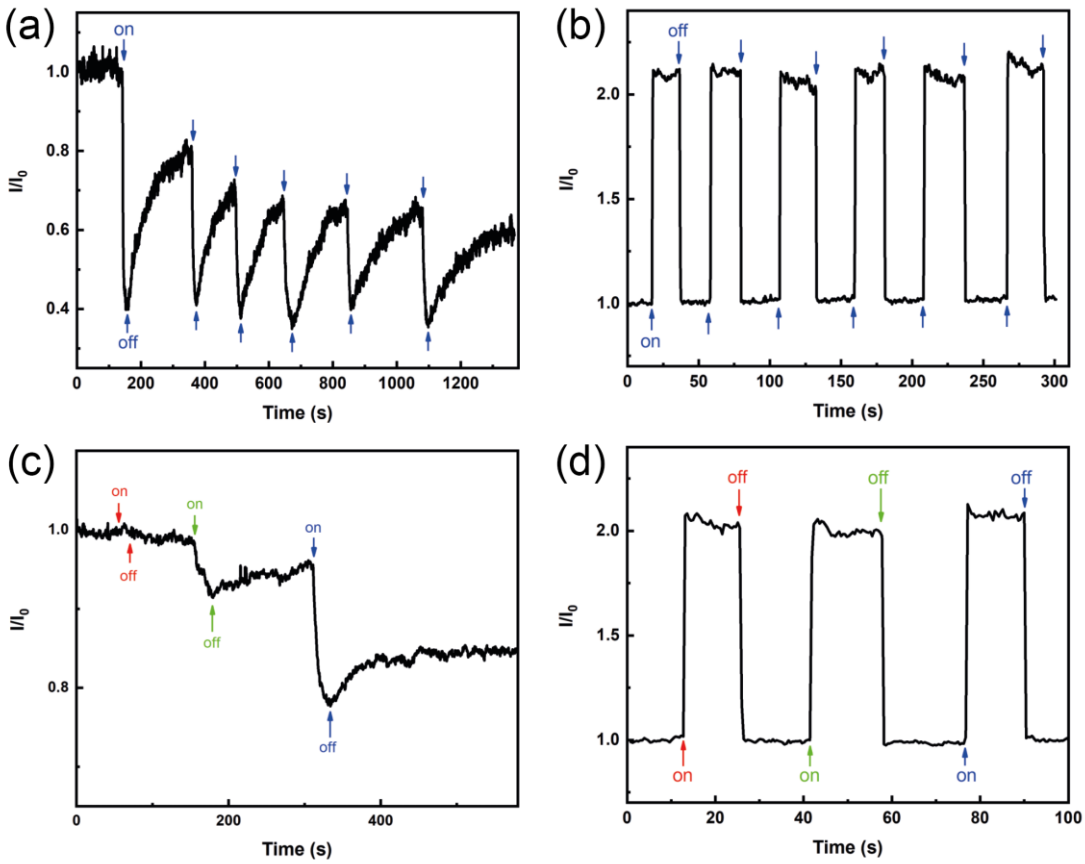

Figure 3-6. *Photoinduced electrical responses (405 nm laser applied) and wavelength dependence test of the devices in ambient conditions. (a, b) real-time photoinduced electrical response with laser turned on and off from (a) DNA-CNT device and (b) PbS-DNA-CNT device; (c, d) wavelength dependence test with sequential illuminations by red (650 nm), green (532 nm) and blue (405 nm) light for (c) DNA-CNT device and (d) PbS-DNA-CNT device. The current is reported here as* I/I_0 *for better illustration of current change,* I *represents the absolute real-time current value and* I_0 *equals to the mean current value before the first laser illumination upon the device.*

For PbS-CNT hybrids, an opposite and faster photoresponse was observed, i.e. a sharp current increase in 1 s with laser illumination and a sharp decrease in 1 s upon switching off the light source (***Figure 3-6 b***). Notably, this photo-induced current contributed to

more than 100% increase in the device's measured I_{sd} and the photoresponse cycle was highly repeatable.

The wavelength dependence of our devices was tested with 650 nm, 532 nm and 405 nm lasers sequentially. For DNA-CNT device, no obvious response to red light (650 nm) was observed while responses (drop in current) to green (532 nm) and blue (405 nm) light were recorded (***Figure 3-6 c***). This correlation trend between the photoresponse and incident light wavelength is in accordance with the π-plasmon absorption of CNTs[47,48]. As a result, it is reasonable to attribute its wavelength dependence to the CNT π-plasmon absorption.

For the PbS-DNA-CNT based device, we observed a photoresponse to all three wavelengths (i.e. 650 nm, 532 nm, 405 nm) with similar magnitude (***Figure 3-6 d***). In fact, both the DNA-CNTs and the PbS QDs absorb strongly at 650 nm, 532 nm and 405 nm (***Figure 3-7, Figure 3-8***), which suggests that the excitation of DNA-CNTs/PbS QDs could be one potential event behind the photoresponse of PbS-DNA-CNT system.

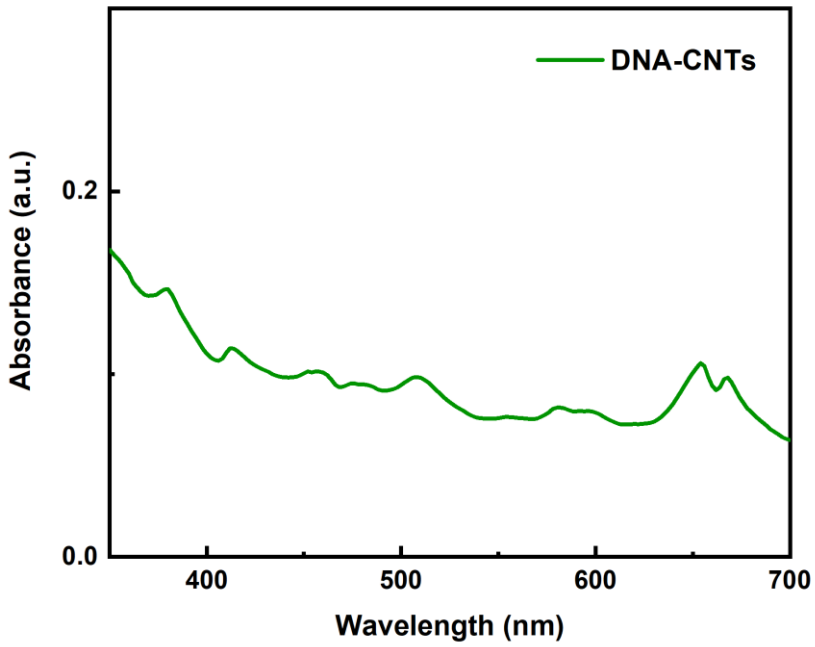

Figure 3-7. *Absorption spectrum of DNA-CNTs.*

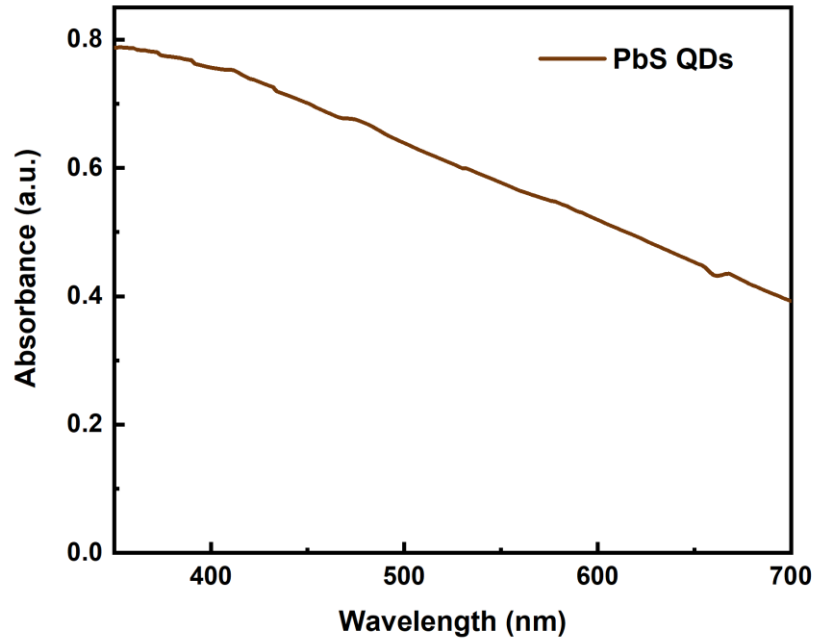

Figure 3-8. *Absorption spectrum of PbS QDs.*

Notably, very different photo-responsive features (current change direction, speed, and wavelength dependence) between DNA-CNT and PbS-DNA-CNT devices may reflect some key differences in the photo-induced exited state dynamics of the corresponding systems. Importantly, by organizing DNA-CNT and assembled PbS-DNA-CNT nanohybrids that work in varied photo-inducible wavelength ranges on the same chip, we have fabricated a nanodevice with multiplexed sensing capability.

3.4 Further investigations

To further understand the main mechanisms behind the observed photoresponses, we carried out more investigations on the corresponding systems. All the above-mentioned performances of the devices were acquired in ambient conditions (i.e. in air). In order to see whether the presence of air played a role in the photo-responsive behaviors of our devices, we tested the photoresponses in a vacuum chamber (10^{-6} bar). Interestingly, for DNA-CNT devices, a drop in the current was again obtained upon light illumination but the current recovery after switching the light off was no longer observed (***Figure 3-9 a***).

In the meantime, we monitored the current dependence on gate voltage of DNA-CNT device and found that it displayed typical p-type features [***Figure 3-9 b***, gate dependence features of the devices were measured with gate bias sweeping mode (-10 V to 10 V) to record the source-drain current (I_{sd}) versus gate bias (V_g)]. The p-type behavior of DNA-CNT is caused by the adsorbed electron withdrawing molecules (e.g. oxygen) on the CNT surface.[49,50] As a result, a photo-induced molecular desorption model was suggested to best describe the mechanism behind the DNA-CNT

photoresponses, which was previously observed from devices based on chemical vapor deposition (CVD) grown SWCNTs.[51] In brief, due to the π-plasmon absorption of CNTs, the oxygen molecules previously adsorbed to DNA-CNT were removed (molecular desorption) from the CNT surface upon light illumination, returning electrons back into the CNT. Given the p-type nature of the conducting DNA-CNT, this electron injection leads to the population decrease of the holes (the major charge carriers) in the CNTs, resulting in the decrease in device conductivity (drop in current). Additionally, the wavelength-dependent features of DNA-CNT device have been positively correlated to the optical absorption of π-plasmon in CNTs,[47] where a bigger drop in current has corresponded to a stronger absorption. This is in line with the model in which the π-plasmon of the CNTs are responsible for the molecular desorption.[51] Significantly, this photo-responsive feature based on the molecular desorption mechanism highlights the potential of DNA-CNTs in light-gas correlated sensing applications, with the merits of efficient dispersion and manipulation in aqueous solutions.

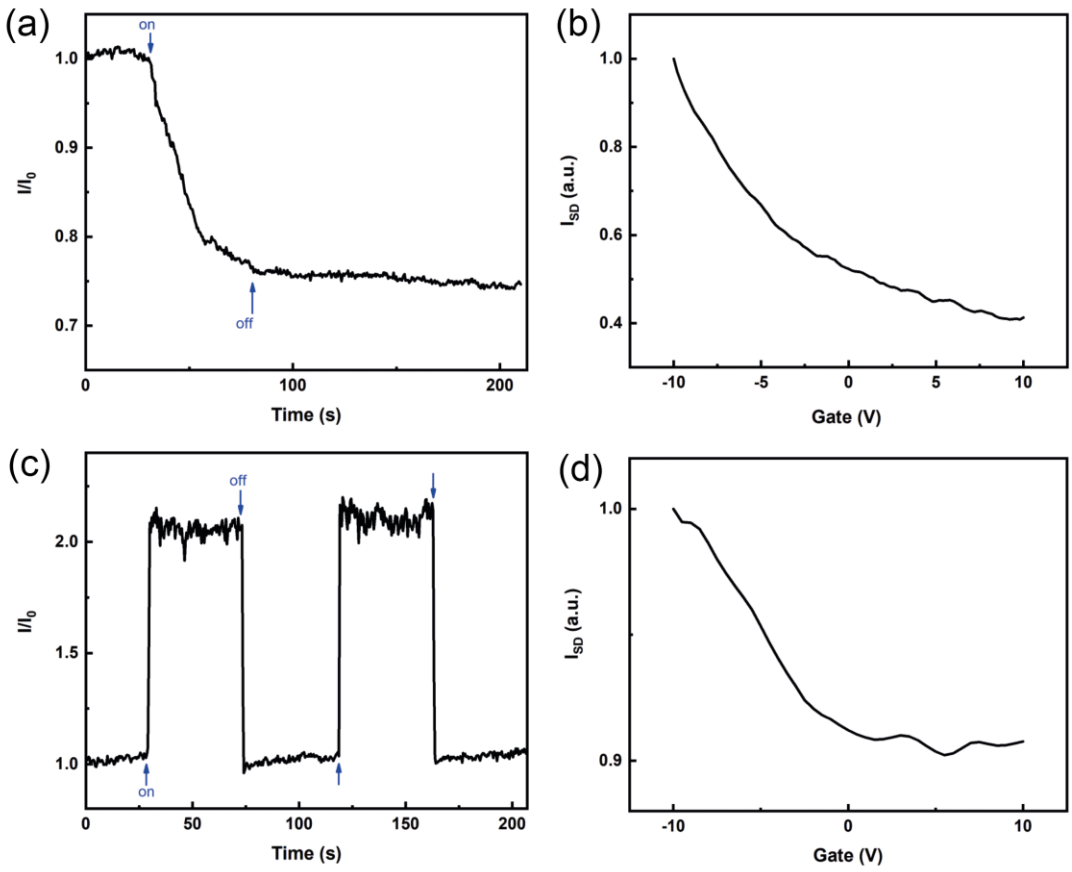

Figure 3-9. *Photoinduced electrical response tests in vacuum (10^{-6} bar) and gate dependence measurements. (a) photoresponse of DNA-CNT device in vacuum (405 nm laser applied); (b) I_{sd}-V_G curve of DNA-CNT device; (c) photoresponse of PbS-DNA-CNT device in vacuum (405 nm laser applied); (d) I_{sd}-V_G curve of PbS-DNA-CNT device.*

In terms of the PbS-DNA-CNT device, no obvious change in photoresponse features was observed in vacuum as compared to that in air (***Figure 3-9 c***). Meanwhile, the device also displayed p-type gate dependence as was the case for DNA-CNT device (***Figure 3-9 d***). It is important to note that the device was no longer conductive after removing SWCNTs in the hybrids by oxygen plasma (OP) (***Figure 3-10***). This confirms the role of SWCNTs as the 1D conductive pathway in the PbS-DNA-CNT device.

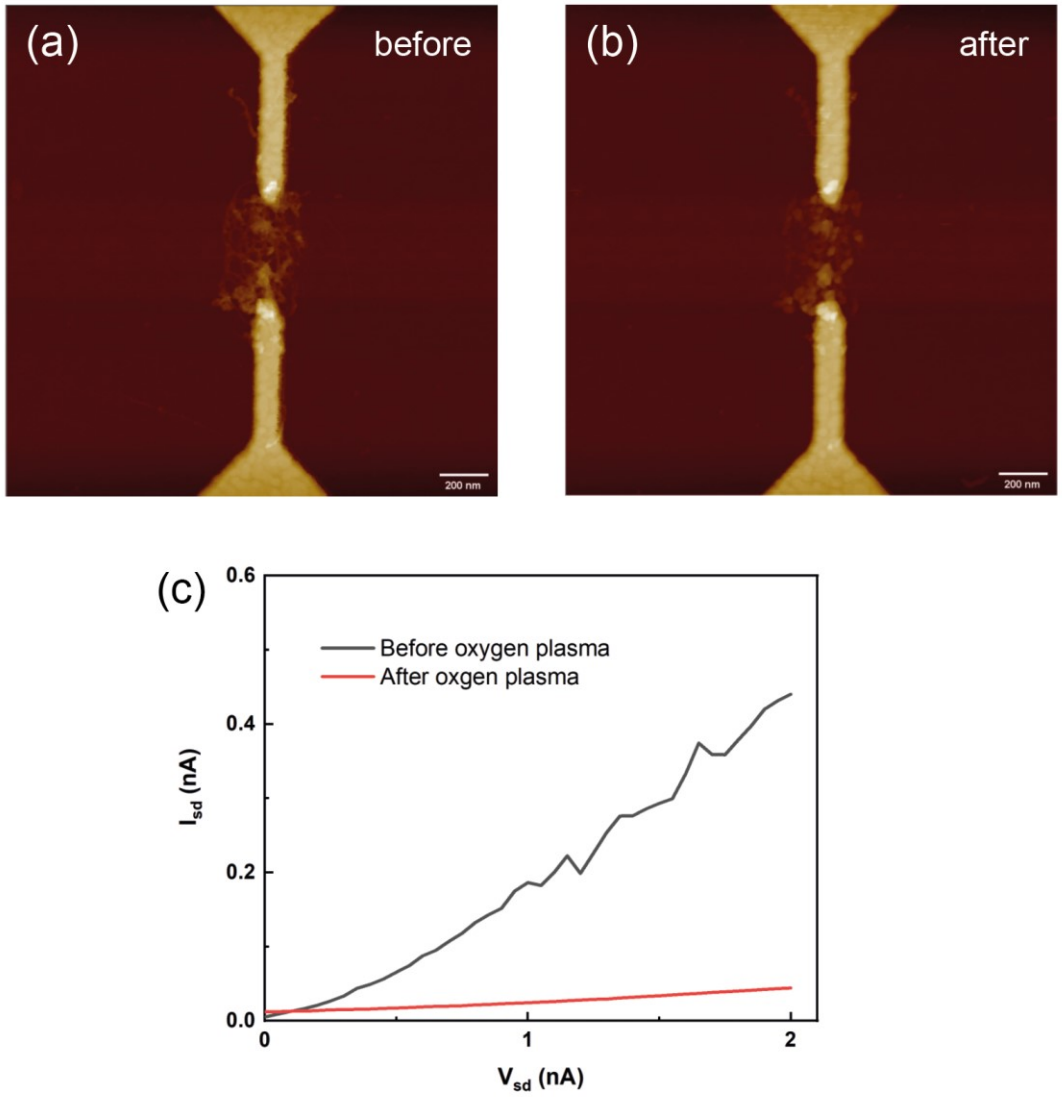

Figure 3-10. *AFM and conductivity comparison of the same PbS-DNA-CNT device before and after the oxygen plasma (OP) treatment. (a) AFM image of the device before OP treatment; (b) AFM image of the device after OP treatment; (c) conductivity of the device before and after the OP treatment.*

Consequently, a mechanism that differs from molecular photodesorption model is suggested for this system. Since an increase in current was observed upon light illumination, an electron transfer from CNT to attached PbS QDs is the most likely

event, considering the p-type nature of the devices. We then probed the excited state behaviors of DNA-CNT and PbS-DNA-CNT hybrids via TAS at 1152 nm [corresponding to the E_{11} transition of (7,6) chirality SWCNTs] and with a pump at 650 nm. As is presented in ***Figure 3-11***, after 650 nm excitation, the PbS-DNA-CNTs exhibit a slower bleaching recovery compared to that of DNA-CNTs.

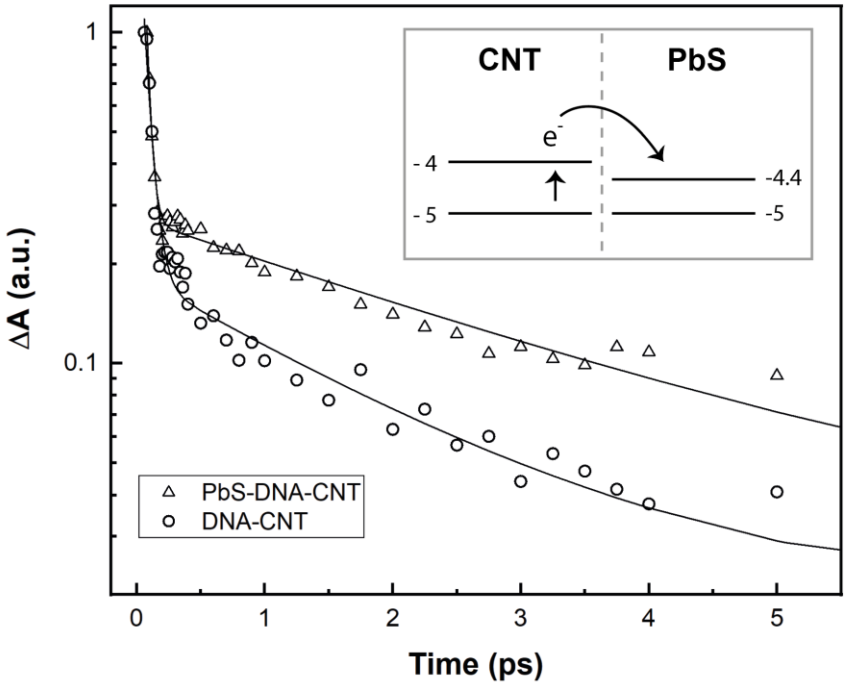

Figure 3-11. *Excited state lifetime investigations of DNA-CNTs and PbS-DNA-CNT hybrids (pump at 650 nm). Normalized transient absorption kinetics of PbS-DNA-CNTs and DNA-CNTs at 1152 nm are shown [corresponds to the E_{11} transition of the (7,6) SWCNTs] and the solid lines are the kinetic fits (see Supporting Information for details). The inset shows the energy band positions of SWCNT and PbS QDs in the system.*

We analysed the bleaching recovery of DNA-CNT and PbS-DNA-CNT hybrids from the acquired TAS data with a biexponential kinetics model:

$$Abs(t)\tau = A_1 e^{-t/\tau_1} + A_2 e^{-t/\tau_2}$$

where t is time, A is amplitude, and τ is the decay lifetime.

The average lifetimes of the samples were calculated from the weighted average of the two lifetimes:

$$\langle\tau\rangle = \sum_{i=1}^{2} A_i\tau_i^2 \Big/ \sum_{i=1}^{2} A_i\tau_i$$

The obtained values from the kinetic analysis are displayed in Table 1.

	A_1	τ_1 (ps)	A_2	τ_2 (ps)	$\langle\tau\rangle$ (ps)
DNA-CNT	2.712±0.286	0.055±0.005	0.166±0.021	1.777±0.536	1.198
PbS-DNA-CNT	9.090±1.357	0.032±0.002	0.252±0.009	3.058±0.283	2.228

Table 1. *Lifetimes and amplitudes of the bleaching recovery of DNA-CNT and PbS-DNA-CNT hybrids calculated from the fitting with biexponential kinetics.*

The averaged lifetimes were calculated to be 2.2 ps and 1.2 ps for PbS-DNA-CNTs and DNA-CNTs, respectively. This evidence strongly indicates an electron transferring pathway from the excited CNT to PbS QDs, contributing to the slower recovery of the CNT ground state. The suggested event also agrees with the reported energy band positions of SWCNTs and PbS as shown in the inset of ***Figure 3-11***, where a net electron transfer is energetically allowed when CNTs are excited.[52,53]

3.5 General applicability: DNA-CNT templated CdS-DNA-CNT hybrids

To prove that our one-pot assembly method exploiting DNA-CNT as the template is of general applicability, we have also assembled CdS-DNA-CNT hybrids with the same approach simply by changing Pb^{2+} to Cd^{2+} during the assembly procedure (see ***Figure 3-12*** and ***Figure 3-13*** for AFM characterizations). The assembled CdS-DNA-CNT hybrids were then implemented into nanodevice (***Figure 3-14***) and displayed similar photo-responsive/wavelength dependence features as were observed in DNA-CNT devices (***Figure 3-15, Figure 3-16***).

In terms of further investigations, compared with DNA-CNT devices, similar observations were acquired for CdS-DNA-CNT counterparts (i.e. no clear current recovery after switching off the light when the testing condition was changed to vacuum and p-typed gate-dependence features: ***Figure 3-17, Figure 3-18***). Additionally, no clear evidence suggesting the effective electron transfer between excited CdS QDs and CNTs was obtained from the comparison of excited state absorptions of DNA-CNTs and CdS-DNA-CNT hybrids (***Figure 3-19, Figure 3-20***). We expected a change in bleaching recovery kinetics if there was electron transfer when the CNTs were in contact to excited CdS QDs. As presented in ***Figure 3-20***, after 405 nm excitation, no obvious difference in the bleaching recovery between CdS-DNA-CNTs and DNA-CNTs was observed.

Consequently, the above-mentioned observations indicated that the molecular photodesorption was likely to be the dominant process accountable for the photo-responsive features of CdS-DNA-CNT device, instead of the previously suggested electron transfer model for CdS-CNT systems in air.[32] Moreover, the successful assembly of CdS-DNA-CNT hybrids demonstrates that the DNA-CNT based templating approach is of general applicability for similar materials compatible with aqueous solutions.

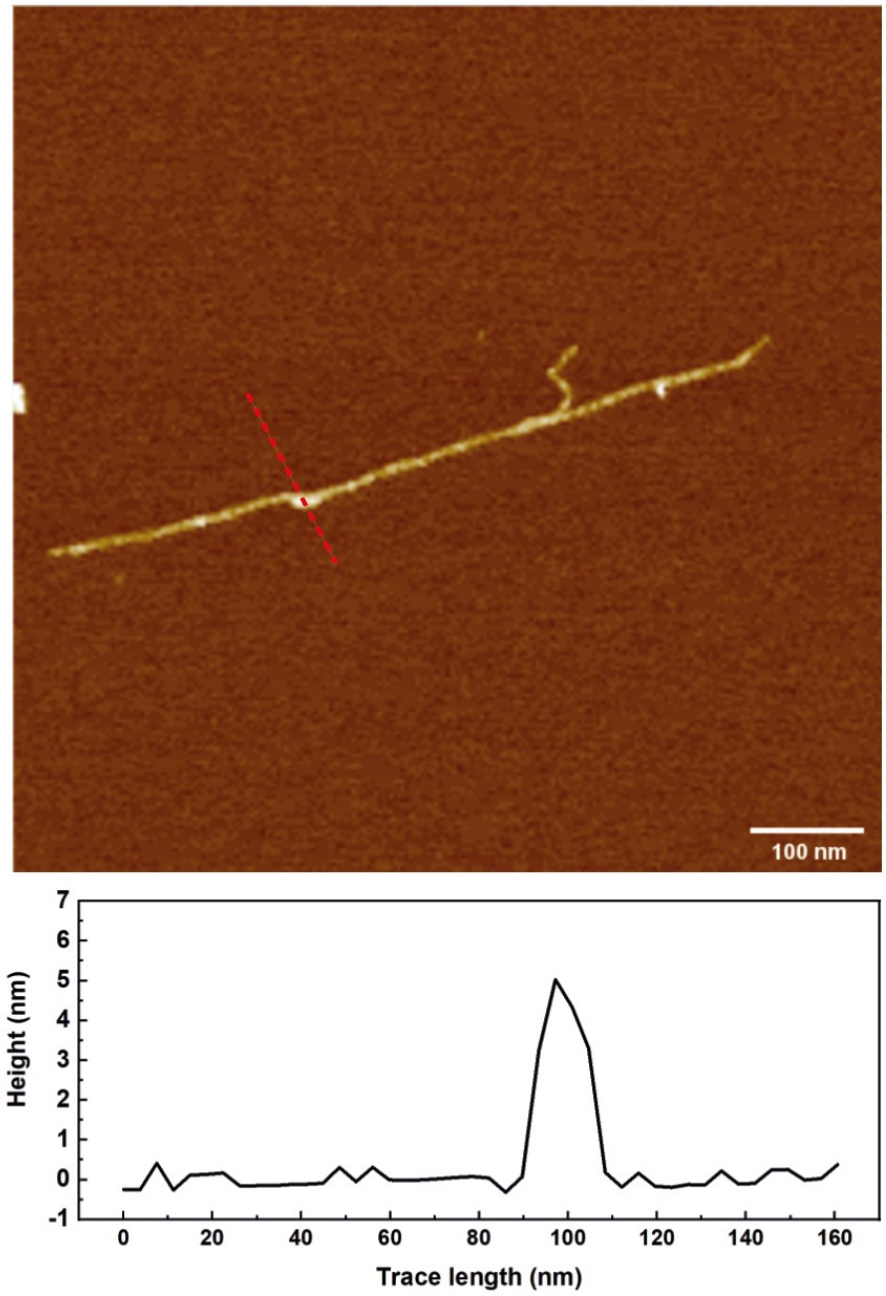

Figure 3-12. *AFM image of a typical assembled CdS-DNA-CNT hybrid. The height profile follows the corresponding red dashed line in the AFM image above it, indicating a typical size of 5 nm.*

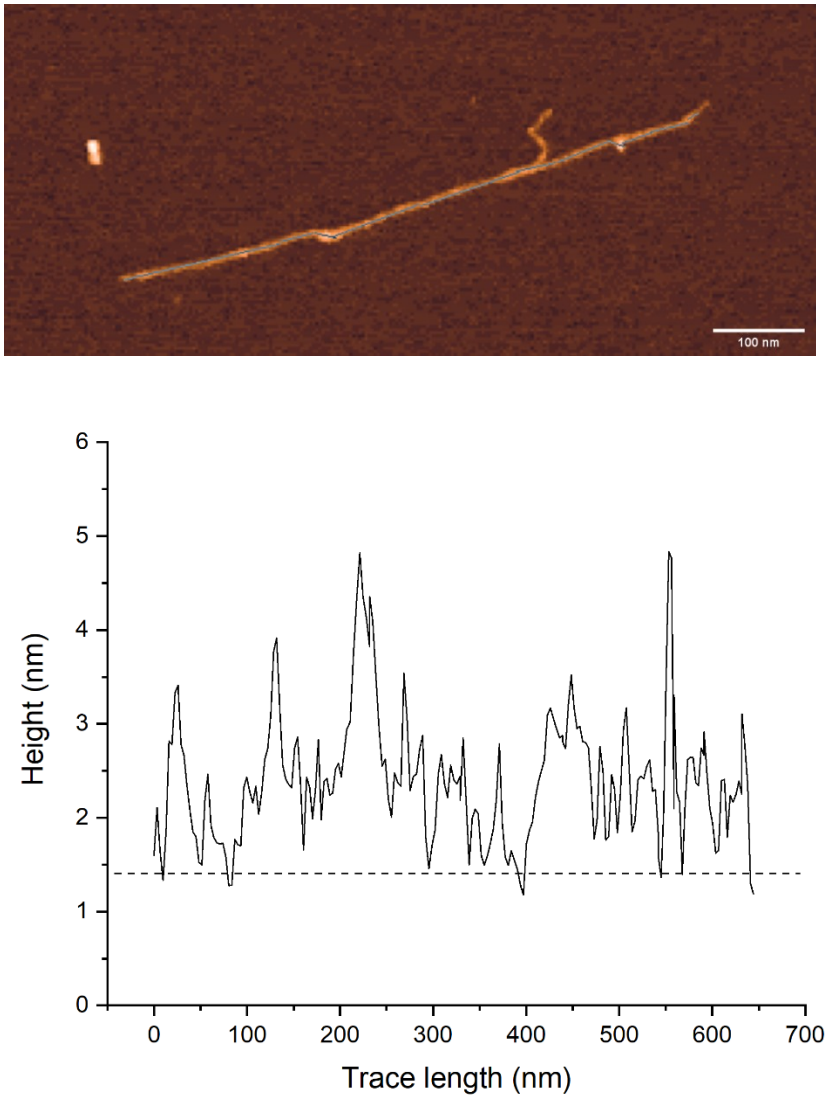

Figure 3-13. *Height profile along the length of CdS-DNA-CNT. Top: AFM image of CdS-DNA-CNT hybrid; bottom: height profile along the length of the shown CdS-DNA-CNT (the dashed line indicates the DNA-CNT average height of 1.4 nm).*

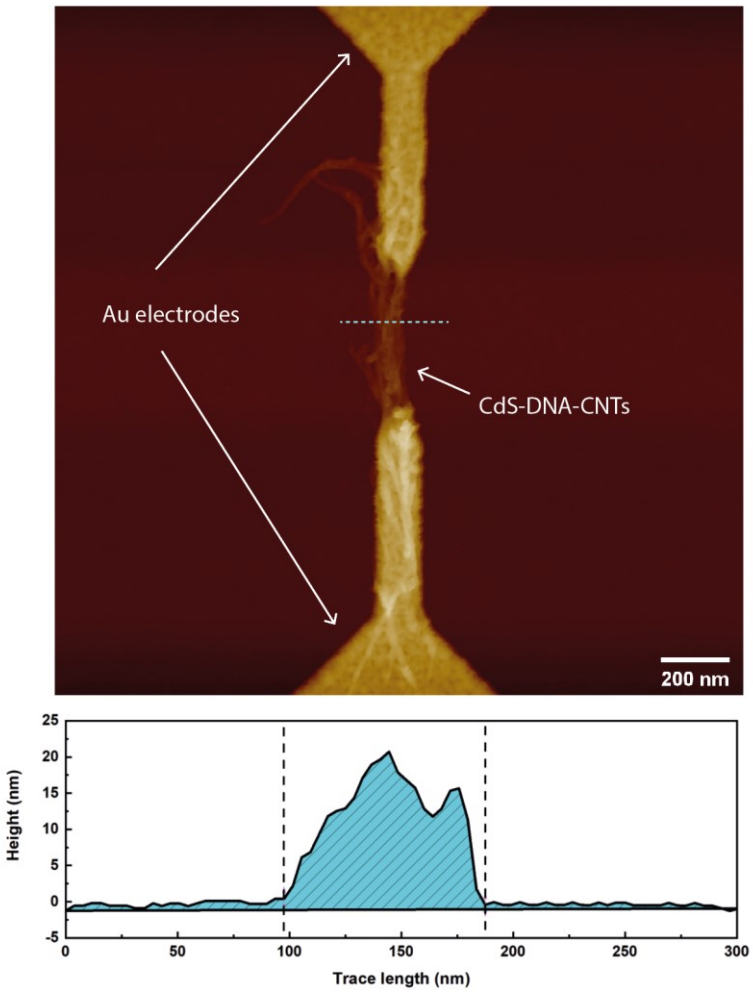

Figure 3-14. *AFM of a typical CdS-DNA-CNT device on chip (top) and height profile along to the dashed line shown in the image (bottom).*

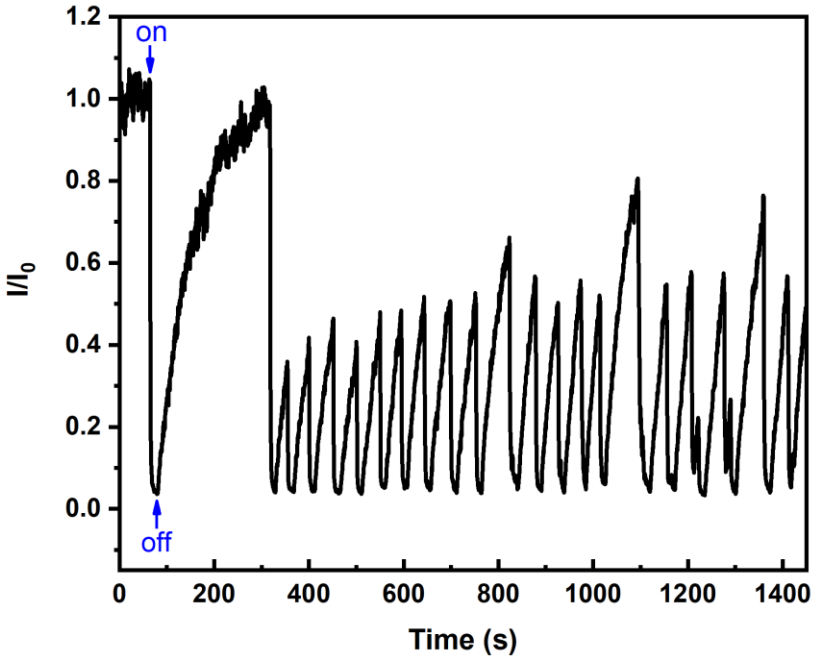

Figure 3-15. *Photoresponse of CdS-DNA-CNT device (405 nm laser applied) in ambient conditions.*

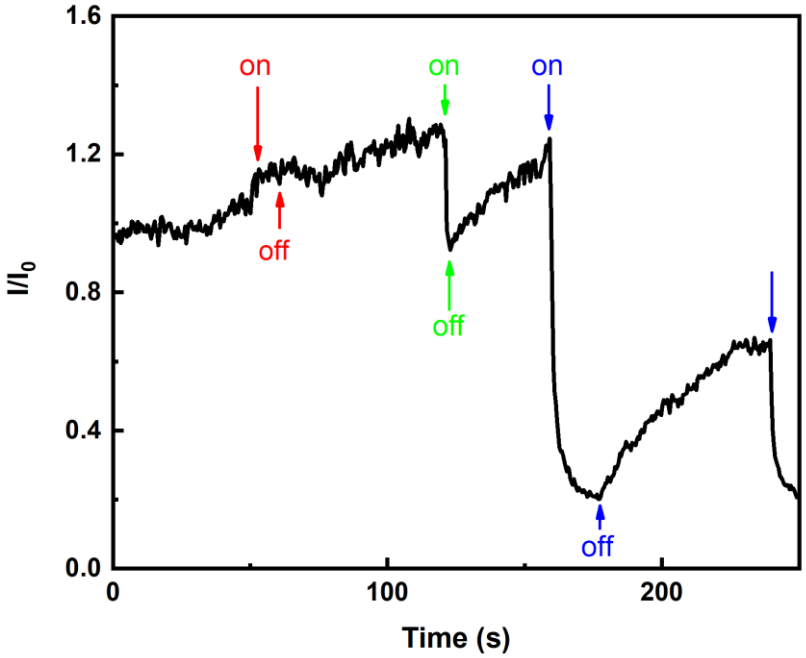

Figure 3-16. *Wavelength dependence test with sequential illuminations by red (650 nm), green (532 nm) and blue (405 nm) light for CdS-DNA-CNT device in ambient conditions.*

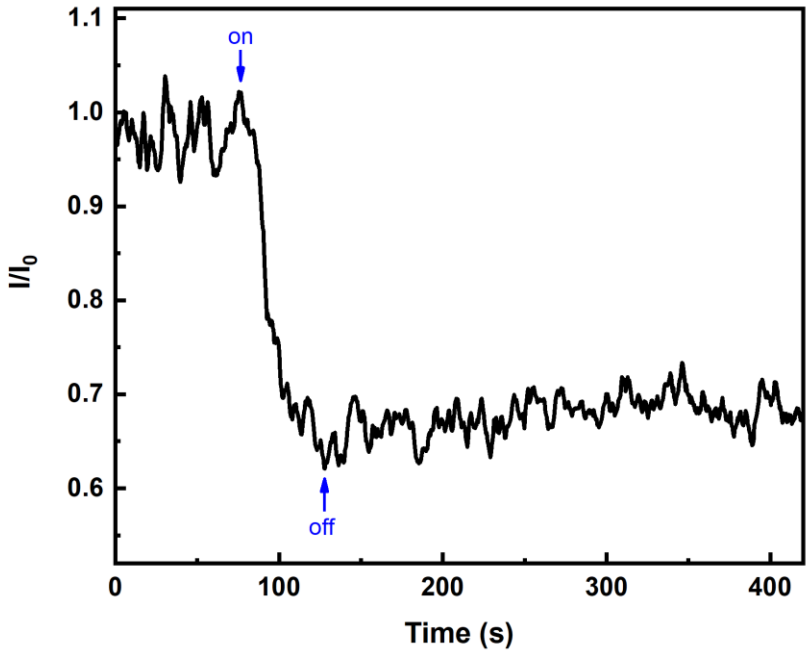

Figure 3-17. *Photoresponse of CdS-DNA-CNT device in vacuum (405 nm laser applied). Note that there is no obvious recovery in current after switching off the laser.*

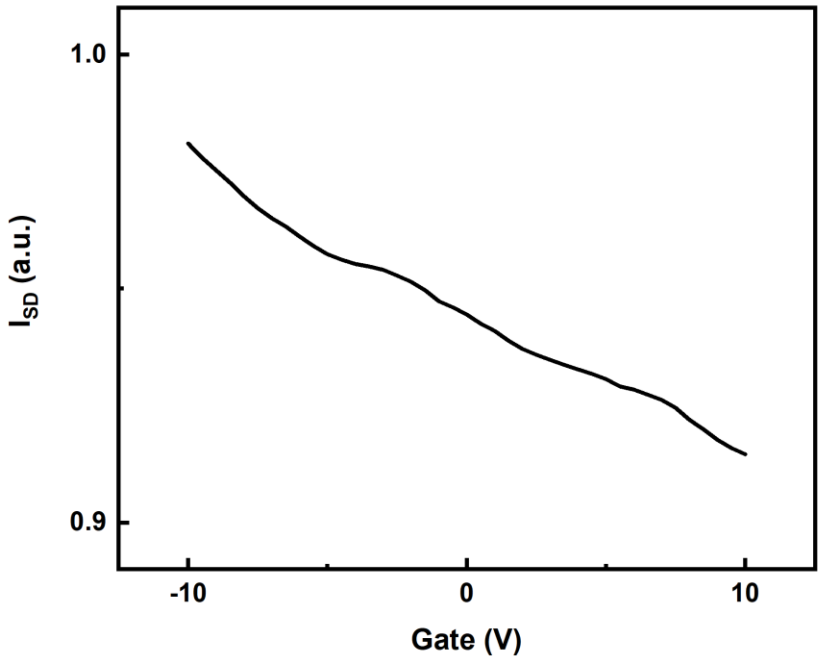

Figure 3-18. *Gate dependence of CdS-DNA-CNT device (I_{sd}-V_G curve), indicating its p-type polarity.*

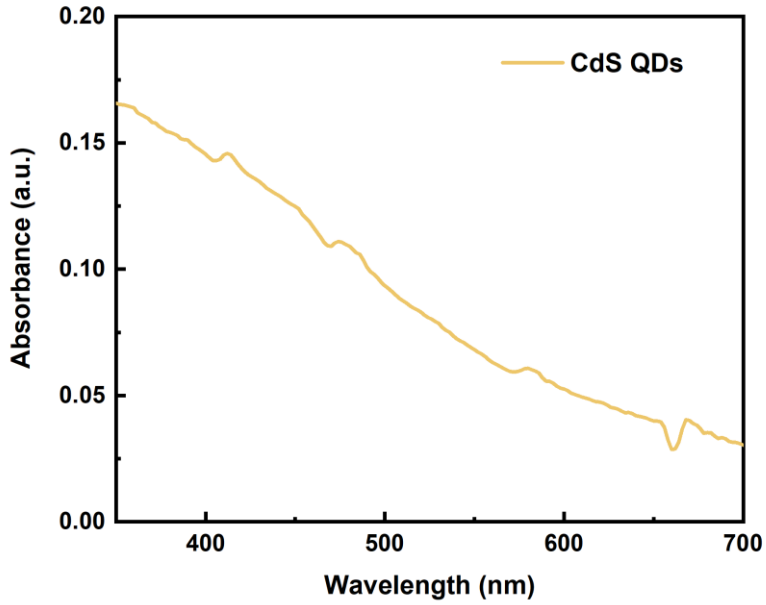

Figure 3-19. *Absorption spectrum of CdS QDs. Note that CdS QDs absorb at 405 nm.*

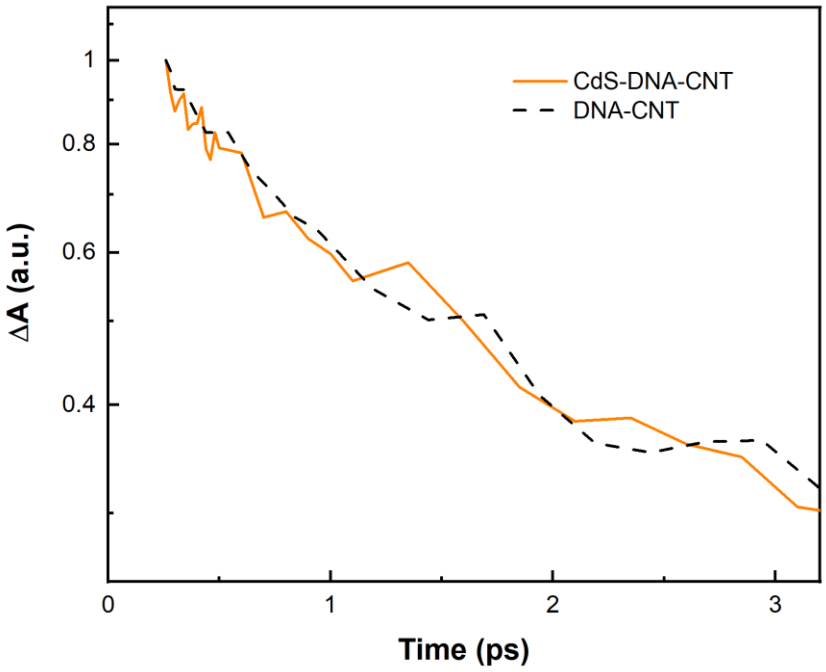

Figure 3-20. *Excited state lifetime investigations of DNA-CNTs and CdS-DNA-CNT hybrids (pump at 405 nm). Normalized transient absorption kinetics of CdS-DNA-CNTs*

and DNA-CNTs at 1152 nm are shown [corresponds to the E_{11} transition of the (7,6) SWCNTs].

3.6 Conclusion

We have demonstrated the successful construction of a multiplexed photo-responsive chip from DNA-CNTs, PbS-DNA-CNT and CdS-DNA-CNT hybrids (***Figure 3-21***), and investigated the key mechanisms behind the corresponding photoresponses. In brief, a facile one-pot strategy of assembling PbS-DNA-CNT and CdS-DNA-CNT nanohybrids with DNA-CNTs as the effective one-dimensional templates has been achieved. Benefiting from the effective use of electrostatic interactions between metal cations and negatively charged DNA-CNT sidewall, CdS and PbS QDs were grown directly along the sidewall of these DNA-CNT templates in aqueous solutions with sequential addition of metal cations and S^{2-}, which was confirmed by AFM. By organizing both DNA-CNTs and assembled hybrids on the same pre-patterned chip via dielectrophoresis (DEP), we fabricated our nanoscale devices with multiplexed detection capability. With their nanoscale dimensions, devices have achieved photoresponses of more than 100% current change within 1 s. Additionally, very different photoresponses were observed and these were explained by different mechanisms of device operation, which were confirmed by us from further electrical (photoresponse measurement in vacuum and gate dependence test) and excited state lifetime (TAS measurement) investigations.

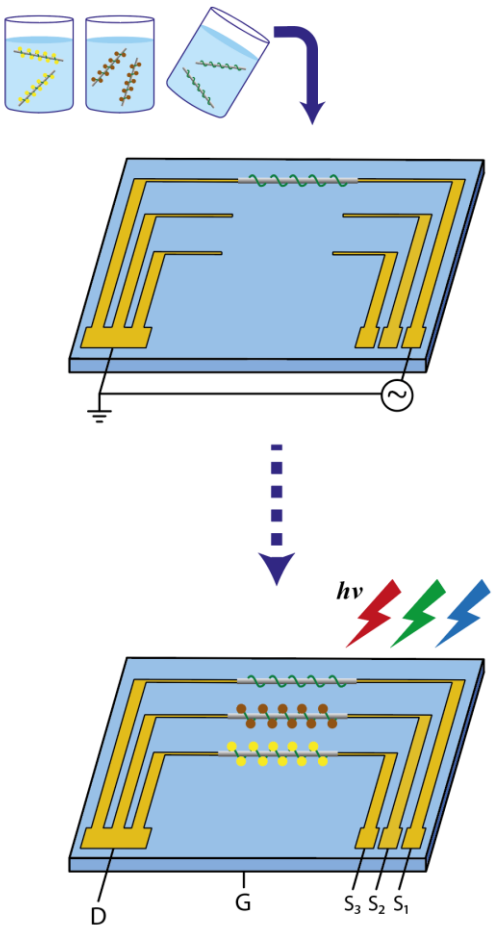

Figure 3-21. *The construction of multiplexed photo-responsive device from aqueous solutions of DNA-CNTs and templated PbS-DNA-CNT/CdS-DNA-CNT hybrids.*

Two vital roles of DNA-CNTs were revealed: i) the suggested photo-induced molecular desorption process for DNA-CNT device highlights the potential of DNA-CNTs for the construction of light-gas correlated sensing devices; ii) DNA-CNTs can be the effective templates for the assembly of varied CNT-inorganic nanohybrid materials in aqueous solutions. This strategy opens the way in the design of optoelectronic devices with a general applicability and multiplexed sensing potential.

3.7 Materials and methods

Hybrids assembly

In brief, (7,6) enriched SWCNTs (Sigma Aldrich) were wrapped by single-strand DNA [ssDNA, $(GT)_{20}$] (Integrated DNA Technologies, Inc) in 0.1M NaCl (Fisher Scientific) solution under 60 min sonication (VWR basin sonicator, Model USC300TH) to form the DNA-CNTs. The undispersed CNTs and residues (amorphous carbon etc.) were removed by keeping only the supernatant after 90 min centrifugation at 16000 g (Biofuge pico D-37520, Heraeus Instruments). The supernatant solution was then dialysed (Thermo Fisher Scientific, Slide-A-Lyzer™ MINI Dialysis Device, 20K MWCO) against MiliQ® H_2O overnight. The DNA-CNT aqueous solution can then be stored under 4°C as stock solution.

To assemble the CdS/PbS-DNA-CNT hybrids, the stock DNA-CNT solutions were diluted 10x with MiliQ® H_2O. To every 10 μL of diluted DNA-CNT solution, 25 μL of H_2O and 10 μL of 5mM M^{2+} (Cd^{2+} or Pb^{2+} dissolved from $Cd(NO_3)_2$ or $Pb(NO_3)_2$, Sigma Aldrich) were added and the solution was incubated at 4°C overnight; the incubated solution was then added 10 μL of 5mM S^{2-} (dissolved from Na_2S, Sigma Aldrich) and subject to overnight incubation. The incubated solution was dialysed against MiliQ® H_2O for 3 h. The incubated solutions were dialyzed against MiliQ® H_2O for 3 h and the CdS-DNA-CNT or PbS-DNA-CNT hybrids were then ready for device implementation and further investigations.

AFM characterization

Topography analysis of the SWCNT molecular junctions were imaged with a Bruker Dimension Icon atomic force microscope (AFM) with ScanAsyst Air tips (tip radius 12

nm) in tapping mode with 512 samples per line and a scan rate of 1.2 Hz. The sample solutions were deposited onto freshly cleaved mica discs, rinsed with water and dried before AFM measurement.

The height/size analysis were carried out with the use of Nanoscope Analysis (Bruker, V 1.5), Gwyddion (V 2.56) and ImageJ (V 1.52p).

Device fabrication

Gold electrodes was fabricated by our collaborators, following the protocol reported in our previous publication [1]. A drop of dialysed DNA-CNT or CdS/PbS-DNA-CNT hybrids solution (5μL) was cast on the gold electrodes. AC voltage was applied to the electrode with a V_{p-p} of 6 V at a frequency of 400KHz. After a duration of 30s, the voltage was turned off as enough DNA-CNTs or CdS/PbS-DNA-CNT hybrids had been immobilised between the gold electrodes. Subsequently, the electrodes were rinsed with water and blow-dried for AFM characterization and electrical measurement.

To prepare multiplexed platform for photodetection, we immobilised DNA-CNT, CdS-DNA-CNT and PbS-DNA-CNT hybrids on the same chip via dielectrophoresis (DEP). Briefly, we first cast DNA-CNT solution on the electrodes and applied AC voltage. DNA-CNTs would be only immobilised between electrodes where AC voltage was applied. Subsequently, CdS-DNA-CNT and PbS-DNA-CNT hybrids solutions were cast on the same chip, followed by application of AC voltage between electrodes which had not been used previously. Thus, DNA-CNT, CdS-DNA-CNT and PbS-DNA-CNT hybrids were all immobilised separately on the same chip.

Electrical measurement

Real time measurement

Electrical measurements were performed using a probe station (PS-100, Lakeshore) equipped with a semiconducting parameter analyser (Keithley, 4200SCS) at room temperature. The analyser recorded the current through the devices (I_{sd}) where a constant voltage (1V) was applied to the source and drain electrodes. After the current was stable, lasers of different wavelength (typically, 650nm, 532nm and 405nm) were cast onto the devices. After a duration of 20 s, the lasers were turned off. We repeated this process for more than 30 cycles to test the reproducibility of the devices.

Gate dependence measurement

Gate dependence features of the devices were measured with gate bias sweeping mode (-10 V to 10 V) to record the source-drain current (I_{sd}) versus gate bias (V_g). In addition to measurement in dark, to investigate the influence of light illumination, we also cast the laser on the devices while measuring the gate dependence features of the devices.

Plasma treatment

Plasma treatment of the devices was conducted in a plasma cleaner (Harrick PDC-32G-2, 18 W). In brief, devices based on assembled hybrids were put into the vacuum chamber of plasma cleaner and undergone 5 s plasma treatment. AFM characterization and conductivity test (I_{sd}-V_{sd}) were carried out for devices before and after the plasma treatment (***Figure 3-10***).

Specifically, we compared the AFM images and electrical conductivities of the same CdS-CNT hybrid device before and after the OP treatment that will selectively oxidize the DNA-CNTs within the hybrids. After 5 s OP treatment, the fine wire-like structures found in the AFM image of the same device before OP treatment were no longer observed, leaving only the isolated particle shaped material between nanoelectrodes

(***Figure 3-10 a, b***). Additionally, the conductivity of the device had decreased for more than 10 times after the OP treatment and fell below the minimum effective sensitivity of the analyser equipment (***Figure 3-10 c***). This confirms the role of SWCNTs as the 1D conductive pathway in our devices.

Transient absorption spectroscopy

Samples were interrogated using visible pump, near IR probe transient absorption spectroscopy. The pump pulses were generated using an optical parametric amplifier system (TOPAS Prime Niruvis – Light Conversion), pumped by a 2.5 W, 800 nm, 40 fs duration, 1 kHz repetition rate laser. This pulse was generated using a commercially available Ti:Sapphire regenerative amplification laser system (Spitfire Ace PA – Spectra Physics) seeded by a Ti:Sapphire oscillator laser (MAITAI – Spectra physics) pumped by two 100 ns, 30 W pulsed laser at 532 nm (Ascend – Spectra Physics). The TOPAS system generated pulses at 405 and 650 nm with an average power of ~5 mW, pulse duration of 40 fs and repetition rate of 1 kHz. These beams were attenuated with a neutral density filter and focused onto the sample using a CaF_2 lens to achieve the fluences described. The probe pulse was generated using a second optical parametric amplifier (TOPAS-C – Light Conversion) pumped by a 1.7 W, 800 nm beam, generated by the same regenerative amplifier as described above. This second TOPAS system output 1600 nm, 40 fs pulses with an average power of ~100 mW and a repetition rate of 1 kHz. This pulse was attenuated by a neutral density filter and then focused using a CaF_2 (50 mm focal length) lens onto a sapphire crystal 2 mm thick to generate a super continuum spanning from ~1100-1400 nm. This super continuum pulse was focused by a second 50 mm focal length CaF_2 lens and then focussed onto the sample using a six-inch focal length unprotected gold off-axis parabolic mirror where it intercepted the

pump beam. A delay between the pump and probe pulses, Δt, was generated by delaying the probe beam using an unprotected gold retroreflector mounted on a 500 mm delay stage. Samples were placed into a one-millimetre quartz cuvette through which the two beams crossed at relative crossing angle of ~5°. The probe light was collected using a commercially available IR spectrometer (IHR320 – Horiba). The pump beam was chopped by a mechanical chopper (Thorlabs) at 500 Hz so that every other probe pulse passed through photoexcited sample. Transient absorption spectra at various delay times, Δt, were generated by comparing the signal at the detector between pumped and unpumped probe pulse pairs.

3.8 References

1. Eder, D. Carbon nanotube-inorganic hybrids. *Chem. Rev.* **110**, 1348–1385 (2010).

2. Shearer, C. J., Cherevan, A. & Eder, D. Application and future challenges of functional nanocarbon hybrids. *Adv. Mater.* **26**, 2295–2318 (2014).

3. Padgaonkar, S., Olding, J. N., Lauhon, L. J., Hersam, M. C. & Weiss, E. A. Emergent Optoelectronic Properties of Mixed-Dimensional Heterojunctions. *Acc. Chem. Res.* **53**, 763–772 (2020).

4. Zhang, X., Hou, L. & Samorì, P. Coupling carbon nanomaterials with photochromic molecules for the generation of optically responsive materials. *Nature Communications* **7**, (2016).

5. Peng, X., Chen, J., Misewich, J. A. & Wong, S. S. Carbon nanotube–nanocrystal heterostructures. *Chem. Soc. Rev.* **38**, 1076 (2009).

6. Attanzio, A. *et al.* Carbon Nanotube-Quantum Dot Nanohybrids: Coupling with Single-Particle Control in Aqueous Solution. *Small* **13**, (2017).

7. Freeley, M. *et al.* Tuning the Coupling in Single-Molecule Heterostructures: DNA-Programmed and Reconfigurable Carbon Nanotube-Based Nanohybrids. *Adv. Sci.* **5**, (2018).

8. Shao, D. *et al.* Organic-Inorganic Heterointerfaces for Ultrasensitive Detection of Ultraviolet Light. *Nano Lett.* **15**, 3787–3792 (2015).

9. Xie, Y. *et al.* Broad-spectral-response nanocarbon bulk-heterojunction excitonic photodetectors. *Adv. Mater.* **25**, 3433–3437 (2013).

10. Lipomi, D. J. *et al.* Skin-like pressure and strain sensors based on transparent elastic films of carbon nanotubes. *Nat. Nanotechnol.* **6**, 788–792 (2011).

11. Konstantatos, G. *et al.* Ultrasensitive solution-cast quantum dot photodetectors. *Nature* **442**, 180–183 (2006).

12. Lin, Y. & Guo, X. Ultrahigh Photogain Nanoscale Hybrid Photodetectors. *Small* **11**, 2856–2861 (2015).

13. García De Arquer, F. P., Lasanta, T., Bernechea, M. & Konstantatos, G. Tailoring the electronic properties of colloidal quantum dots in metal-semiconductor nanocomposites for high performance photodetectors. *Small* **11**, 2636–2641 (2015).

14. Fang, H. *et al.* Solution-Processed Self-Powered Transparent Ultraviolet Photodetectors with Ultrafast Response Speed for High-Performance Communication System. *Adv. Funct. Mater.* **29**, (2019).

15. Yang, X., Liu, Y., Lei, H. & Li, B. An organic-inorganic broadband photodetector based on a single polyaniline nanowire doped with quantum dots. *Nanoscale* **8**, 15529–15537 (2016).

16. Guo, P. *et al.* On-Nanowire Axial Heterojunction Design for High-Performance Photodetectors. *ACS Nano* **10**, 8474–8481 (2016).

17. Clifford, J. P. *et al.* Fast, sensitive and spectrally tuneable colloidal-quantum-dot photodetectors. *Nat. Nanotechnol.* **4**, 40–44 (2009).

18. Park, S., Vosguerichian, M. & Bao, Z. A review of fabrication and applications of carbon nanotube film-based flexible electronics. *Nanoscale* **5**, 1727–1752 (2013).

19. Richter, M., Heumüller, T., Matt, G. J., Heiss, W. & Brabec, C. J. Carbon Photodetectors: The Versatility of Carbon Allotropes. *Advanced Energy Materials* **7**, (2017).

20. Hammel, E. *et al.* Carbon nanofibers for composite applications. in *Carbon* **42**, 1153–1158 (2004).

21. Zaporotskova, I. V., Boroznina, N. P., Parkhomenko, Y. N. & Kozhitov, L. V. Carbon nanotubes: Sensor properties. A review. *Mod. Electron. Mater.* **2**, 95–105 (2016).

22. Kamat, P. V. *et al.* Self-assembled linear bundles of single wall carbon nanotubes and their alignment and deposition as a film in a dc field. *J. Am. Chem. Soc.* **126**, 10757–10762 (2004).

23. Girishkumar, G., Vinodgopal, K. & Kamat, P. V. Carbon nanostructures in portable fuel cells: Single-walled carbon nanotube electrodes for methanol oxidation and oxygen reduction. *J. Phys. Chem. B* **108**, 19960–19966 (2004).

24. Wang, C. *et al.* Proton Exchange Membrane Fuel Cells with Carbon Nanotube Based Electrodes. *Nano Lett.* **4**, 345–348 (2004).

25. Arnold, M. S. *et al.* Recent developments in the photophysics of single-walled carbon nanotubes for their use as active and passive material elements in thin film photovoltaics. *Physical Chemistry Chemical Physics* **15**, 14896–14918 (2013).

26. Gaviria Rojas, W. A. & Hersam, M. C. Chirality-Enriched Carbon Nanotubes for Next-Generation Computing. *Adv. Mater.* 1905654 (2020). doi:10.1002/adma.201905654

27. Lesiak, A. *et al.* Optical sensors based on II-VI quantum dots. *Nanomaterials* **9**, 192 (2019).

28. Moreels, I. *et al.* Size-dependent optical properties of colloidal PbS quantum dots. *ACS Nano* **3**, 3023–3030 (2009).

29. Schulz-Drost, C. *et al.* Innovative inorganic-organic nanohybrid materials: Coupling quantum dots to carbon nanotubes. *Angew. Chemie - Int. Ed.* **49**, 6425–6429 (2010).

30. Robel, I., Bunker, B. A. & Kamat, P. V. Single-walled carbon nanotube-CdS nanocomposites as light-harvesting assemblies: Photoinduced charge-transfer interactions. *Adv. Mater.* **17**, 2458–2463 (2005).

31. Hu, L. *et al.* Light-induced charge transfer in pyrene/CdSe-SWNT hybrids. *Adv. Mater.* **20**, 939–946 (2008).

32. Li, X., Jia, Y. & Cao, A. Tailored single-walled carbon nanotube-CdS nanoparticle hybrids for tunable optoelectronic devices. *ACS Nano* **4**, 506–512 (2010).

33. Saran, R. & Curry, R. J. Lead sulphide nanocrystal photodetector technologies. *Nature Photonics* **10**, 81–92 (2016).

34. Wang, D. *et al.* Controlled fabrication of pbs quantum-dot/carbon-nanotube nanoarchitecture and its significant contribution to near-infrared photon-to-current conversion. *Adv. Funct. Mater.* **21**, 4010–4018 (2011).

35. Ka, I., Le Borgne, V., Ma, D. & El Khakani, M. A. Pulsed laser ablation based direct synthesis of single-wall carbon nanotube/PbS quantum dot nanohybrids exhibiting strong, spectrally wide and fast photoresponse. *Adv. Mater.* **24**, 6289–6294 (2012).

36. Ka, I. *et al.* Multiple exciton generation induced enhancement of the photoresponse of pulsed-laser-ablation synthesized single-wall-carbon-nanotube/PbS-quantum-dots nanohybrids. *Sci. Rep.* **6**, (2016).

37. Feng, W. *et al.* A layer-nanostructured assembly of PbS quantum dot/multiwalled carbon nanotube for a high-performance photoswitch. *Sci. Rep.* **4**, (2014).

38. Molotsky, T., Tamarin, T., Moshe, A. Ben, Markovich, G. & Kotlyar, A. B. Synthesis of chiral silver clusters on a DNA template. in *Journal of Physical Chemistry C* **114**, 15951–15954 (2010).

39. Dong, L. *et al.* DNA-templated semiconductor nanoparticle chains and wires. *Adv. Mater.* **19**, 1748–1751 (2007).

40. Watson, S. M. D., Pike, A. R., Pate, J., Houlton, A. & Horrocks, B. R. DNA-templated nanowires: Morphology and electrical conductivity. *Nanoscale* **6**, 4027–4037 (2014).

41. Li, N. *et al.* Fabrication of Metal Nanostructures on DNA Templates. *ACS Appl. Mater. Interfaces* **11**, 13835–13852 (2019).

42. Ohshiro, T., Zako, T., Watanabe-Tamaki, R., Tanaka, T. & Maeda, M. A facile method towards cyclic assembly of gold nanoparticles using DNA template alone. *Chem. Commun.* **46**, 6132–6134 (2010).

43. Li, X. *et al.* Efficient synthesis of carbon nanotube-nanoparticle hybrids. *Adv. Funct. Mater.* **16**, 2431–2437 (2006).

44. Zheng, M. *et al.* DNA-assisted dispersion and separation of carbon nanotubes. *Nat. Mater.* **2**, 338–342 (2003).

45. Xu, X. *et al.* Reconfigurable Carbon Nanotube Multiplexed Sensing Devices. *Nano Lett.* **18**, 4130–4135 (2018).

46. Clément, P. *et al.* Direct Synthesis of Multiplexed Metal-Nanowire-Based Devices by Using Carbon Nanotubes as Vector Templates. *Angew. Chemie* **131**, 10033–10037 (2019).

47. Landi, B. J., Ruf, H. J., Evans, C. M., Cress, C. D. & Raffaelle, R. P. Purity

assessment of single-wall carbon nanotubes, using optical absorption spectroscopy. *J. Phys. Chem. B* **109**, 9952–9965 (2005).

48. Kazaoui, S. *et al.* Pressure dependence of the optical absorption spectra of single-walled carbon nanotube films. *Phys. Rev. B - Condens. Matter Mater. Phys.* **62**, 1643–1646 (2000).

49. Zettl, A. Extreme oxygen sensitivity of electronic properties of carbon nanotubes. *Science (80-.).* **287**, 1801–1804 (2000).

50. Preenchidos, C. Electronic Properties of Oxidized Carbon Nanotubes" [PRL, 85 8, 1710 (2000)]. *Carbon N. Y.* **49**, 5–7 (2000).

51. Chen, R. J. *et al.* Molecular photodesorption from single-walled carbon nanotubes. *Appl. Phys. Lett.* **79**, 2258–2260 (2001).

52. Pfohl, M. *et al.* Probing the Diameter Limit of Single Walled Carbon Nanotubes in SWCNT: Fullerene Solar Cells. *Adv. Energy Mater.* **6**, (2016).

53. Du, K., Liu, G., Chen, X. & Wang, K. PbS Quantum Dots Sensitized TiO 2 Nanotubes for Photocurrent Enhancement . *J. Electrochem. Soc.* **162**, E251–E257 (2015).

Chapter 4

DNA-Powered Stimuli-Responsive CNT Junctions

4.1 Introduction

The construction of junctions between SWCNTs[1–5] has been investigated for the fabrication of nanoelectronic devices,[6–8] including the use of SWCNTs as nanoelectrodes in molecular transport junctions and single molecule investigations.[2,9–14] Different methods have been explored for junction formation;[1,4,5,15] in this context, the controlled assembly of linear (end-to-end) junctions through in-solution approaches[1,2,16–18] is particularly desirable for the low-cost (solution processable) fabrication[19–21] of carbon nanotube-based devices.[12,14] Nevertheless, although different technologically-relevant nanomaterials have been designed to respond to changes in the surrounding medium,[22,23] the assembly of reversibly reconfigurable end-to-end SWCNT junctions in-solution has yet to be demonstrated; this would allow the facile fabrication of CNT-based stimuli-responsive molecular systems and devices.

In this regard, deoxyribonucleic acid (DNA) is an interesting biopolymer for the implementation of dynamic behavior in nanomechanical architectures[16,18] because of its well-known chemistry (i.e., several modifications are available for the attachment of

functionalities or nanoparticles) and the ability to act as an actuator that responds to a number of different stimuli, depending on its nucleotide sequence. Several studies reported the use of DNA as the molecular material for the construction of designed nano-objects[24,25] or as a scaffold for the assembly of nanoparticles with precise spatial arrangement.[26,27] Furthermore, various response mechanisms to different stimuli were demonstrated to be available for the activation of the dynamics of specific DNA sequences, including strand-displacement,[28] ligand−aptamer complex formation,[29] noncanonical base-pairing,[30] and 3D motif formation (e.g., G-quadruplex and i-motif).[31,32]

Herein, we present a strategy for the controlled assembly of stimuli-responsive end-to-end SWCNT junctions in aqueous solution, employing DNA as a molecular linker: the dynamic behavior of the junctions is controlled by the interaction of the DNA specific sequences with selected external stimuli. As a proof of concept, we fabricated linear assemblies of individual DNA-wrapped SWCNTs by their end-functionalization with two partly complementary (vide infra) azido-modified single strands of DNA. The strands can hybridize to form a partial duplex under neutral pH conditions, thus forming SWCNT junctions. The formed junctions were disassembled by changing the pH of the solution from 7 to 5, via the formation of a more stable i-motif structure at acidic pH, hence destabilizing the DNA partial duplex linking the nanotubes. The individual SWCNTs were then subjected to neutral pH, to restore the DNA duplex junctions, thus demonstrating the reversibility of the system. Additionally, we extended the study demonstrating the construction of dynamic SWCNT junctions that operate via the strand-displacement mechanism. The approaches developed in this study allowed us to obtain reconfigurable end-to-end SWCNT junctions, as indicated by morphological

analysis [atomic force microscopy (AFM)] and further supported by time-dependent fluorescence characterizations. The ability to switch the coupling between single SWCNT segments, forming individual junctions, is of great importance for their future implementation in nano- and molecular-electronic smart systems and devices.[13,33–35]

4.2 End functionalization of CNT with DNA

HiPco SWCNTs were dispersed as-purchased in aqueous solution via DNA (single-stranded) wrapping[36,37] [see **section 4.4**]. The noncovalent wrapping of DNA around the nanotubes allows both the dispersion of the carbon nanotubes in biocompatible aqueous solutions and the protection of their sidewalls, leaving the nanotube ends available for further functionalization.[1,2,9,10]

The solution containing the DNA-wrapped SWCNTs was mixed with methanol at a 1:20 water-methanol final ratio (v/v); this solution was divided into two aliquots, and while DNA sequence (1) was added to the first aliquot, DNA sequence (2) was added to the second one (all DNA sequences used in this study are listed in ***Table 4-1*** in **section 4.4**). DNA sequences (1) and (2) are 5′-azido-modified oligonucleotide strands that include in their sequences a cytosine-rich (C-rich) or guanine-rich (G-rich) domain, respectively, that are partially complementary to one another. In order to covalently functionalize the ends of the nanotubes with DNA, the two solutions were UV-irradiated with a medium pressure immersion mercury lamp (emitting predominantly at 365 nm, Photochemical Reactors Ltd) to promote the formation of reactive nitrene groups, which in proximity of the free-SWCNT-tips form aziridine photoadducts by a cycloaddition reaction[38–40] (***Figure 4-1***). After centrifugal filtration to remove the unreacted excess of (1) and (2) and subsequent re-dispersion of the modified nanotubes

in aqueous solution, (1)-functionalized SWCNTs, A1, and (2)-functionalized SWCNTs, A2, were obtained. This functionalization procedure generates SWCNTs that are covalently and region-specifically linked to the DNA strands: specifically, the SWCNTs carry single DNA molecules at the nanotube ends.[2]

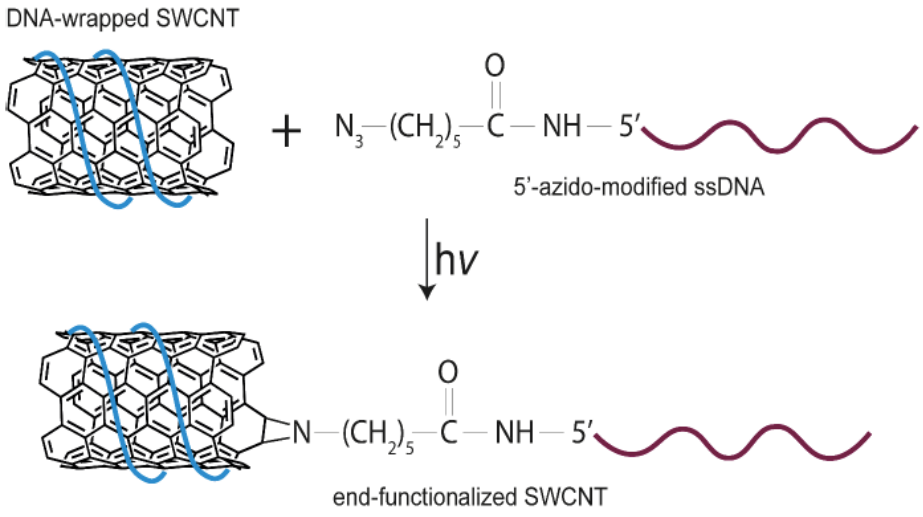

Figure 4-1. *End functionalization of DNA-wrapped SWCNT. The DNA-CNT solutions were UV-irradiated for 10 min with a 400W medium pressure immersion mercury lamp (emitting predominantly at 365 nm, Photochemical Reactors Ltd).*

To quantify the amount of azido-DNA that reacted with A1 and A2, the concentration of DNA in the filtered solutions was estimated by spectrophotometry: absorbance readings were taken at 260 nm. The initial concentration of either (1) and (2) before UV irradiation was 2 μM, whereas the concentration of the removed, unreacted DNA in the filtered solution was found to be equal to 0.19 and 0.17 μM for (1) and (2), respectively (see ***Figure 4-2***). Although most of the DNA seemed to have reacted, a direct quantification of the DNA coupled to the SWCNT ends is, at the moment, still under investigation. As the DNA wrapping protects the nanotube sidewalls, leaving

only the tube ends available for further functionalization, this method provides a facile one-step strategy for the selective functionalization of SWCNT termini.

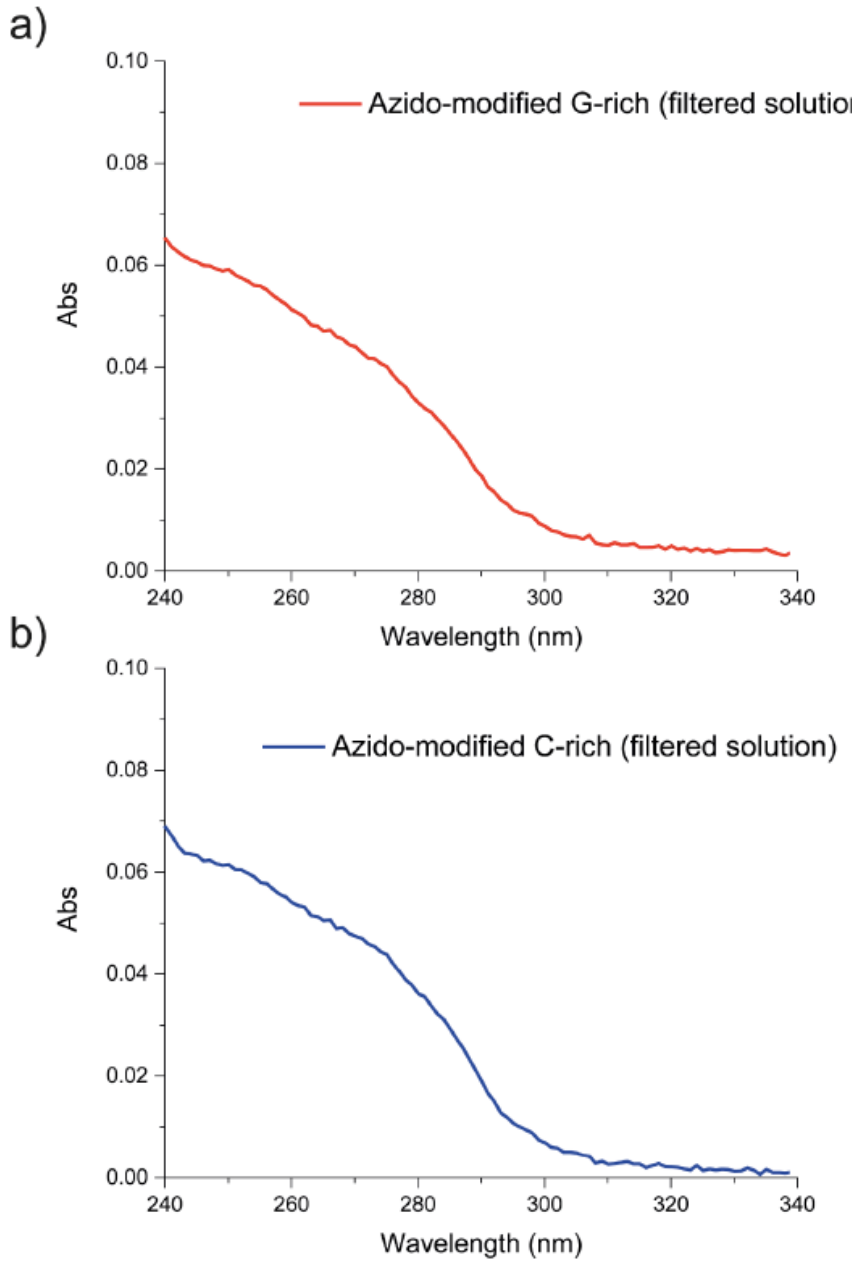

Figure 4-2. *(a) UV absorbance spectrum of azido-modified G-rich DNA solution in the filtered solution. Estimated concentration in the supernatant: 0.17 μM; extinction coefficient: 301,800 L/(mole·cm). (b) UV absorbance spectrum of azido-modified C-rich DNA solution in the filtered solution. Estimated concentration in the supernatant: 0.17 μM; extinction coefficient: 285,000 L/(mole·cm).*

4.3 DNA-powered CNT junction assembly/disassembly

4.3.1 Junction labelling

The aforementioned A1 and A2 were then employed as the building blocks for the formation of DNA-linked SWCNT junctions. In particular, (1) and (2) can hybridize at neutral pH forming a partial DNA duplex (calculated T_m = 34 °C). In order to direct the assembly of SWCNTs junctions, A1 and A2 were mixed with equal amounts at pH = 7 in a buffer solution [containing 2 mM 3-(N-morpholino)propanesulfonic acid (MOPS) and 400 mM NaCl]; this leads to junction formation via DNA hybridization that results in the duplex (1)/(2) as shown in ***Figure 4-3***.

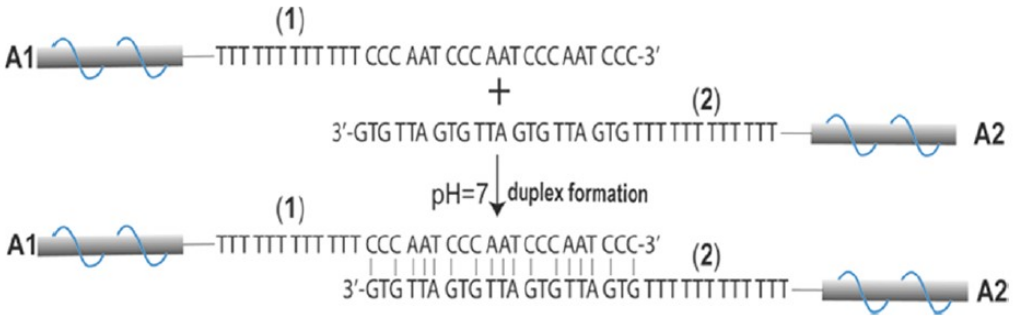

Figure 4-3. *SWCNT junction formation.*

Both (1) and (2) contain different domains: a domain that forms the DNA partial duplex (1)/(2) and a thymine-rich region. By mixing the so-formed junctions with a biotin-modified adenine-rich (3) DNA sequence, which is complementary to the thymine-region, we could introduce biotin functionalities at the site of the junction formation. The presence of the biotin between the two SWCNT segments in the junctions was then exploited to label the junction site via the addition of streptavidin that strongly and

specifically interacts with biotin (for additional details on the biotin-labeled junction in the presence of streptavidin, see ***Figure 4-4***). This allowed us to then unequivocally locate the site of the junction formation via AFM imaging, hence, further demonstrating the successful linking of A1 and A2. For this purpose, we drop-cast low-coverage films of SWCNTs at pH = 7 on mica, then drop-cast a 500 nM streptavidin solution, and after washing off the streptavidin excess with distilled water, the substrate was imaged by AFM. ***Figure 4-5*** shows the representative AFM images and respective height profiles of the streptavidin-labeled SWCNT junctions, corresponding to the expected nanotubes and protein sizes: this confirms junction formation. It is worth mentioning that although at the junction point two biotin-labeled oligonucleotides are hybridized, it is assumed that only one streptavidin can bind to the site because of steric hindrance; this assumption is confirmed by AFM analysis of the junctions (see ***Figure 4-5***). Note that both straight and bent junctions are presented in our AFM images. This is likely to be an effect of the physisorption of the SWCNT junctions from solution to surfaces, as previously observed by us and others.[1,16]

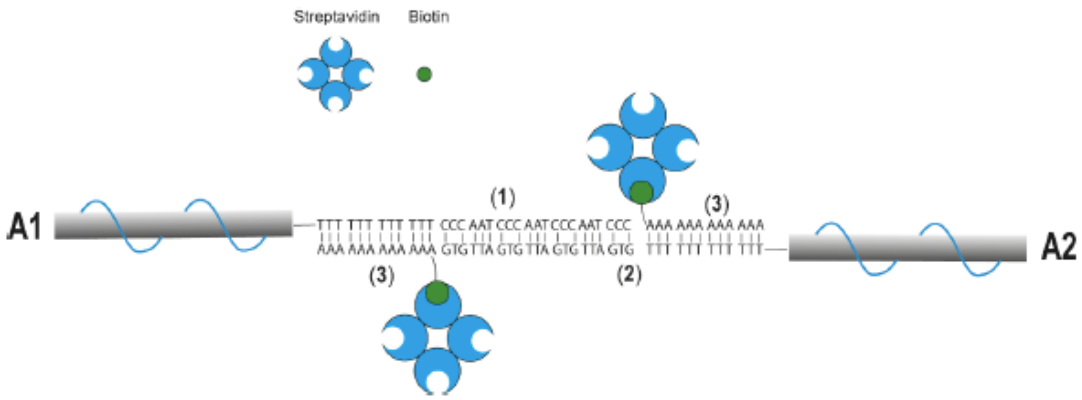

Figure 4-4. *In situ Streptavidin-Biotin labelling of the junction.*

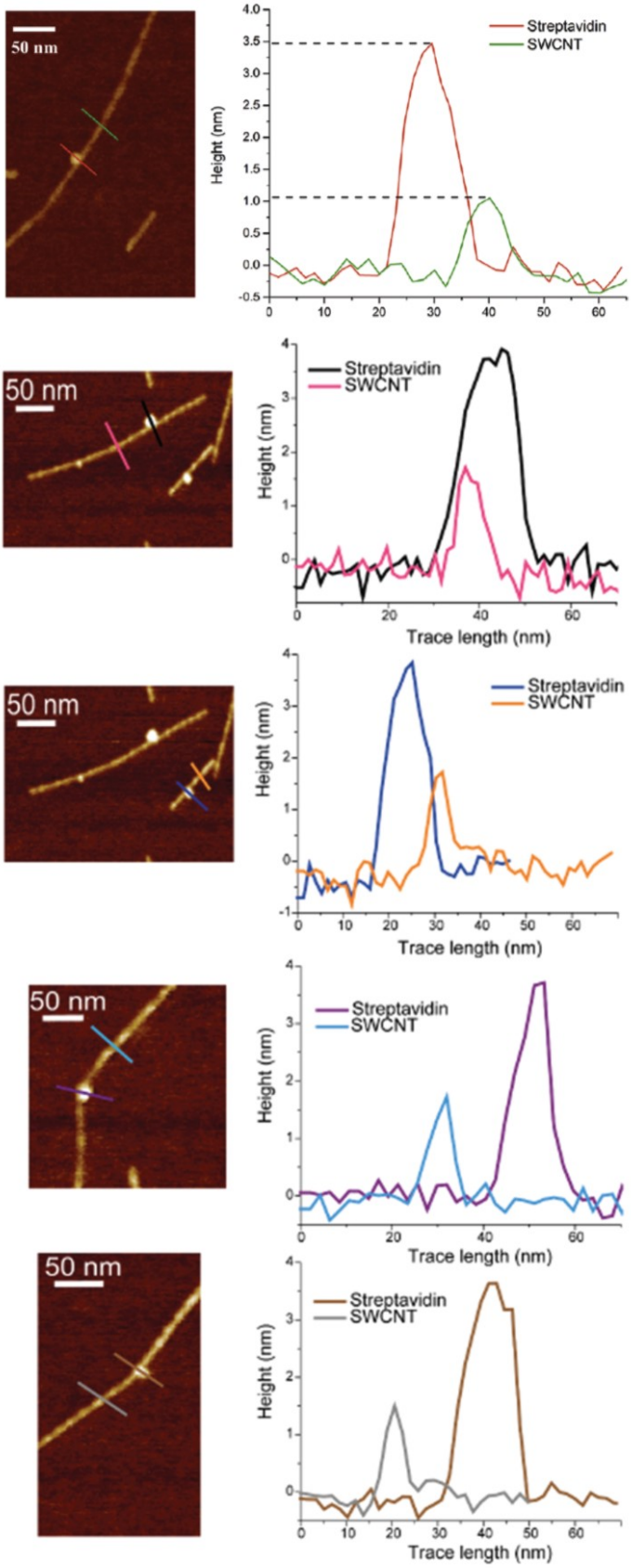

Figure 4-5. *AFM characterizations of the Streptavidin-Biotin labelled SWCNT junctions.*

4.3.2 Real-time monitoring of stimuli-responsivity

4.3.2.1 pH as the stimulus

At neutral pH, (1) is available for duplex formation and consequently can hybridize with its complementary (2), forming nanotube junctions. Conversely, when the pH of the solution is acidic (pH = 5), (1) forms an energetically-favorable intercalated motif structure (i-motif),[31,41,42] leading to the disassembly of the DNA-linked SWCNT junctions. This behavior can then be exploited for the pH-controlled assembly/disassembly of SWCNT junctions.

To further prove the successful pH-controlled assembly/disassembly of SWCNT junctions, time-dependent fluorescence analysis of the nanostructures was performed. We mixed A1 and A2 in equal amounts at pH = 7 in a solution containing 2 mM MOPS and 400 mM NaCl, as previously described, to form the junctions and added a quencher (Q)-modified DNA sequence (4), which is complementary to the thymine-domain and binds at the junction site. We then added to this solution a cyanine 3 (Cy3)-modified DNA (5), which is partially complementary to (2). ***Figure 4-6*** shows the pH-controlled mechanism of the SWCNT−DNA junction assembly/ disassembly, in the presence of the quencher and fluorophore labels (4) and (5), respectively.

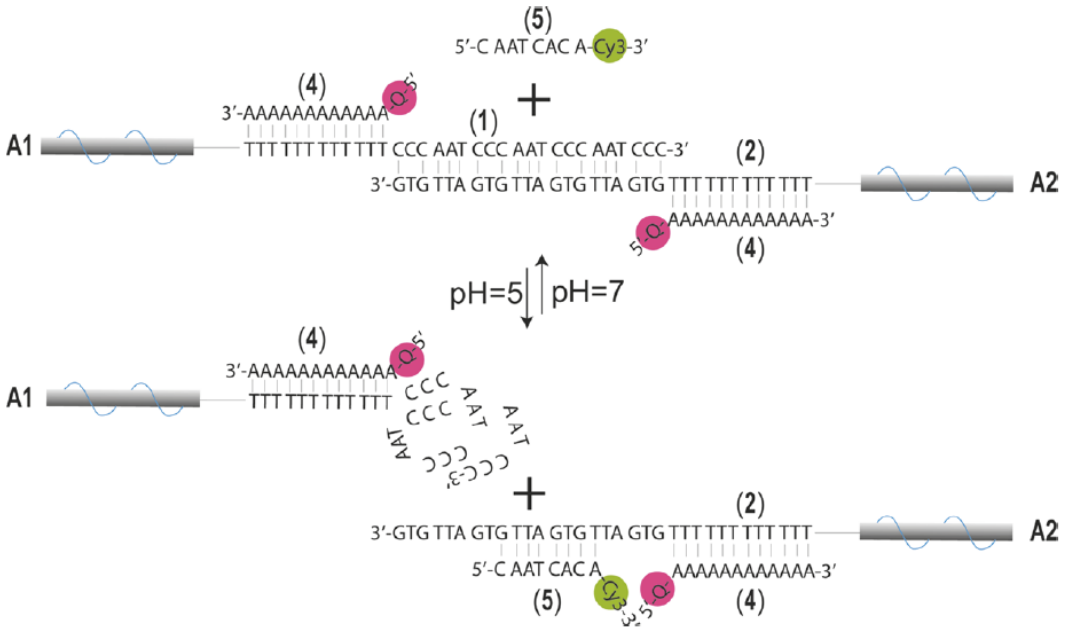

Figure 4-6. *Scheme of the dynamic junction assembly/disassembly exploiting pH as the stimulus.*

At pH = 7, (5) is free in solution as (2) is not available due to the junction formation via a more stable (1)/(2) duplex structure; when the pH is decreased from 7 to 5, the disassembly of the junction frees (2) in A2, allowing it to hybridize with (5); this in turn results in the quenching of Cy3 because of its proximity to Q on the terminal ends of A2 (see ***Figure 4-6***). The sequences (4) and (5) were designed to position the Q and Cy3 functionalities at a specific separating distance. From geometric considerations of the DNA molecule, we calculated the distance separating Cy3 and the quencher in the duplex structure (2)/(4)/(5) to be equal to 1.7 nm. This results in the efficient quenching of the fluorescence emission at pH = 7, whereas at pH = 5, the large separating distance between Cy3 and the quencher in the single-strand (5) and duplex (2)/(4) results in the inefficient quenching of the fluorophore. We monitored this change in fluorescence in real time, by varying the pH from 7 to 5 in multiple cycles, and recording the

fluorescence emission of Cy3, as shown in ***Figure 4-7***. This allowed us to confirm the reversible pH-dependent assembly/disassembly of the DNA−SWCNTs. It should be noted that the incremental drift in the fluorescence intensity is likely due to the slow aggregation and precipitation of the SWCNTs; this results in a time-dependent proportional decrease in optical density of the mixture and increased collected emission from the fluorophore. Additionally, small deviations are observed due to the manual operation and by small volume additions of concentrated acid/base. To prove that the quenching effect of the carbon nanotubes on the fluorophores is not significant, we performed the same experiments in the absence of SWCNTs (see ***Figures 4-7***).

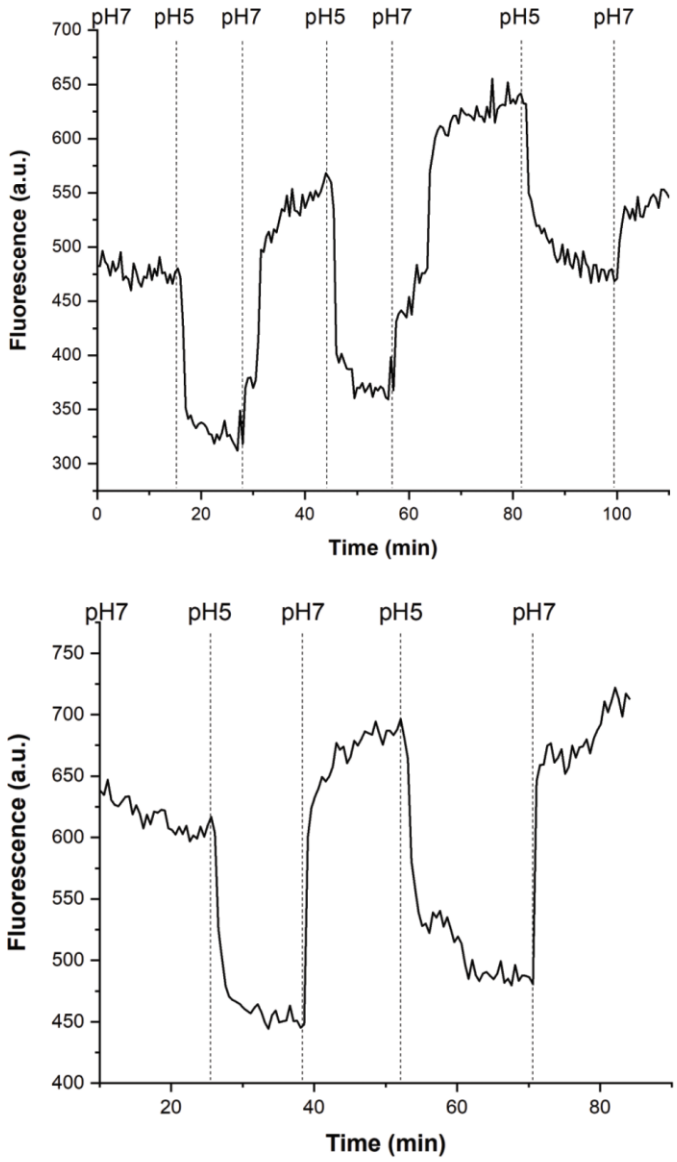

Figure 4-7. *Top: Real-time fluorescence changes of the pH-controlled DNA−SWCNT junctions. The fluorescence emission of Cy3 is monitored while reversibly varying the pH between 7 and 5 in multiple cycles. High fluorescence emission corresponds to the formed DNA− SWCNT junctions at pH = 7 [where Cy3-modified strand (5) is free in solution], whereas low fluorescence emission corresponds to the separation of the DNA−SWCNT junctions at pH = 5 [where the Cy3-functionalized (5) is quenched by the quencher-modified strand (4)]. Bottom: Real-time fluorescence changes of the pH-switch system in absence of SWCNTs. The fluorescence emission of Cy3 is monitored while reversibly varying the pH between 7 and 5, in multiple cycles.*

4.3.2.2 DNA as the stimulus

In order to explore the versatility of the approach developed here, we extended our studies by inducing the disassembly of SWCNT junctions with a different stimulus. A fuel DNA sequence (SD1), a DNA sequence that activates the disassembly process, was designed to be capable of destabilizing the DNA duplex forming the SWCNT junction, via strand-displacement.[28,43] Upon addition of the designed fuel DNA strand (SD1) to the DNA-linked SWCNT junctions solution at neutral pH, strand (2) is displaced from duplex (1)/(2) by (SD1), resulting in a new duplex (1)/(SD1) and free strand (2). To make this new system reversible, we introduced an anti-fuel DNA strand (SD2), a DNA sequence that reactivates the assembly process, which promotes the recovery of the assembly of A1 and A2 by a second strand-displacement event (***Figure 4-8***). This was confirmed by time-dependent fluorescence measurements.

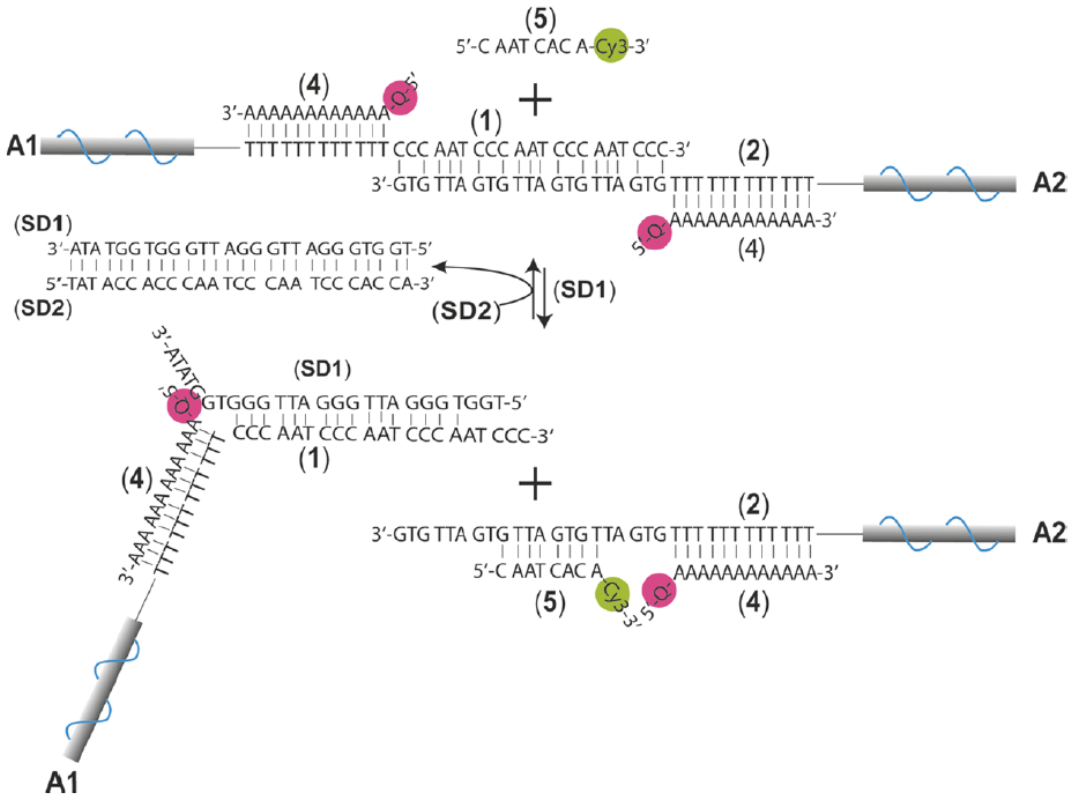

Figure 4-8. *Scheme of the dynamic junction assembly/disassembly exploiting DNA as the stimulus.*

Quencher-labeled A1 and A2 were mixed together at pH = 7 with (5); at neutral pH, A1 and A2 form SWCNT junctions and the solution is characterized by a high fluorescence intensity because of the free Cy3-modified DNA (5) in solution. Upon addition of (SD1), the junction is separated and (5) binds to (2), resulting in the proximity of Cy3 to Q and the low emission of fluorescence of Cy3. The following addition of (SD2) displaces (SD1) from the duplex (1)/(SD1), resulting in the new duplex (SD1)/(SD2), and the restoration of the original SWCNT junction via the duplex (1)/(2). The concomitant release in solution of the fluorophore-modified strand (5) recovers the original high-level fluorescence emission from Cy3 because of the large spatial separation from the quencher unit. Upon cyclic sequential addition in solution

of (SD1) and (SD2) strands, the reversible assembly and disassembly of the SWCNT junctions is demonstrated by the low and high level of emission from Cy3-modified strand (5). Although a high level of fluorescence characterizes the free fluorophore (formed junction), the proximity of the fluorophore-quencher pair functionalities in the separated junctions is characterized by low fluorescence. ***Figure 4-9*** shows the time-dependent fluorescence changes of the strand-displacement controlled SWCNT junction assembly/disassembly system, in the presence of the quencher and fluorophore labels (4) and (5). To prove that the quenching effect of the carbon nanotubes on the fluorophores is not significant, we performed the same experiments in the absence of SWCNTs (see ***Figures 4-9***).

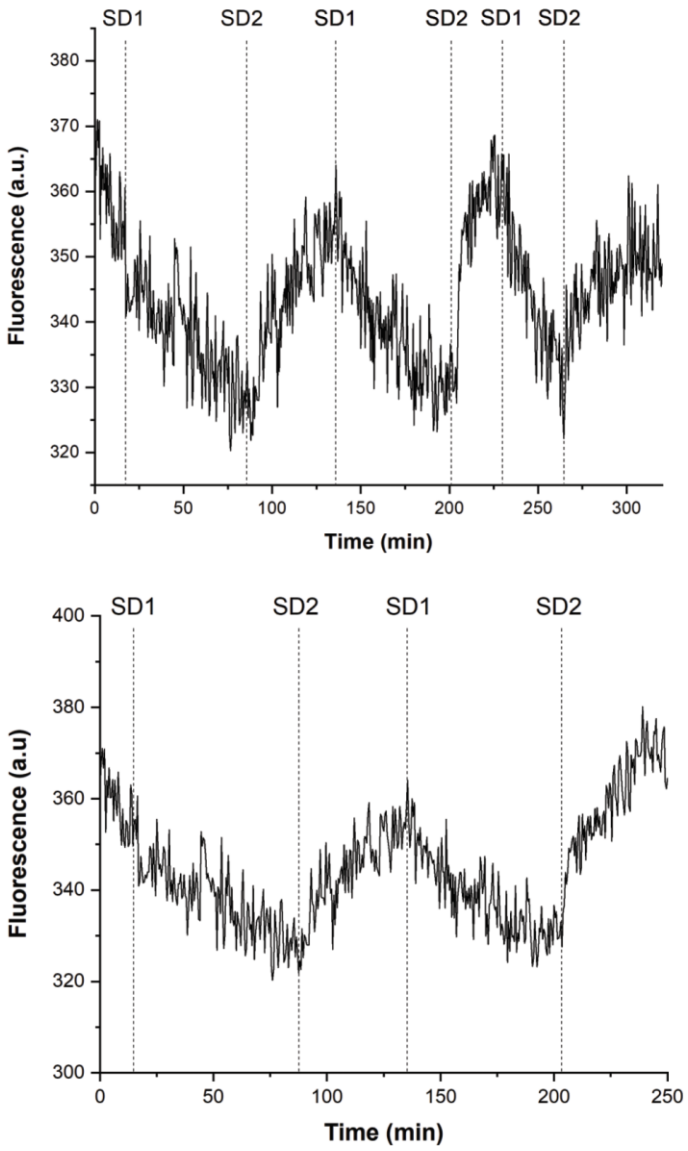

Figure 4-9. *Top: Real-time fluorescence changes of the strand-displacement controlled DNA−SWCNT junctions in the presence of quencher modified oligonucleotide (4) and Cy3-modified strand (5). Addition of (SD1) and (SD2) strands, in multiple cycles, results in the separation and recovery of the junction assembly, respectively. High fluorescence emission corresponds to the free Cy3-modified strand (5) in solution; whereas low fluorescence emission corresponds to the quenching of Cy3-(5) upon separation of the DNA−SWCNT junctions. Bottom: Real-time fluorescence changes of the strand-displacement system in absence of SWCNTs. The fluorescence emission of Cy3 is monitored while reversibly adding (SD1) and (SD2) strands, in multiple cycles.*

4.3.3 Length analysis of junction assembly/disassembly

To further prove the successful stimuli driven SWNCT junction assembly/disassembly, we carried out length analysis based on the AFM images of SWCNTs under varied conditions.

The pristine DNA-wrapped SWCNTs had an average length of 131 ± 72 nm as determined by AFM analysis (see Figure 10 for a representative image). The uncertainty affecting the measured lengths of the nanotube nanostructures was estimated by the standard deviation (SD) values associated with the length distributions, as they appear in the AFM analysis; this is reported for all distributions (average length ± SD).

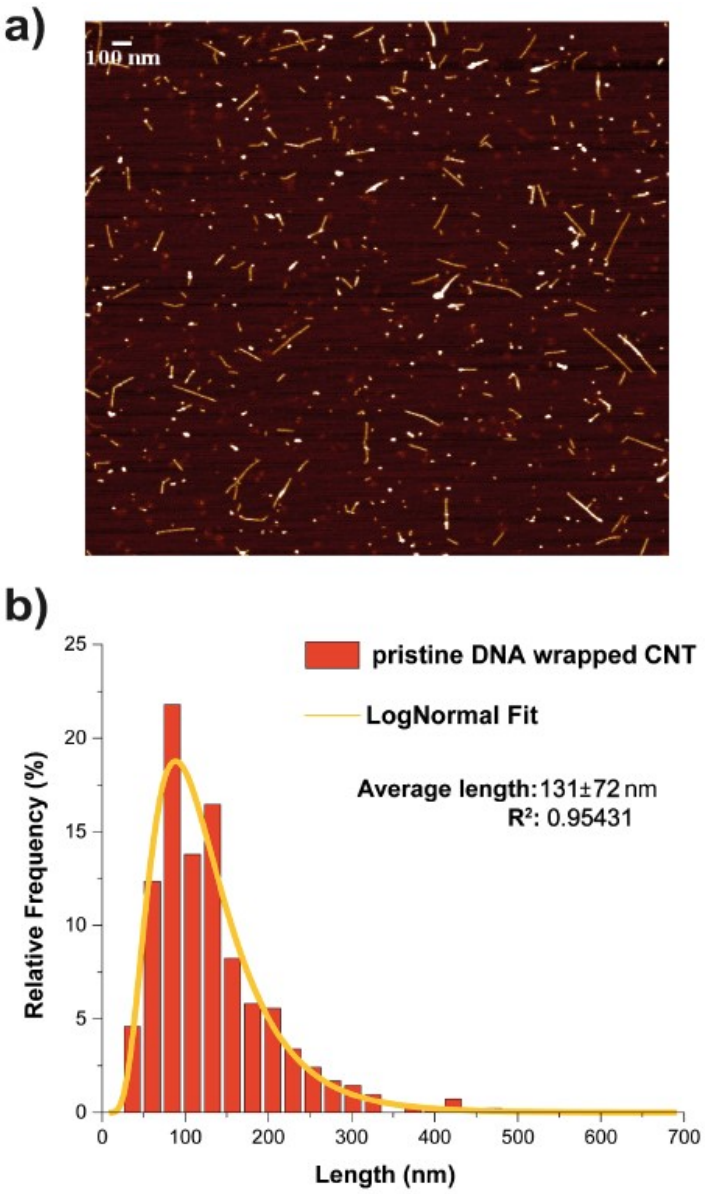

Figure 4-10. *(a) AFM topographical image and (b) length distribution with fitted curve of pristine DNA-wrapped SWCNTs (data size: 413 counts).*

To demonstrate the assembly of the SWCNT junctions at pH = 7, dilute solutions were cast on muscovite mica and the substrate surfaces were imaged with AFM. We performed a statistical analysis of the tube length; the average length of the SWCNT junctions after 1 h incubation of A1 with A2 was found to be 184 ± 97 nm (see ***Figure 4-11*** for a representative AFM image and the related lengths distribution). In line with

our previous SWCNT length analysis of junction formation,[1,2] the increase in the SWCNTs average length from 131 ± 72 (***Figure 4-10***) to 184 ± 97 nm (***Figure 4-11***) indicates the formation of the junctions at pH = 7.

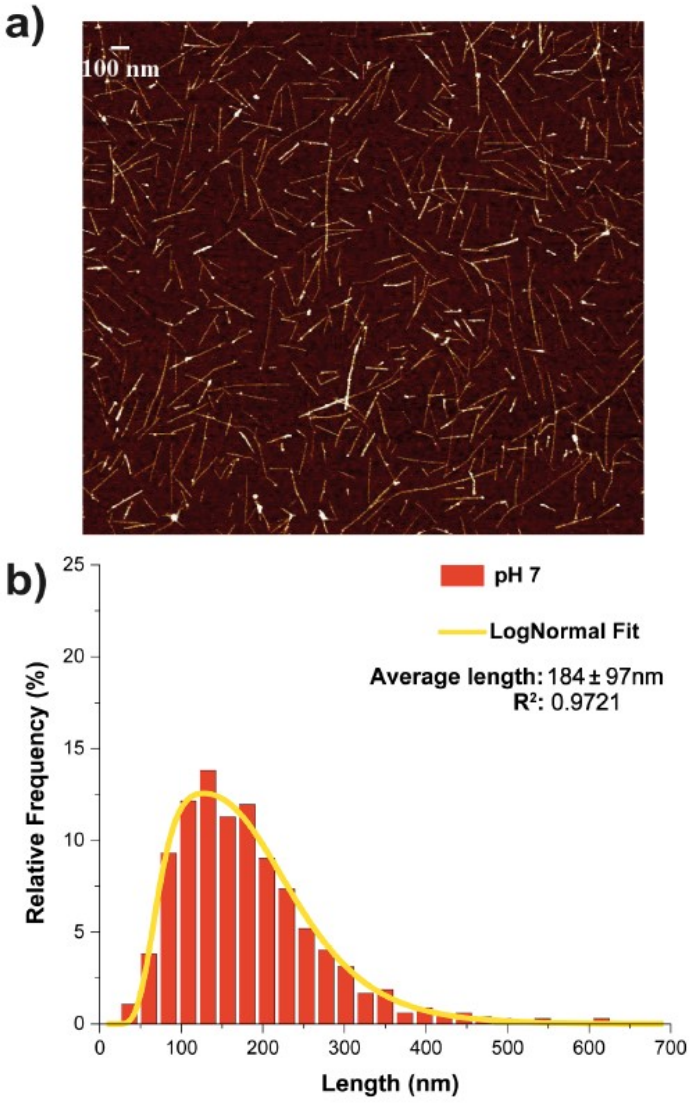

Figure 4-11. *(a) AFM image and (b) length distribution with fitted curve of assembled SWCNT at pH 7 (data size: 500 counts).*

To demonstrate the disassembly of the SWCNT junctions as a function of pH, we cast acidic solutions (pH = 5) on mica and imaged the substrates with AFM. The average length of the SWCNT junctions after changing the pH of the solution from 7 to 5 was

found to decrease to 148 ± 80 nm (see ***Figure 4-12***), suggesting the separation of the jointed SWCNTs upon reducing the pH from 7 to 5.

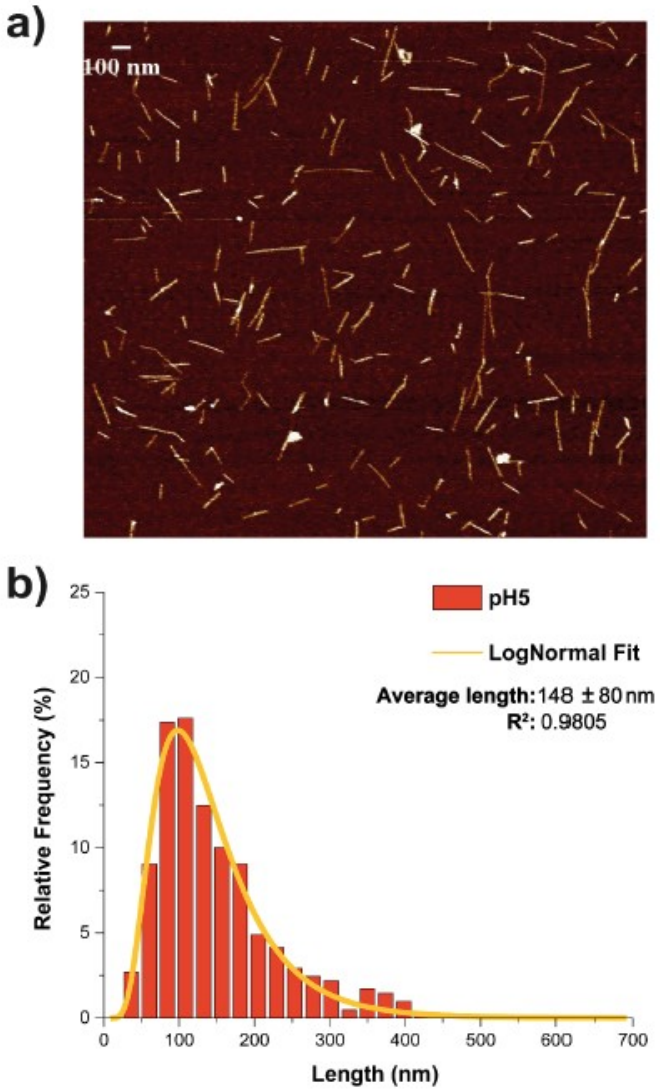

Figure 4-12. *(a) AFM image and (b) length distribution with fitted curve of disassembled SWCNT after acidification of the solution to pH = 5 (data size: 409 counts).*

Additionally, to confirm it is these specific DNA sequences exploited here grant the system the selective responsivity to pH, we assembled nanotube junctions employing a fully-complementary double-stranded DNA (dsDNA) as the linker, which is not

structurally responsive to changes in pH values: ***Figure 4-13*** shows how the average length of the junctions does not vary from pH = 7 to pH = 5.

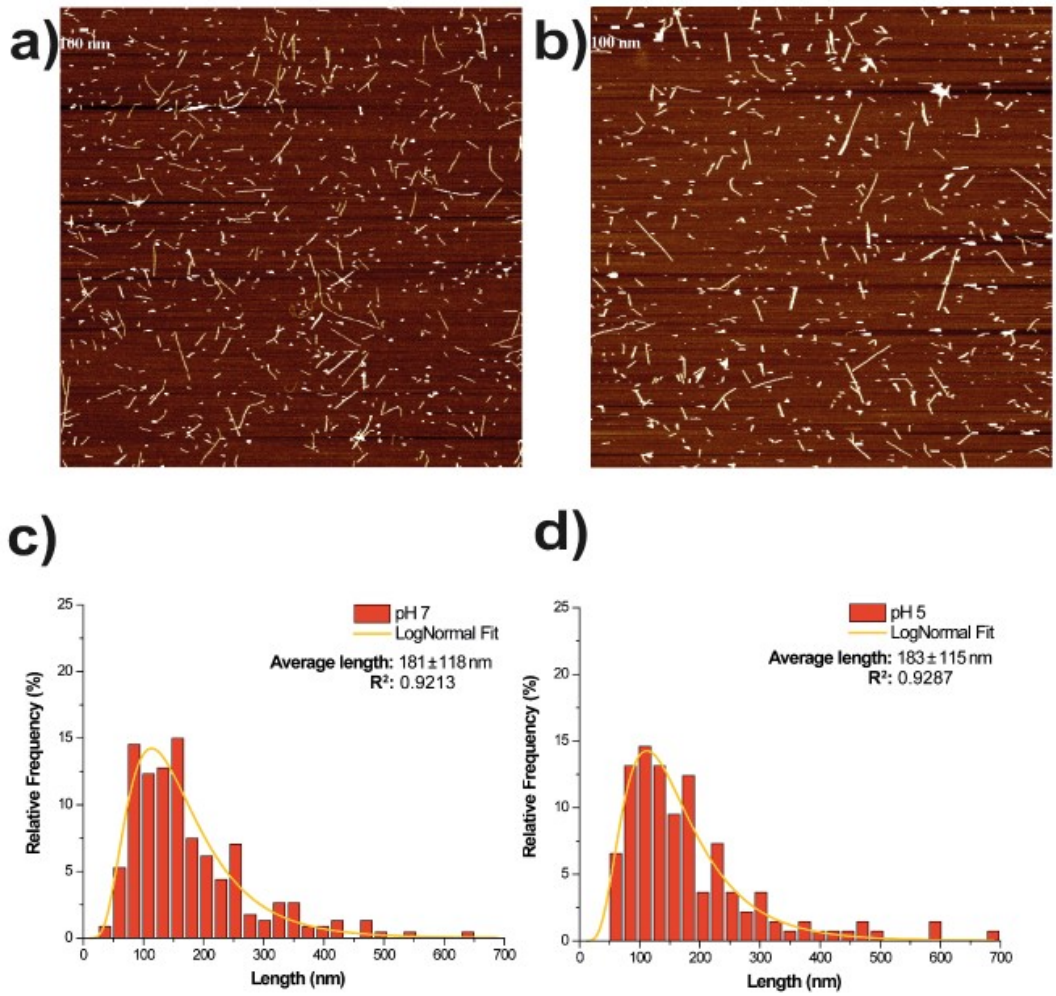

Figure 4-13. *AFM images of DNA-linked SWCNTs junctions at pH = 7 (a) and pH = 5 (b). Length distribution with fitted curves of assembled SWCNTs (c) at pH 7 (data size: 228 counts) and (d) after acidification of the solution to pH = 5 (data size: 137 counts).*

As is previously mentioned in section 4.3.2.2, we also introduced a specific DNA strand as the stimulus to activate the junction disassembly. Upon addition of the designed fuel DNA strand (SD1) to the DNA-linked SWCNT junctions solution at neutral pH, strand

(2) is displaced from duplex (1)/(2) by (SD1), resulting in a new duplex (1)/(SD1) and free strand (2). AFM images of disassembled SWCNT junctions by strand-displacement were taken after the addition of (SD1) to the SWCNT junctions: the disassembly was confirmed by statistical analysis of the average tube length, which was found to be 141 ± 79 nm (see ***Figure 4-14***), in accordance with the results obtained for the disassembled junctions at acidic pH (148 ± 80 nm).

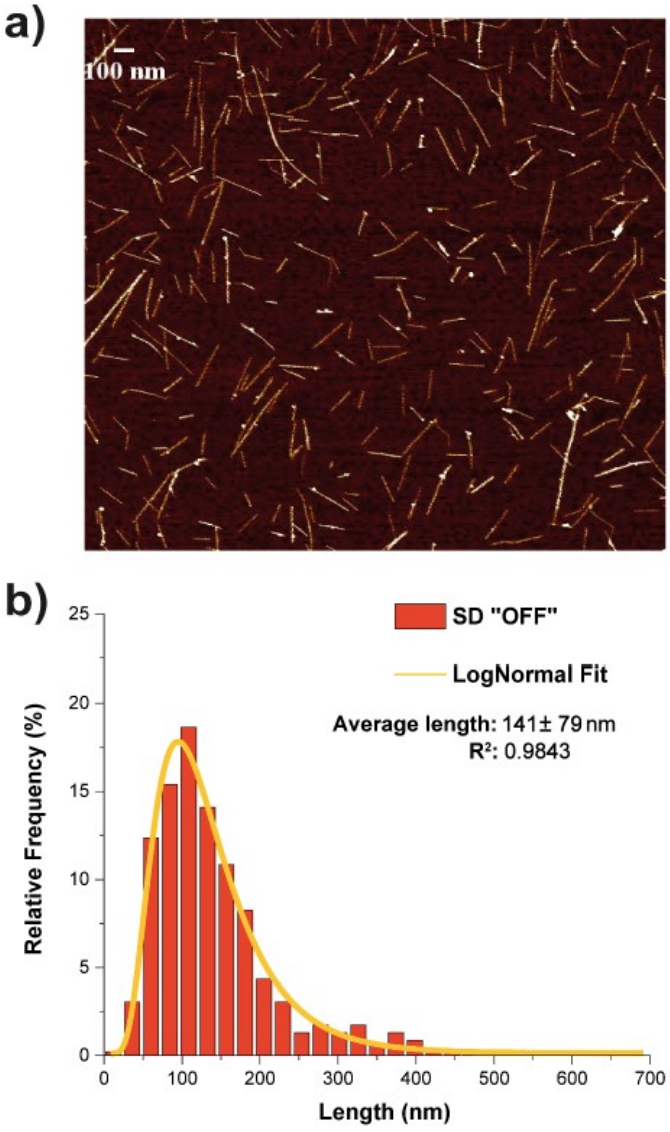

Figure 4-14. *(a) AFM image and (b) length distribution with fitted curve of disassembled SWCNT upon addition of (SD1) to SWCNT junction solution (data size: 461 counts).*

4.4 Conclusions

In summary, we have presented a strategy for the controlled and reversible assembly of end-to-end SWCNT junctions under different stimuli. This was achieved by exploiting the molecular recognition of DNA complementary sequences employed here as linkers. SWCNTs were covalently end-functionalized with azido-modified ssDNA in a one-pot reaction, under UV light. SWCNTs assembly was driven by the hybridization between complementary DNA strands at the nanotube termini at neutral pH. Employing at the junction site a C-rich domain, the reversible assembly/disassembly of SWCNT junctions was controlled by varying the pH; this was confirmed by both AFM imaging and real-time fluorescence investigations. Additionally, we designed the system for the controlled and reversible assembly/disassembly of SWCNT junctions via strand-displacement. This further demonstrates the versatility of the approach presented here, for the dynamic tuning of SWCNT junction formation via different stimuli. The strategy presented in this report is of interest for the fabrication of solution-processable and stimuli-responsive CNT-based systems, also of higher complexity. This holds great potential for the development of optoelectronic devices employing G-rich DNAs as active components, and sensing platforms via the use of oligonucleotide aptamer sequences, where the CNTs can be employed as switchable nanoelectrodes.[13,33,44,45]

4.5 Materials and methods

All DNA strands were purchased from IDT (Integrated DNA Technologies, Inc.). DNA strands were processed by desalted purification and functionalized DNA strands were processed by HPLC purification.

Table 4-1. **DNA strands (all sequences are reported from 5' to 3')**

(1)	Azide-TTT TTT TTT TTT CCC AAT CCC AAT CCC AAT CCC
(1')	Azide-TTT TTT TTT TTT CAC AAT CAC AAT CAC AAT CAC AAA AAA AAA
(2)	Azide-TTT TTT TTT TTT GT GAT TGT GAT TGT GAT TGT G
(3)	Biotin-AAA AAA AAA AAA
(4)	IowaBlackFQ-AAA AAA AAA AAA
(5)	CAATCACA-Cy3
(SD1)	TGG TGG GAT TGG GAT TGG GTG GTA TA
(SD2)	TAT ACC ACC CAA TCC CAA TCC CAC CA
$(GT)_{20}$	GTGT GTGT GTGT GTGT GTGT GTGT GTGT GTGT GTGT GTGT

Atomic Force Microscopy (AFM)

AFM analysis of the samples was carried out on a Bruker Dimension Icon in PeakForce Tapping mode with ScanAsyst Air tips from Bruker.

SWCNT length analysis

Length distributions were obtained by image-J 1.51j8 software. Histograms and Lognormal curve fitting were generated by OriginPro 2015 (V b9.2.257).

SWCNT dispersion

SWCNTs were dispersed in water by DNA wrapping according to published procedures1. Generally, 1 mL solution containing HiPco nanotube (1 mg/mL; Carbon

Nanotechnologies Inc.), DNA oligomer (GT)20 (1 mg/mL) and NaCl (0.1 M, Fisher Scientific) was sonicated in an ice water bath for 90 min at a power of 3W (Sonics, VC130PB). After sonication, the solution was divided into 0.1 mL aliquots, centrifuged for 90 min at 15,000 g to remove insoluble materials, and the supernatant collected. The dispersion process (DNA wrapping) not only allows the dispersion of SWCNTs in solution, but it also protects the sidewall of the nanotubes and leaves the open ends available for further direct functionalization. Then, the solution was drop-cast on freshly cleaved muscovite mica disc (Agar Scientific), pre-treated with $MgCl_2$ solution (1 M, Sigma Aldrich), incubated for 10 min and characterized by AFM. A statistical analysis of the DNA-wrapped SWCNTs length gives an average tube length of 131 ± 72 nm (***Figure 4-10***).

SWCNT end-functionalization

To functionalize SWCNTs, 50 μL of DNA-wrapped SWCNTs were mixed with methanol (at a final volume of 1 mL) and divided into two equal aliquots. The first aliquot was mixed with (1) (at a final concentration of 2 μM), the second with (2) (at a final concentration of 2 μM), and then both UV-irradiated for 10 min with a 400W medium pressure immersion mercury lamp (emitting predominantly at 365 nm, Photochemical Reactors Ltd). After irradiation, free DNA in the samples was removed by 3 min centrifugation at 15,000 g with centrifugal filters (Amicon Ultra 100 kDa, Millipore). The centrifugation process was repeated three times and finally the samples were re-dispersed in 100 μL NaCl (0.1 M). After centrifugal filtration and re-dispersion, (1) end-functionalized SWCNTs (A1) and (2) end-functionalized SWCNTs (A2) were obtained.

SWCNT junction formation

Samples (150 μL in volume) at pH = 7 were prepared as follows: 10 μL of A1 and 10 μL of A2 were mixed in a buffered solution (2 mM MOPS Sigma Aldrich, 400 mM NaCl, pH = 7) and incubated for 1 hour at room temperature. 10 μL of the solution was drop cast on freshly cleaved muscovite mica disc, pre-treated with 1 M $MgCl_2$ solution, incubated for 10 min and characterized by AFM. The statistical analysis of SWCNTs after junction formation gives an average length of 184 ± 97 nm. By comparing this with the average length of pristine DNA-wrapped SWCNTs (131 ± 72 nm), the increase in average length is about 40%, suggesting the formation of end-to-end SWCNT junctions.

SWCNT junction labelling

10 μL of the SWCNT junction solution and (3) (at a final concentration of 100 nM) were mixed and incubated for 1 hour at room temperature. After, the solution was drop-cast on mica (Agar Scientific) pre-treated with $MgCl_2$ solution and incubated for 10 min. After, 10 μL of streptavidin solution (500 nM, Invitrogen™) was deposited on the mica substrate, incubated for 10 minutes, rinsed with MilliQ® water and blown-dried with compressed air.

pH-controlled disassembly

50 μL of the SWCNT junction solution was acidified (pH = 5) by addition of acetic acid (10% vol/vol, VWR Chemicals) and incubated for 1 hour at room temperature. Then, 10 μL of the solution was drop-cast on freshly cleaved discs of pre-treated mica, incubated for 10 min, rinsed with MilliQ® water and blown dry with compressed air.

Control experiment

To confirm the selectivity of the pH system, as a control experiment, we designed a new DNA duplex, bridging the SWCNTs, which is not affected by changing in pH. In this regard HiPco SWCNTs were covalently functionalized at their terminal ends with 5'-azido modified oligonucleotide strand (1'), complementary to (2), as previously described. As (1') and (2) can hybridize forming a DNA duplex, (1')-functionalized SWCNTs, A1', and A2 were employed as constituents for the formation of new DNA-linked SWCNT junctions. A1' and A2 were then mixed in equal amounts in a solution containing 2 mM MOPS and 400 mM NaCl and incubated for 1 hour. To demonstrate the assembly of the new SWCNT junctions is not affected by pH, we imaged the system at pH = 7 and at pH = 5 with AFM, and performed a statistical analysis of the average tube length. The average length of the SWCNTs junctions was found to be 181 ± 118 nm at pH = 7 and 183 ± 115 nm at pH = 5 respectively (see ***Figure 4-13*** for representative AFM images and the related lengths distributions). This allows us to prove the specificity of the pH system, where the tube average length decreases when the pH of the solution is changed from 7 to 5.

SWCNT junction disassembly via strand-displacement

50 µL of SWCNT junction solution was mixed with 2 µL of (SD1) (at a final concentration of 100 µM) and incubated for 1 hour at room temperature. Then, 10 µL of the solution was drop-cast on freshly cleaved discs of pretreated mica, incubated for 10 min, rinsed with MilliQ® water and blown dry with compressed air.

Time-dependent fluorescence investigation of pH-switch system

Samples (150 µL in volume) for time-dependent fluorescence experiments were prepared as follows: 10 µL of A1 and 10 µL of A2 were mixed with (4) (at a final concentration of 700 nM) and (5) (at a final concentration of 100 nM) in a buffered solution (2 mM MOPS, 300 mM NaCl, pH = 7), and incubated for 1 hour at room temperature. Then, the solution was transferred into a plastic cuvette, the fluorophore (Cy3) excited at 520 nm and the emission signal collected at 562 nm. The temperature was set and maintained at 20°C throughout the whole analysis. The pH of the solution was switched between 5 and 7 by sequential additions of 0.6 µL acetic acid (10% vol/vol) or 0.75 µL of ammonia solution (1 M, Sigma-Aldrich).

Time-dependent fluorescence investigation of strand-displacement system

Samples (150 µL in volume) for time-dependent fluorescence experiments were prepared as follows: 10 µL of A1 and 10 µL of A2 were mixed with (4) (at a final concentration of 700 nM) and (5) (at a final concentration of 100 nM) in a buffered solution (2 mM MOPS, 400 mM NaCl, pH= 7), and incubated for 1 hour at room temperature. As for the pH-switch system, the fluorophore (Cy3) was excited at 520 nm into a plastic cuvette and the emission signal collected at 562 nm. The strand-displacement was carried out by sequential additions of (SD1) or (SD2) at a final concentration of 2 µM.

Time-dependent fluorescence investigation of pH-switch system in the absence of SWCNTs

Samples (150 µL in volume) for time-dependent fluorescence experiments were prepared as follows: (1) and (2) (both at final concentration of 30 nM) were mixed with (4) (at a final concentration of 700 nM) and (5) (at a final concentration of 100 nM) in

a buffered solution (2 mM MOPS, 300 mM NaCl, pH = 7), and incubated for 1 hour at room temperature. Then, the solution was transferred into a plastic cuvette, the fluorophore (Cy3) excited at 520 nm and the emission signal collected at 562 nm. The temperature was set and maintained at 20°C throughout the whole analysis. The pH of the solution was switched between 5 and 7 by sequential additions of 0.6 μL acetic acid (10% vol/vol) or 0.75 μL of ammonia solution (1 M, Sigma-Aldrich).

Time-dependent fluorescence investigation of strand-displacement system in the absence of SWCNTs

Samples (150 μL in volume) for time-dependent fluorescence experiments were prepared as follows: (1) and (2) (both at final concentration of 30 nM) were mixed with (4) (at a final concentration of 700 nM) and (5) (at a final concentration of 100 nM) in a buffered solution (2 mM MOPS, 400 mM NaCl, pH = 7), and incubated for 1 hour at room temperature. As previously described for the pH-switch system, the fluorophore (Cy3) was excited at 520 nm into a plastic cuvette and the emission signal collected at 562 nm. The strand-displacement was carried out by sequential additions of (SD1) or (SD2) at a final concentration of 2 μM.

4.6 References

1. Palma, M. *et al.* Controlled formation of carbon nanotube junctions via linker-induced assembly in aqueous solution. *J. Am. Chem. Soc.* **135**, 8440–8443 (2013).
2. Zhu, J. *et al.* Solution-Processable Carbon Nanoelectrodes for Single-Molecule Investigations. *J. Am. Chem. Soc.* **138**, 2905–2908 (2016).
3. McMorrow, J., Freeley, M. & Palma, M. DNA-Wrapped Single-Walled Carbon Nanotube Assemblies. *Ind. Eng. Chem. Res.* **56**, 5302–5308 (2017).

4. Zhen, Y., Postma, H. W. C., Balents, L. & Dekker, C. Carbon nanotube intramolecular junctions. *Nature* **402**, 273–276 (1999).

5. Fuhrer, M. S. *et al.* Crossed nanotube junctions. *Science (80-.).* **288**, 494–497 (2000).

6. Park, H. *et al.* High-density integration of carbon nanotubes via chemical self-assembly. *Nat. Nanotechnol.* **7**, 787–791 (2012).

7. Cao, Q. & Rogers, J. A. Ultrathin films of single-walled carbon nanotubes for electronics and sensors: A review of fundamental and applied aspects. *Advanced Materials* **21**, 29–53 (2009).

8. Park, S., Vosguerichian, M. & Bao, Z. A review of fabrication and applications of carbon nanotube film-based flexible electronics. *Nanoscale* **5**, 1727–1752 (2013).

9. Freeley, M. *et al.* Site-Specific One-to-One Click Coupling of Single Proteins to Individual Carbon Nanotubes: A Single-Molecule Approach. *J. Am. Chem. Soc.* **139**, 17834–17840 (2017).

10. Attanzio, A. *et al.* Carbon Nanotube-Quantum Dot Nanohybrids: Coupling with Single-Particle Control in Aqueous Solution. *Small* **13**, (2017).

11. Freeley, M. *et al.* Tuning the Coupling in Single-Molecule Heterostructures: DNA-Programmed and Reconfigurable Carbon Nanotube-Based Nanohybrids. *Adv. Sci.* **5**, (2018).

12. Feldman, A. K., Steigerwald, M. L., Guo, X. & Nuckolls, C. Molecular electronic devices based on single-walled carbon nanotube electrodes. *Acc. Chem. Res.* **41**, 1731–1741 (2008).

13. Guo, X. Single-molecule electrical biosensors based on single-walled carbon nanotubes. *Adv. Mater.* **25**, 3397–3408 (2013).

14. Xiang, D., Wang, X., Jia, C., Lee, T. & Guo, X. Molecular-Scale Electronics: From Concept to Function. *Chem. Rev.* **116**, 4318–4440 (2016).

15. Jin, C., Suenaga, K. & Iijima, S. Plumbing carbon nanotubes. *Nat. Nanotechnol.* **3**, 17–21 (2008).

16. Weizmann, Y., Chenoweth, D. M. & Swager, T. M. Addressable terminally linked

DNA-CNT nanowires. *J. Am. Chem. Soc.* **132**, 14009–14011 (2010).

17. Oruc, B., Celik, S., Hayat Soytas, S. & Unal, H. DNA Directed Self-Assembly of Single Walled Carbon Nanotubes into Three-Way Junction Nanostructures. *ACS Omega* **3**, 4157–4162 (2018).
18. J. Wind, S. *et al.* Integrating DNA with Functional Nanomaterials. *J. Self-Assembly Mol. Electron.* **1**, 177–194 (2013).
19. Xu, X. *et al.* Reconfigurable Carbon Nanotube Multiplexed Sensing Devices. *Nano Lett.* **18**, 4130–4135 (2018).
20. Geier, M. L. *et al.* Solution-processed carbon nanotube thin-film complementary static random access memory. *Nat. Nanotechnol.* **10**, 944–948 (2015).
21. Brady, G. J. *et al.* Quasi-ballistic carbon nanotube array transistors with current density exceeding Si and GaAs. *Sci. Adv.* **2**, (2016).
22. A.P.Alivisatos. Semiconductor Clusters, Nanocrystals, and Quantum Dots. *Science (80-.).* **271**, (1996).
23. Baker, S. N. & Baker, G. A. Luminescent carbon nanodots: Emergent nanolights. *Angewandte Chemie - International Edition* **49**, 6726–6744 (2010).
24. Lu, C. H., Cecconello, A. & Willner, I. Recent Advances in the Synthesis and Functions of Reconfigurable Interlocked DNA Nanostructures. *Journal of the American Chemical Society* **138**, 5172–5185 (2016).
25. Rothemund, P. W. K. Folding DNA to create nanoscale shapes and patterns. *Nature* **440**, 297–302 (2006).
26. Macfarlane, R. J. *et al. Nanoparticle superlattice engineering with DNA*. *Science* **334**, (2011).
27. Cecconello, A., Besteiro, L. V., Govorov, A. O. & Willner, I. Chiroplasmonic DNA-based nanostructures. *Nature Reviews Materials* **2**, (2017).
28. Zhang, D. Y. & Winfree, E. Control of DNA strand displacement kinetics using toehold exchange. *J. Am. Chem. Soc.* **131**, 17303–17314 (2009).
29. Hermann, T. & Patel, D. J. *Adaptive recognition by nucleic acid aptamers*. *Science*

287, (2000).

30. Hu, Y., Cecconello, A., Idili, A., Ricci, F. & Willner, I. Triplex DNA Nanostructures: From Basic Properties to Applications. *Angew. Chemie - Int. Ed.* **56**, 15210–15233 (2017).
31. Wang, A. H.-J. & Robinson, H. I-Motif. *Encycl. Mol. Biol.* **363**, 561–565 (2002).
32. Siddiqui-Jain, A., Grand, C. L., Bearss, D. J. & Hurley, L. H. *Direct evidence for a G-quadruplex in a promoter region and its targeting with a small molecule to repress c-MYC transcription*. *Proceedings of the National Academy of Sciences of the United States of America* **99**, (2002).
33. Zhuravel, R. *et al.* Advances in Synthesis and Measurement of Charge Transport in DNA-Based Derivatives. *Advanced Materials* **30**, (2018).
34. Guo, X., Gorodetsky, A. A., Hone, J., Barton, J. K. & Nuckolls, C. Conductivity of a single DNA duplex bridging a carbon nanotube gap. *Nat. Nanotechnol.* **3**, 163–167 (2008).
35. Wang, H. *et al.* Transducing methyltransferase activity into electrical signals in a carbon nanotube-DNA device. *Chem. Sci.* **3**, 62–65 (2012).
36. Zheng, M. *et al.* DNA-assisted dispersion and separation of carbon nanotubes. *Nat. Mater.* **2**, 338–342 (2003).
37. Huang, X., Mclean, R. S. & Zheng, M. High-resolution length sorting and purification of DNA-wrapped carbon nanotubes by size-exclusion chromatography. *Anal. Chem.* **77**, 6225–6228 (2005).
38. Lee, K. M., Li, L. & Dai, L. Asymmetric end-functionalization of multi-walled carbon nanotubes. *J. Am. Chem. Soc.* **127**, 4122–4123 (2005).
39. Moghaddam, M. J. *et al.* Highly Efficient Binding of DNA on the Sidewalls and Tips of Carbon Nanotubes Using Photochemistry. *Nano Lett.* **4**, 89–93 (2004).
40. Moghaddam, M. J. *et al.* Erratum: Azide photochemistry for facile modification of graphitic surfaces: Preparation of DNA-coated carbon nanotubes for biosensing (Nanotechnology (2012) 23 (425503)). *Nanotechnology* **24**, (2013).

41. Wan, Y., Liu, G., Zhu, X. & Su, Y. PH induced reversible assembly of DNA wrapped carbon nanotubes. *Chem. Cent. J.* **7**, (2013).

42. Leroy, J. louis, Guéron, M., Mergny, J. louis & Hélène, C. *Intramolecular folding of a fragment of the cytosine-rich strand of telomeric DNA into an I-motif*. *Nucleic Acids Research* **22**, (1994).

43. Ding, B. & Seeman, N. C. Operation of a DNA robot arm inserted into a 2D DNA crystalline substrate. *Science (80-.).* **314**, 1583–1585 (2006).

44. Jariwala, D., Sangwan, V. K., Lauhon, L. J., Marks, T. J. & Hersam, M. C. Carbon nanomaterials for electronics, optoelectronics, photovoltaics, and sensing. *Chem. Soc. Rev.* **42**, (2013).

45. Lipomi, D. J. *et al.* Skin-like pressure and strain sensors based on transparent elastic films of carbon nanotubes. *Nat. Nanotechnol.* **6**, 788–792 (2011).

Chapter 5

A Facile Length Sorting Approach for DNA-wrapped CNTs via Gel Electrophoresis and the Application in CNT Junction Assembly Analysis

5.1 Introduction

Single walled carbon nanotubes (SWCNTs) are one of the most promising building blocks for future nanomaterials, and the length of them (or, our ability to control/select the length of SWCNTs) essentially determines their actual potential for possible applications. The length is the dominant physical dimension of a SWCNT. Certain physical processes, such as carrier recombination, are length-dependent;[1,2] device applications, such as CNT-based scanning probes,[3–5] require CNT length control for easy and reproducible fabrication; solution-phase CNT assemblies of CNTs on solid substrates (e.g. end-to-end CNT junction assembly) will also benefit from CNTs with well-defined length (the uniform building block).[6] Consequently, the capability to obtain a CNT batch with desired length (and with narrower length distribution) is pursued by researchers around the world.

However, given the tremendous progress that has been made in CNT synthesis, directly making CNTs with a particular size remains a major challenge: the current as-produced samples still contain CNTs of varied lengths.[7] As a result, scientists have been trying to seek efficient post-synthetic methods to sort CNTs by their lengths to address the length sorting problem.

Many studies have been done on length sorting.[7,8] Doorn et al. have first demonstrated the possibility to separate as-produced CNTs by length via capillary electrophoresis (CE).[7] The underlying mechanism of such separations is that the mobility of solution phase (the dispersed CNTs in corresponding solutions) is charge and size dependent under the applied electric filed. Moreover, an approach of size-exclusion chromatography (SEC) has shown the potential for CNT length sorting:[9–11] notably, Zheng et al. developed a SEC method with high resolution sorting capability.[12]

However, in many of the reported works, quantification of length variation in obtained fractions was absent. Some works did demonstrate control over the average length of separated tubes; the length variation within a given fraction, however, was typically very broad and could be as high as 80%. In addition, some of the processes reported cannot be scaled up for processing large quantities of materials. It is, thus, highly desirable to develop a scalable process that can yield CNT fractions of well-defined length.

In this context, a facile length sorting approach for DNA-CNTs via agarose gel electrophoresis is demonstrated in this chapter. Length sorted CNT fractions could be acquired within 2 hours, and the quantity of sorted CNTs should be scaled up by simply

increasing the loading well size in the agarose gel block. Moreover, absorption spectra of the sorted fractions suggested the potential of chirality separation for DNA-CNTs by gel electrophoresis. Additionally, the length sorted DNA-CNTs were further applied in a SWCNT molecular junction assembly study, where a single-step chemical strategy with diazonium salts was exploited.[6] These CNTs of well-defined length helped to simplify the AFM analysis of junction assemblies.

5.2 Length sorting of CNTs

The whole sorting procedure (from pristine DNA-CNTs to the stock of length sorted CNT batches) can be divided into three main stages: the preparation, the running, and the extraction/purification.

(a) Preparation.

For the length sorting experiment demonstrated here, HiPco SWCNTs were wrapped by $(GT)_{20}$ single strand DNA under 1 h sonication[13] and the as prepared DNA-CNT aqueous stock solution was ready for further use.

First, a 2% (w/v) agarose (Invitrogen™, Thermo Fisher Scientific) gel block was prepared with an extended loading well. The 1X TAE buffer (40 mM Tris, 20 mM acetic acid, 1mM EDTA, pH 8.6, diluted from 50X TAE by Thermo Scientific) was used for the agarose preparation and to fill the tank (***Figure 5-1 a***).

Then, the DNA-CNT stock solution was thoroughly mixed with supplement glycerol solution (50% v/v aqueous solution) at a 5:2 volume ratio. Afterwards, the mixed solution was loaded into the agarose well (***Figure 5-1 a***).

(b) Running of gel (sorting of DNA-CNTs).

The gel electrophoresis was then carried out at an approximate 1 V/cm electric field strength for 2 h under ice bath. Since the DNA-CNTs were negatively charged in aqueous solution, the DNA-CNTs moved towards the anode (the positively charged electrode). During the electrophoresis a wide gray band of DNA-CNTs was formed in the agarose gel block, indicating the separation of the DNA-CNTs due to the varied moving rates of DNA-CNT species with different sizes (***Figure 5-1 b***).

(c) Extraction and purification.

After the sorting is done, the gray band was divided into 3 fractions (*F1*, *F2*, *F3*) according to their different distances to the loading site (as this distance is the indication of the CNT length distribution in the gel) and put into different dialysis tubings (Snake Skin®, a Dialysis Tubing with 10,000 MWCO, Thermo Scientific) each with 6 mL of 1X TAE buffer inside. The tubings were then sealed at both ends, put back into electrophoresis buffer and subjected to electrophoresis under the same conditions as mentioned before for 1 h until the nanotubes were extracted from the agarose fractions (***Figure 5-1 c***).

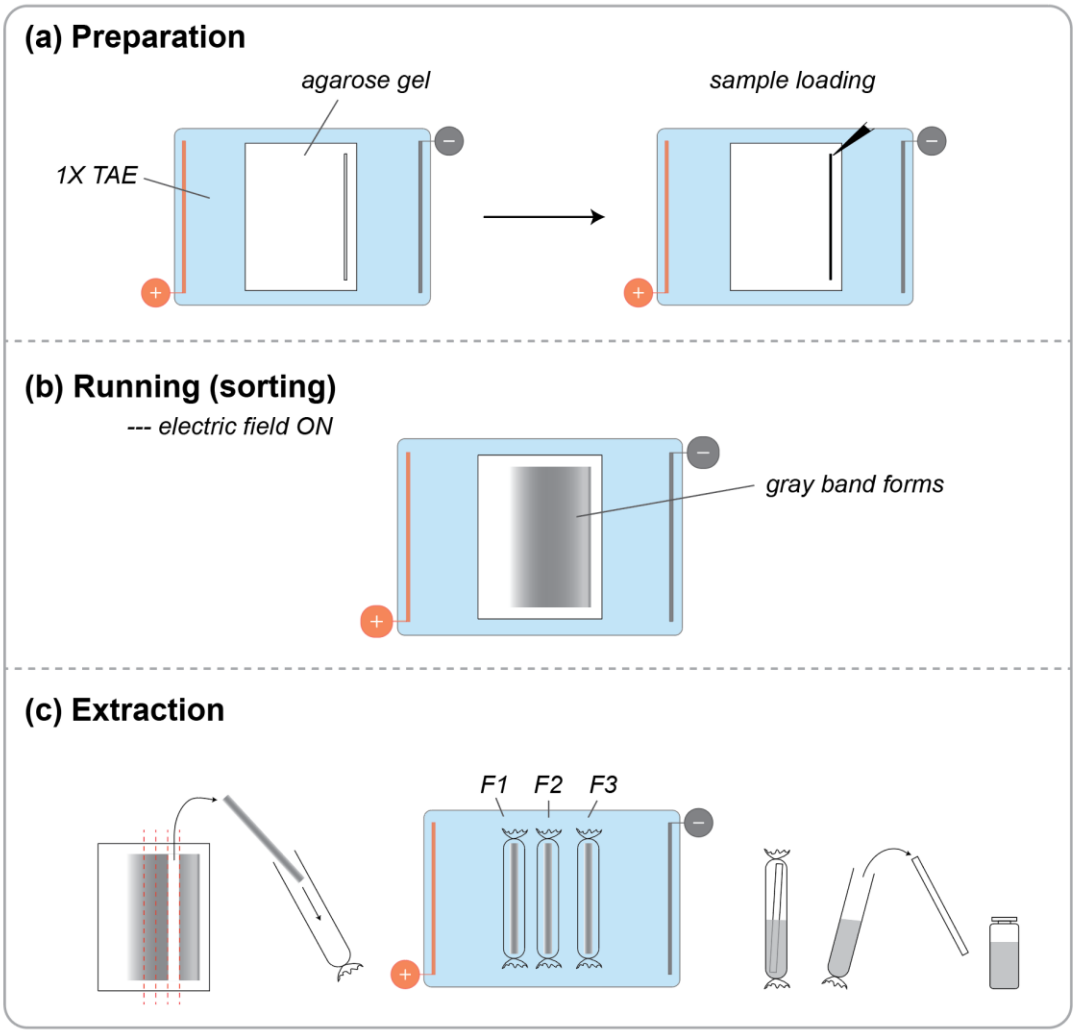

Figure 5-1. *Schematic illustration of the DNA-CNT length sorting procedure via agarose gel electrophoresis. (a) the preparation of gel and the sample loading before the running; (b) during the running (sorting of the DNA-CNTs) stage, a gray band forms in the gel matrix under the influence of applied electric field, indicating the separation of DNA-CNTs; (c) the extraction of the DNA-CNTs from the divided fractions of the gel matrix.*

Finally, the extracted DNA-CNT fractions were subject to overnight dialysis against DI water. The dialyzed solution was then kept as stock solution of length sorted CNTs after a syringe filtration step. Additionally, the stock solutions could also be freeze-dried to

obtain the length-sorted DNA-CNTs in powder. These as-prepared fraction powders could then be dissolved to any desired concentrations for further use.

5.3 Length analysis

The gel sorted DNA-CNTs were imaged with a Bruker Dimension Icon atomic force microscope (AFM) in tapping mode with a 512*512 data point resolution and a scan rate of 1.2 Hz. The solutions of pristine DNA-CNTs and sorted fractions (i.e. *F1*, *F2* and *F3*) were deposited onto freshly cleaved mica discs, which were pre-treated with 1 M $MgSO_4$ solution to enhance the DNA-CNT adsorption, rinsed with water and blow dried before AFM measurement.

A representative AFM image of pristine DNA-CNTs is shown in ***Figure 5-2***. The statistical analysis of pristine DNA-CNTs lengths from all the acquired images suggested the average length to be 213 ± 142 nm (mean value ± standard deviation) (***Figure 5-2***).

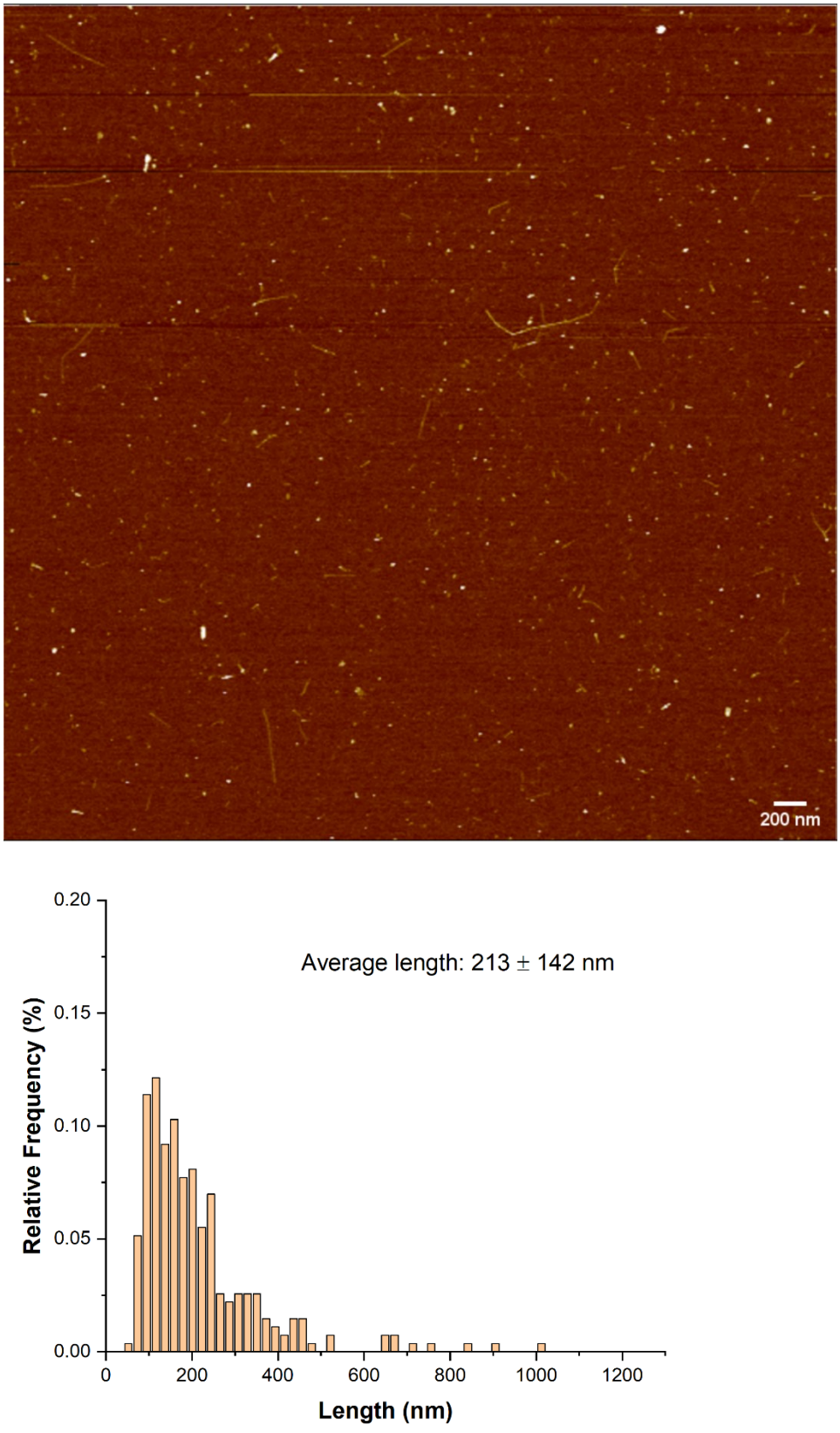

Figure 5-2. *A representative AFM image (top) and the length distribution (bottom) of the pristine DNA-CNTs (272 DNA-CNTs counted).*

As for the sorted fractions, a clear difference in length could be observed from the AFM images directly, suggesting an ascending trend of average length from *F1* to *F3* (***Figure 5-3***, ***Figure 5-4, Figure 5-5***). The corresponding statistical analysis confirmed this observation, where *F1*, *F2* and *F3* showed an average length of 66 ± 23 nm, 241 ± 70 nm and 548 ± 199 nm, respectively. This successful sorting of DNA-CNTs by their lengths can be explained by the simple expression of the moving rate v of the molecule/particle in a gel electrophoresis environment (see Chapter 2, section 2.3.1):

$$v = \frac{Eq}{f}$$

where E is the electric field strength, f is the frictional coefficient and q is the net charge of the molecule. Importantly, the frictional coefficient f has a positive correlation to the particle size r: $f \propto r$.[14] As a result, the bigger the molecule size (here the length of DNA-CNTs), the slower it moves in the gel matrix, and vice versa.

Note that the length distribution of the sorted fractions was narrowed down compared with that of the pristine DNA-CNTs. Specifically, taking the relative standard deviation (standard deviation/mean) as the index, the distribution width has decreased from 66.7% to 34.8% of *F1*, 29.0% of *F2* and 36.3% of *F3*. These narrower distributions again confirm the effectiveness of the sorting strategy.

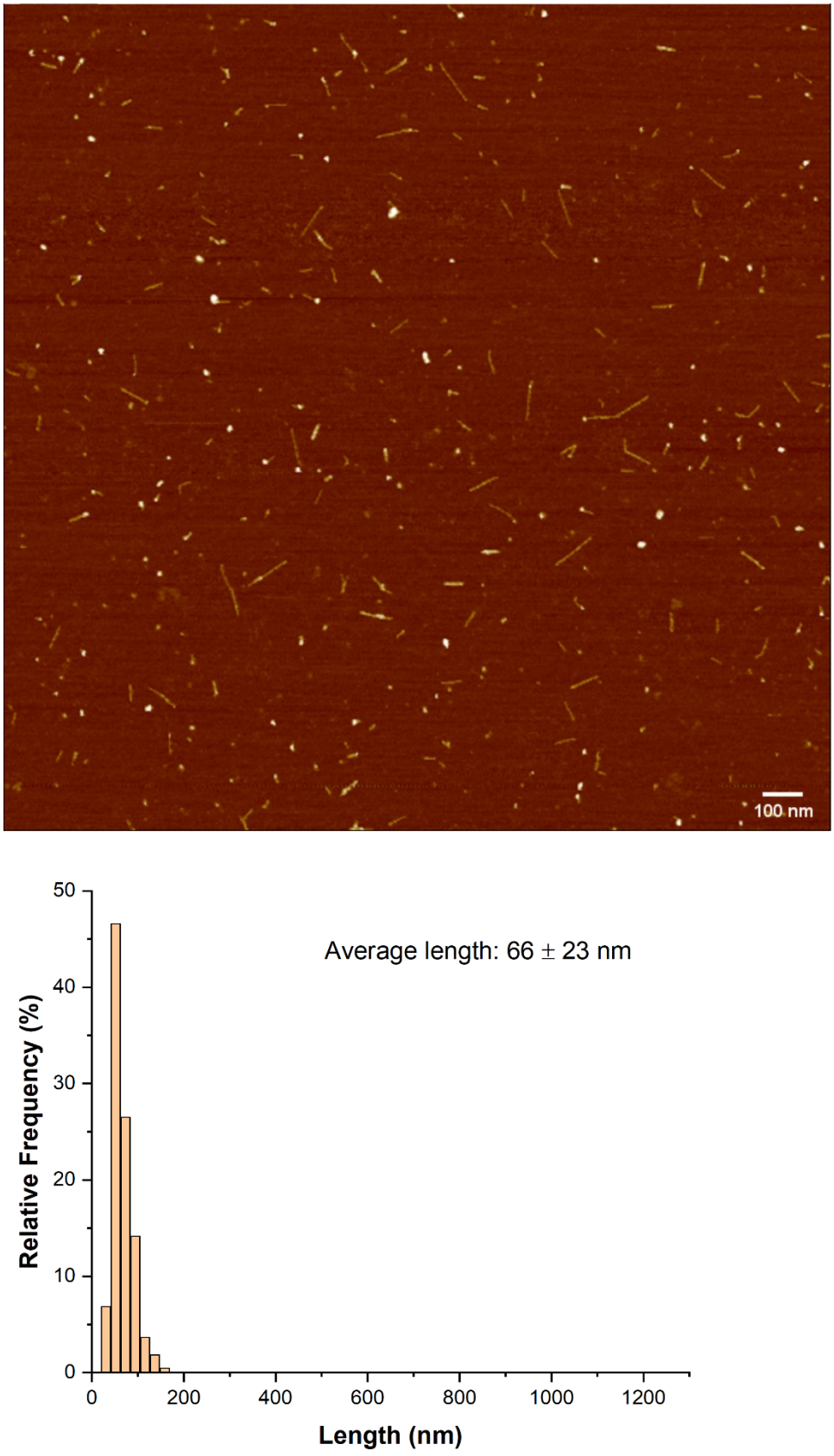

Figure 5-3. *A representative AFM image (top) and the length distribution (bottom) of the sorted fraction 1 (F1; 219 DNA-CNT counted).*

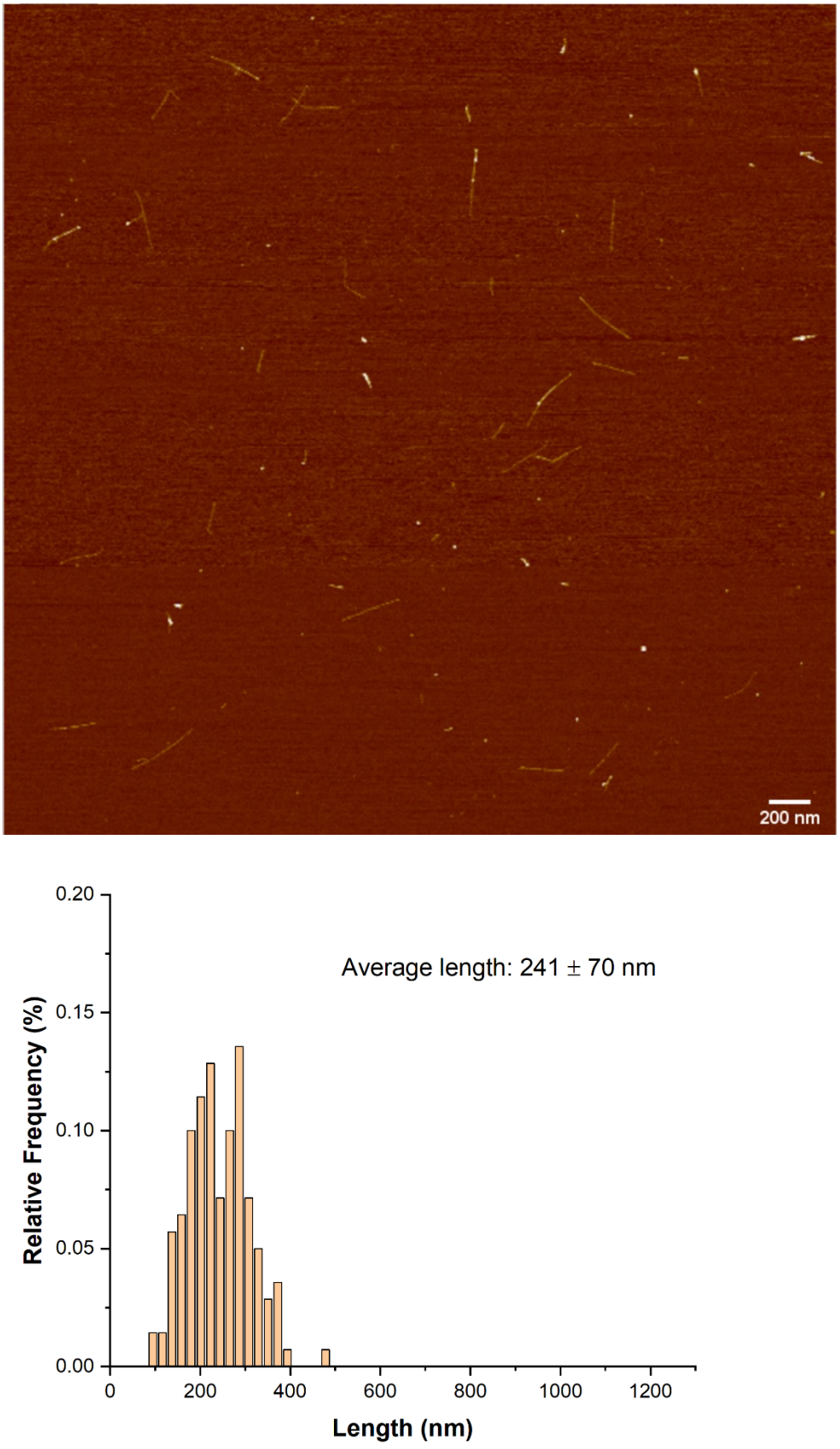

Figure 5-4. *A representative AFM image (top) and the length distribution (bottom) of the sorted fraction 2 (F2; 140 DNA-CNT counted).*

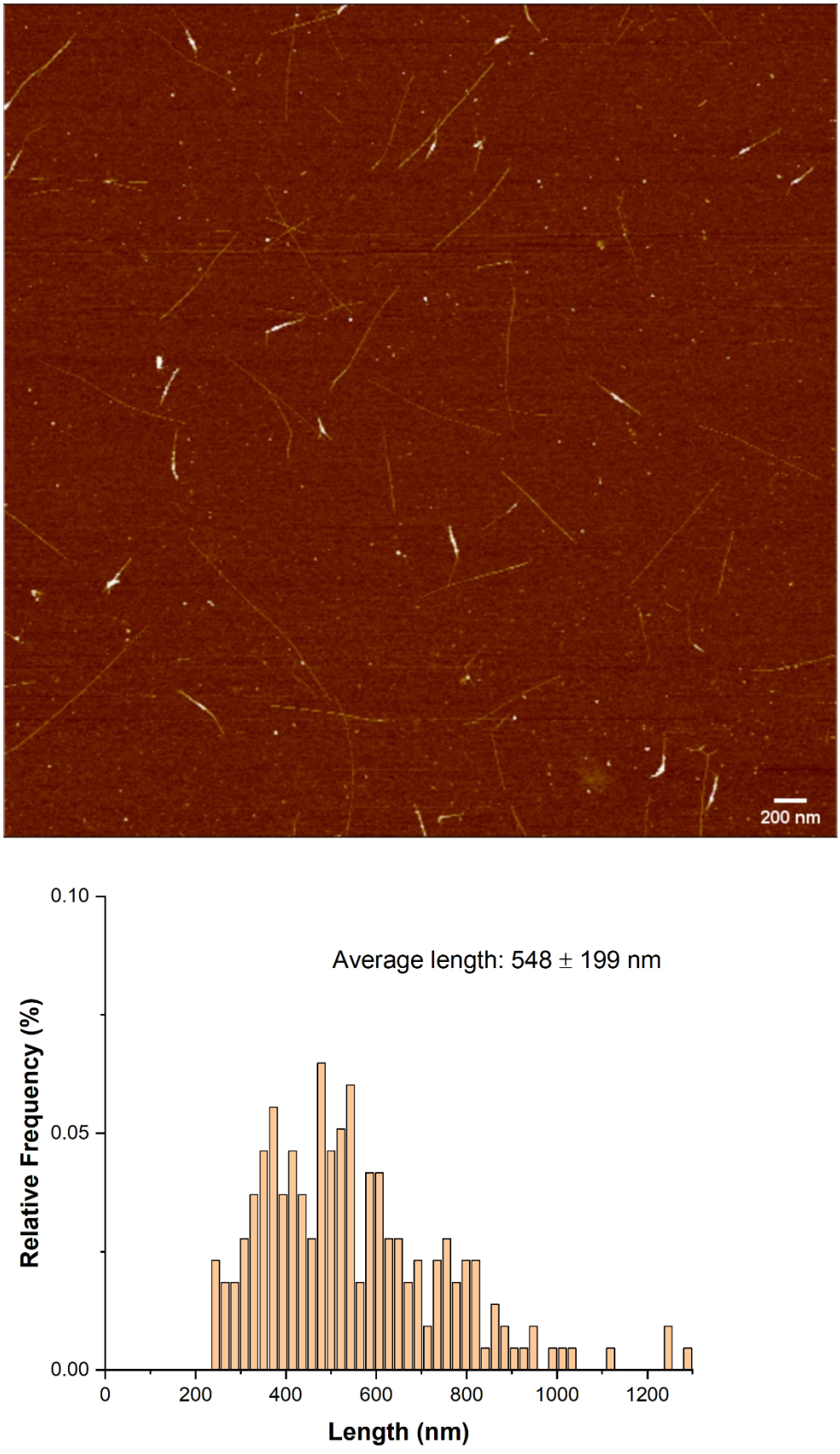

Figure 5-5. *A representative AFM image (top) and the length distribution (bottom) of the sorted fraction 3 (F3; 216 DNA-CNT counted).*

5.4 Potential of chirality separation

In addition to the length analysis with AFM, we investigated the absorption properties of the sorted fractions (*F1, F2, F3*). Intriguingly, some features indicating the separation of SWCNT chirality were observed during the comparison of the absorption spectra (***Figure 5-6***). Though SWCNTs of mixed chiralities from pristine DNA-CNTs [$(GT)_{20}$-HiPco] were still present in all fractions, differences in the relative concentration of certain species were observed. Specifically, as the spectra are normalized at 1130 nm [corresponding to (9,4) and (8,4) species], the relative height of peaks at 1150 nm and 1270 nm [corresponding to (7,6), (8,7), (10,5), (9,5) species as indicated in then spectra] tend to increase from *F1* to *F3*, suggesting the gradual separation of relevant CNT chiralities during the gel sorting.

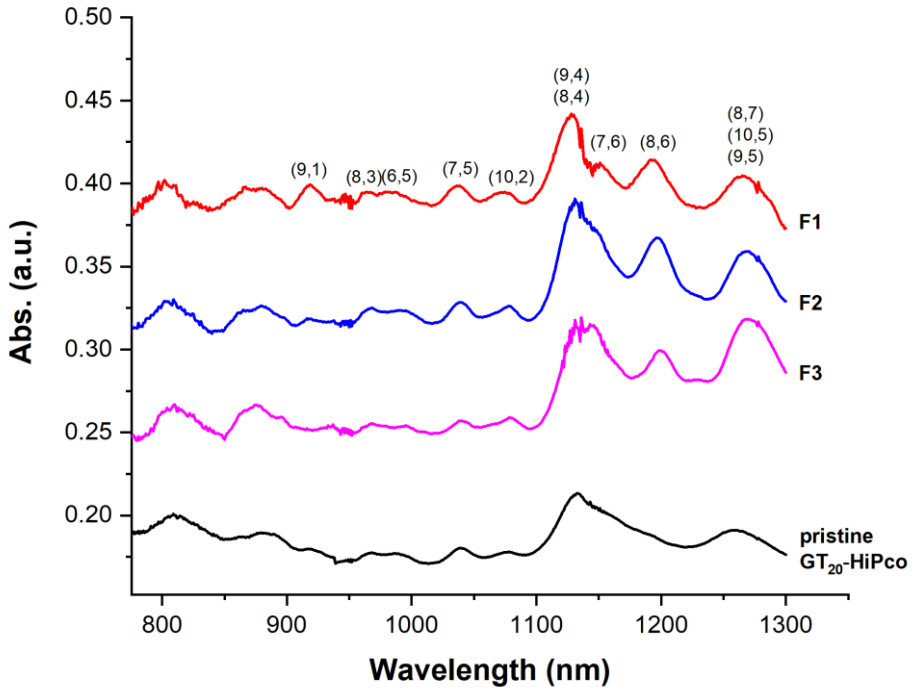

Figure 5-6. *Absorption spectra of the sorted fractions (F1, F2, F3) and pristine DNA-CNTs (GT_{20}-HiPco). The CNT chiral species are labelled on top of the corresponding peaks. The spectra are normalized and vertically offset for better comparison.*

This chirality enrichment/depletion may suggest a correlation between the CNT chirality/diameter and length within the pristine $(GT)_{20}$-HiPco batch, or else some electrophoretic mobility related parameters could be the dominant drive(s) behind this separation. Heller et al. observed an inverse correlation between length and diameter of the gel sorted sodium cholate (SC) dispersed CNTs.[15] On the other hand, Vetcher et al. proposed a higher electrophoretic mobility of semiconducting DNA-CNT compared to metallic ones.[16] Moreover, Tanaka et al. reported the separation of metallic and semiconducting sodium dodecyl sulfate (SDS) dispersed CNTs within gel matrix and attributed this phenomenon to the different affinities between SDS, metallic/semiconducting CNTs and the gel matrix.[17,18] Based on these reports, the dispersing agent (e.g. SC, SDS, DNA) seems to play a major role as different surfactant eventually lead to different outcomes. However, it is still difficult to elucidate the chirality separation phenomenon observed for our gel sorted DNA-CNTs. For instance, the enrichment of (7,6) tubes compared to (9,4) and (8,4) ones from *F1* to *F3*, given they are all semiconducting species, suggesting a high chirality sensitivity of the sorting that has not been clarified so far. Consequently, due to the varied results and explanations, the key mechanism of this chirality separation by gel electrophoresis remains unclear. In general, this observation from the gel sorting of DNA-CNTs reveals the potential of gel electrophoresis for CNT chirality separation purposes.

5.5 Application: optimization of junction assembly analysis

5.5.1 Background

The ability to control the formation of junctions between SWCNTs and functional molecules or nanostructures is of paramount importance for the development of SWCNT-based electronics.[19,20] To address this challenge, the Palma group has reported a single-step chemical strategy for the formation of SWCNT molecular junctions in aqueous solution with water-soluble diazonium salts (see ***Figure 5-7*** for the diazonium salt used for the junction assembly).[6]

In particular, the length sorted DNA-CNTs from the above introduced gel electrophoresis strategy were applied into the SWCNT molecular junction assembly, easing the analysis and interpretation of junction assembly with corresponding AFM data.

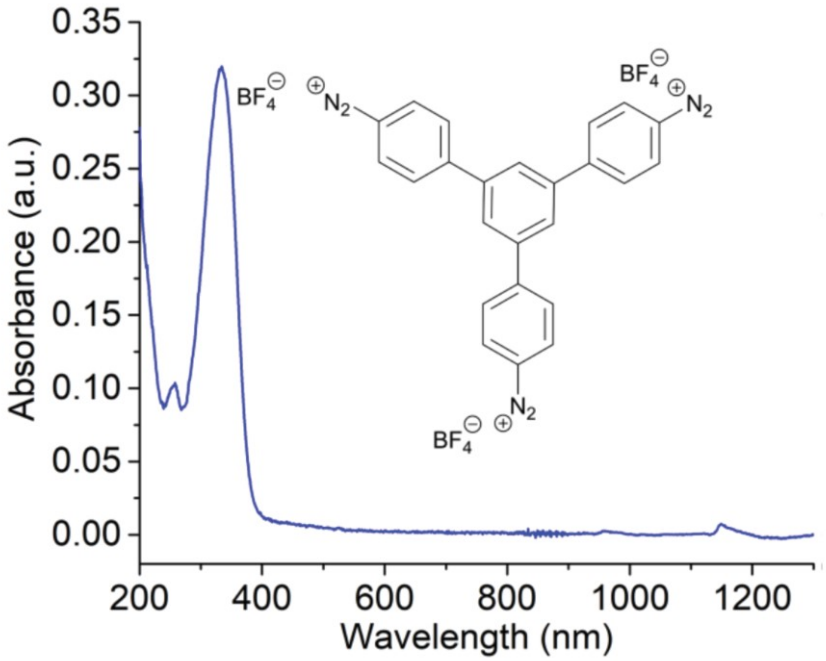

Figure 5-7. *(a) The molecular linker employed in the CNT junction assembly work: 1,3,5-Tris(4-diazophenyl)benzene and its corresponding UV-vis-NIR absorption in water.*[6]

5.5.2 Junction formation analysis

In order to confirm junction formation after the assembly process, the samples were cast on muscovite mica substrates and imaged with atomic force microscope (AFM) (***Figure 5-8***). After being length sorted by gel electrophoresis, the starting SWCNTs before reaction had an average length of 264 ± 92 nm: ***Figure 5-8 a*** displays a representative AFM image and the corresponding SWCNT length histogram. ***Figure 5-8 b*** shows AFM images of linear SWCNT junctions typically obtained employing 1,3,5-Tris(4-diazophenyl)benzene as the linker at a low concentration (18nM): the

average length of the SWCNTs segments was found to increase to 395 ± 155 nm, strongly indicating the junction formation.

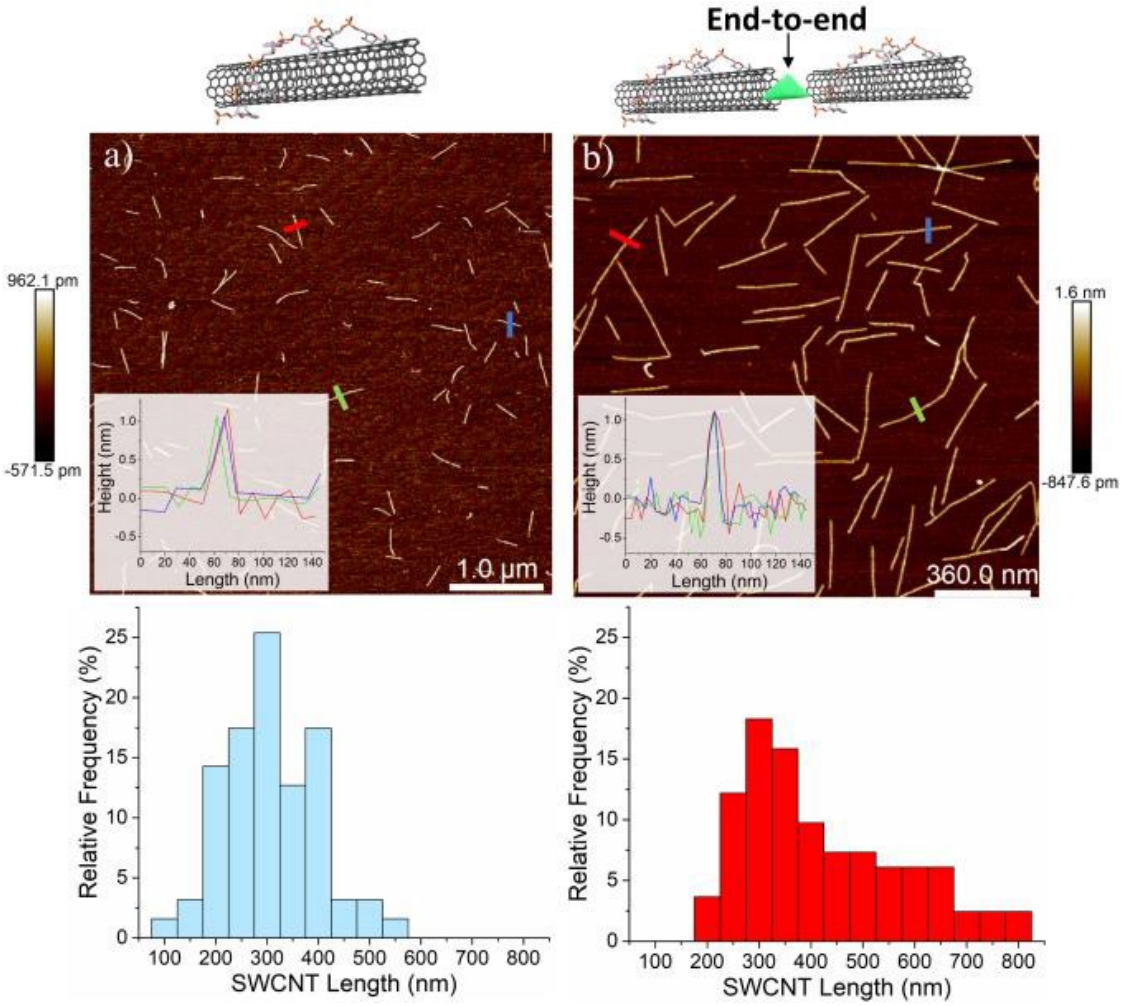

Figure 5-8. *AFM topographical images of: (a) pristine DNA-wrapped SWCNTs; the average length of the SWCNTs was found to be 264 ± 92 nm; (b) linear end-to-end SWCNT junctions formed with the molecular linker at 18 nM; the average length of the SWCNTs was found to be 395 ± 155 nm as determined from ca. 100 nanotubes.*[6]

The junction formation yield was estimated based on the processed AFM data mentioned above. If the total numbers and average lengths of DNA-CNT segments

before and after the junction assembly are N_0 and L_0, N' and L', respectively, and Y percent of the original N_0 DNA-CNTs form the junctions. Given that the original DNA-CNTs were length sorted with a narrow distribution, to simplify the estimation from the AFM data, it is reasonable to assume that all the formed junctions are composed of 2 original DNA-CNT segments. Hence, from the equations

$$N' \cdot L' = N_0 \cdot L_0$$

$$N' = N_0 \cdot \left(1 - \frac{Y}{100}\right) + \frac{1}{2} N_0 \cdot \frac{Y}{100} = N_0 \cdot \left(1 - \frac{Y}{200}\right)$$

we have

$$Y = 200 \cdot \left(1 - \frac{L_0}{L'}\right)$$

as the expression of the yield Y. Eventually, by substituting L_0 and L' with 264 nm and 395 nm, we estimated the final yield of junction formation to be 66.3%.

5.6 Conclusion

In conclusion, a facile length sorting approach for DNA-CNTs via agarose gel electrophoresis has been demonstrated here. After a 2-hour separation process in 2% agarose gel, length-sorted DNA-CNT fractions with the relative standard deviation of length distribution as low as 29% were obtained, which was confirmed by AFM data analysis. Notably, CNT chirality enrichment/depletion among the sorted fractions were observed, suggesting the extra potential in chirality separation by the proposed method. Moreover, the length-sorted DNA-CNTs were further applied in a SWCNT molecular junction assembly study, where a single-step chemical strategy with diazonium salts

was exploited.[6] Based on these CNTs with well-defined length, the junction assembly became obvious via AFM and quantitative analysis of the junction formation yield was achieved and simplified.

This method demonstrated in this chapter offers a facile and low-cost strategy for the length sorting of CNTs. In addition, the amount of processed CNTs could be simply scaled up by extending the loading well size within the agarose gel.

5.7 Materials and methods

DNA dispersion of carbon nanotubes

In brief, HiPco SWCNTs (Sigma Aldrich) were wrapped by single-strand (ss) DNA [$(GT)_{20}$] ((Integrated DNA Technologies, Inc) in 0.1M NaCl (Fisher Scientific) solution under 60 min sonication (VWR basin sonicator, Model USC300TH) to form the DNA-CNTs. The undispersed CNTs and residues (amorphous carbon etc.) were removed by keeping only the supernatant after 90 min centrifugation at 16000 g (Biofuge pico D-37520, Heraeus Instruments).

Length sorting of DNA wrapped SWCNTs by gel electrophoresis

Prepared DNA wrapped SWCNT dispersion was thoroughly mixed with supplement glycerol solution (50% v/v aqueous solution) at a 5:2 volume ratio for further loading into agarose. The gel electrophoresis was then carried out in a 2% (w/v) agarose (Invitrogen^{TM}, Thermo Fisher Scientific) with loaded sample solution using 1X TAE buffer (40 mM Tris, 20 mM acetic acid, 1mM EDTA, pH 8.6, diluted from 50X TAE by Thermo Scientific) at an approximate 1 V/cm electric field strength for 3 h under ice

bath. After the electrophoresis a wide gray band of DNA wrapped CNT was formed in the agarose. The band was divided into 3 fractions according to their different distances to the loading site (as this distance is the indication of the CNT length distribution in the gel) and put into different dialysis tubings (SnakeSkin® Dialysis Tubing with 10,000 MWCO, Thermo Scientific) each with 6 mL of 1X TAE buffer inside. The tubings were then sealed at both ends, put back into electrophoresis buffer and subjected to electrophoresis under the same conditions as mentioned before for 2 h until the nanotubes were extracted from the agarose fractions. Afterwards, the extracted DNA wrapped CNT fractions were to overnight dialysis against DI water and freeze dried for 24 h to obtain the DNA wrapped CNT fractions in powder. The as-prepared fraction powders were then dissolved by 100 mM of NaCl and ready for further junction formation processes.

AFM characterization

Topography analysis of the SWCNT molecular junctions were imaged with a Bruker Dimension Icon atomic force microscope (AFM) with ScanAsyst Air tips (tip radius 12 nm) in tapping mode with 512 samples per line and a scan rate of 1.2 Hz. The sample solution of CNT hybrids was deposited onto a piece of freshly cleaved mica disc, which was pre-treated with 1 M MgSO4 solution to enhance DNA adsorption, rinsed with water and dried before AFM measurement.

The height/length analysis were carried out with the use of Nanoscope Analysis (Bruker, V 1.5), ImageJ (V 1.52p) and OriginPro 2015 (V b9.2.257).

5.8 References

1. Cognet, L. *et al.* Stepwise quenching of exciton fluorescence in carbon nanotubes by single-molecule reactions. *Science (80-.).* **316**, 1465–1468 (2007).
2. Danné, N. *et al.* Ultrashort Carbon Nanotubes That Fluoresce Brightly in the Near-Infrared. *ACS Nano* **12**, 6059–6065 (2018).
3. Stevens, R. M. New carbon nanotube AFM probe technology. *Mater. Today* **12**, 42–45 (2009).
4. Nguyen, C. V., Ye, Q. & Meyyappan, M. Carbon nanotube tips for scanning probe microscopy: Fabrication and high aspect ratio nanometrology. *Meas. Sci. Technol.* **16**, 2138–2146 (2005).
5. Akita, S., Nishijima, H., Nakayama, Y., Tokumasu, F. & Takeyasu, K. Carbon nanotube tips for a scanning probe microscope: Their fabrication and properties. *J. Phys. D. Appl. Phys.* **32**, 1044–1048 (1999).
6. Clément, P. *et al.* A One-Step Chemical Strategy for the Formation of Carbon Nanotube Junctions in Aqueous Solution: Reaction of DNA-Wrapped Carbon Nanotubes with Diazonium Salts. *Chempluschem* **84**, 1235–1238 (2019).
7. Doorn, S. K. *et al.* High resolution capillary electrophoresis of carbon nanotubes. *J. Am. Chem. Soc.* **124**, 3169–3174 (2002).
8. Doorn, S. K. *et al.* Capillary electrophoresis separations of bundled and individual carbon nanotubes. *J. Phys. Chem. B* **107**, 6063–6069 (2003).
9. Heller, D. A. *et al.* Concomitant length and diameter separation of single-walled carbon nanotubes. *J. Am. Chem. Soc.* **126**, 14567–14573 (2004).
10. Niyogi, S. *et al.* Chromatographic purification of soluble single-walled carbon nanotubes (s-SWNTs) [1]. *Journal of the American Chemical Society* **123**, 733–734 (2001).
11. Farkas, E., Elizabeth Anderson, M., Chen, Z. & Rinzler, A. G. Length sorting cut single wall carbon nanotubes by high performance liquid chromatography. *Chem.*

Phys. Lett. **363**, 111–116 (2002).

12. Huang, X., Mclean, R. S. & Zheng, M. High-resolution length sorting and purification of DNA-wrapped carbon nanotubes by size-exclusion chromatography. *Anal. Chem.* **77**, 6225–6228 (2005).

13. Zheng, M. *et al.* DNA-assisted dispersion and separation of carbon nanotubes. *Nat. Mater.* **2**, 338–342 (2003).

14. Adamson, N. J. & Reynolds, E. C. Rules relating electrophoretic mobility, charge and molecular size of peptides and proteins. *J. Chromatogr. B Biomed. Appl.* **699**, 133–147 (1997).

15. Heller, D. A. *et al.* Concomitant Length and Diameter Separation of Single-Walled Carbon Nanotubes. *J. Am. Chem. Soc.* **126**, 14567–14573 (2004).

16. Vetcher, A. A. *et al.* Fractionation of SWNT/nucleic acid complexes by agarose gel electrophoresis. *Nanotechnology* **17**, 4263–4269 (2006).

17. Saito, T., Ohmori, S. & Shukla, B. High-Yield Separation of Metallic and Semiconducting Single-Wall Carbon Nanotubes by Agarose Gel Electrophoresis Continuous Separation of Metallic and Semiconducting Carbon Nanotubes Using Agarose Gel Takeshi Tanaka, Yasuko Urabe, Daisuke Nishide et al. -. *Appl. Phys. Express* **1**, (2008).

18. Tanaka, T. *et al.* Simple and scalable gel-based separation of metallic and semiconducting carbon nanotubes. *Nano Lett.* **9**, 1497–1500 (2009).

19. Zhen, Y., Postma, H. W. C., Balents, L. & Dekker, C. Carbon nanotube intramolecular junctions. *Nature* **402**, 273–276 (1999).

20. Fuhrer, M. S. *et al.* Crossed nanotube junctions. *Science (80-.).* **288**, 494–497 (2000).

Chapter 6

Conclusions and Future Challenges

On the current and upcoming stage of nanomaterials, carbon nanotubes (CNTs) play a significant role because of their nanoscale diameter and exceptional thermal, mechanical, electrical and electronic properties. Among the various research directions concerning CNTs, one central effort is to synergistically combine CNTs with other nanoscale components by the construction of CNT-based nano-assemblies or nanohybrids.

In this thesis, we first discussed the use of DNA-wrapped single walled carbon nanotubes (DNA-CNTs) templates for the assembly of hybrid nanostructures with inorganic semiconducting materials and their use in optoelectronic devices (Chapter 3). In particular, based on the Coulomb interaction between the metal cations and negatively charged DNA phosphate backbone in H_2O, a facile one-pot two-step procedure was introduced where the PbS-DNA-CNT or CdS-DNA-CNT hybrids were assembled by simple sequential additions of metal cations (Pb^{2+} or Cd^{2+}) and S^{2-} in aqueous solution. The direct assembly of PbS/CdS QDs along the DNA-CNT templates the was confirmed by atomic force microscopy (AFM). Afterwards, both DNA-CNTs

and the assembled hybrids were used to fabricate photo-sensing devices that, given their nanoscale dimensions, achieve photoresponses of more than 100% current change within 1 s. Importantly, by immobilizing different hybrids (i.e. DNA-CNTs, PbS-DNA-CNTs and CdS-DNA-CNTs) on the same chip via dielectrophoresis (DEP), devices exhibiting multiplexed sensing capabilities were realized. Notably, very different photoresponses have been observed for devices based on DNA-CNT/CdS-DNA-CNT and PbS-DNA-CNT hybrids. These were explained by different mechanisms of device operation (i.e. photo-induced molecular desorption model for DNA-CNT/CdS-DNA-CNT devices and electron transfer model for PbS-DNA-CNT devices), which were confirmed by us from further electrical (photoresponse measurement in vacuum and gate dependence test) and excited state lifetime (TAS measurement) investigations.

Notably, the role of DNA-CNTs in this study is twofold: i) the suggested photo-induced molecular desorption process for DNA-CNT device highlights the potential of DNA-CNTs for the construction of light-gas correlated sensing devices; ii) DNA-CNTs can be the effective templates for the assembly of varied CNT-inorganic nanohybrid materials in aqueous solutions. This versatile templated assembly method for the construction of inorganic-organic nanohybrids not only realized the direct growth of semiconducting QDs along the sidewall of well-dispersed DNA-CNTs in aqueous solutions without extra chemical functionalization (thus a non-destructive route that preserves the electronic properties of SWCNTs and enhances the charge transfer within the heterostructures), but also facilitated the fabrication of multiplexed photo-sensing nanodevices. In general, devices based on these novel hybrids will pave the way towards next-generation photodetection with outstanding performance and merits including nanoscale dimensions and outstanding flexibility.

We then presented a straightforward approach for the fabrication of end-to-end SWCNT junctions exploiting oligonucleotides as molecular linkers (Chapter 4). Specifically, terminal ends of DNA-CNTs were functionalized with azido-modified single-strand DNAs (ssDNAs) via an efficient UV activated cycloaddition reaction. The two end-functionalized ssDNA strands of pre-designed sequences were partly complementary so that they could hybridize to form a partial duplex under neutral pH conditions and thus formed the desired SWCNT junctions. Significantly, the self-assembled junctions were capable to react to specific stimuli (pH and DNA sequence) and exhibited reconfiguration potentials by repeated assembly/disassembly under varied environmental conditions. This was contributed to the inherent features of the designed DNA sequences: the formed junctions disassembled when the solution pH changed from 7 to 5, via the formation of an energetically favored i-motif structure at acidic pH, hence destabilizing the DNA partial duplex bridging the nanotubes; as the individual SWCNTs were then subjected to neutral pH, the DNA duplex reformed as it became the more stable configuration under such conditions. Similarly, assembly/disassembly were also enabled by the addition of specific ssDNA strands via the strand-displacement mechanism. Consequently, the successful assembly of end-to-end SWCNT junctions with stimuli-controlled reconfiguration potentials were confirmed by morphological analysis (AFM) and time-dependent fluorescence characterizations.

The strategies developed in this work allowed us to construct reconfigurable end-to-end SWCNT junctions, which has the potential to provide a step further towards the

low-cost fabrication of nanoelectronic devices, including the use of SWCNTs as nanoelectrodes in molecular transport junctions and single molecule investigations. In addition, the stimuli correlated reconfiguration capabilities demonstrated here is of great importance for the future implementation of stimuli-responsive molecular systems and nanoscale smart devices. Generally speaking, this work has explored the possibility of synergistically combining SWCNT and DNA nanotechnology to produce programmed stimuli-responsive SWCNT junctions.

To address the CNT length sorting problem, a length sorting strategy for DNA-CNTs via agarose gel electrophoresis is demonstrated (Chapter 5). This facile method of 3 major stages (i.e. the preparation, the running/sorting, the extraction and purification) allowed us to acquire length-sorted DNA-CNT fractions within 2 hours. Every length-sorted DNA-CNT fraction had its own distinct average length from the others with a narrow length distribution (relative standard deviation of length distribution as low as 29%), which was confirmed by AFM data analysis. In addition, the quantity of processed CNTs could be scaled up by simply increasing the loading well size in the agarose gel block. Moreover, the gel-sorted DNA-CNTs were further applied in a SWCNT molecular junction assembly study, where a single-step chemical strategy with diazonium salts was exploited. These CNTs with well-defined length were proved to simplify the AFM analysis and the yield estimation of junction assembly.

The method demonstrated in Chapter 5 offers a practical and low-cost facile strategy for the length sorting of CNTs. Notably, this is a scalable strategy as the amount of processed CNTs could be simply increased by extending the loading well size within the agarose gel.

In summary, by integrating DNA-CNTs with other active components, we have achieved the assembly for organic-inorganic nanohybrids of multiplexed photo-sensing capabilities and the reconfigurable SWCNT junctions with stimuli-responsive features. The strategies developed in these works contributed to the assemblies of novel CNT based functional nanohybrids with the potential to be implemented in next generation nanoelectronic devices and single molecular systems. Moreover, a facile and efficient method to sort DNA-CNTs by their lengths was demonstrated to address the length sorting challenge of CNTs.

CNTs do present substantial opportunities to nanoscience and nanotechnology as well as significant challenges for future work in relevant fields. Gaining further control in the assembly of CNT based heterostructures will continue to open new possibilities in basic science and real-world applications. The strategies to assemble nanocomponents (e.g. quantum dots, metal nanoparticles) with CNTs into well-organized structures offer the promising direction to approach nanoscale problems and construct novel molecular-scale systems and devices with advanced electronic, electrical, photophysical features. Nevertheless, there are always some ultimate goals in front of us: to realize the self-assembly and manipulation of defect-free CNT based hybrids at the industrial level by simple and effective methods, gain absolute control over CNT length and chirality, and be able to directly introduce modifications to any desired sites along the CNT.